Multi-scale mechanics of traumatic brain injury

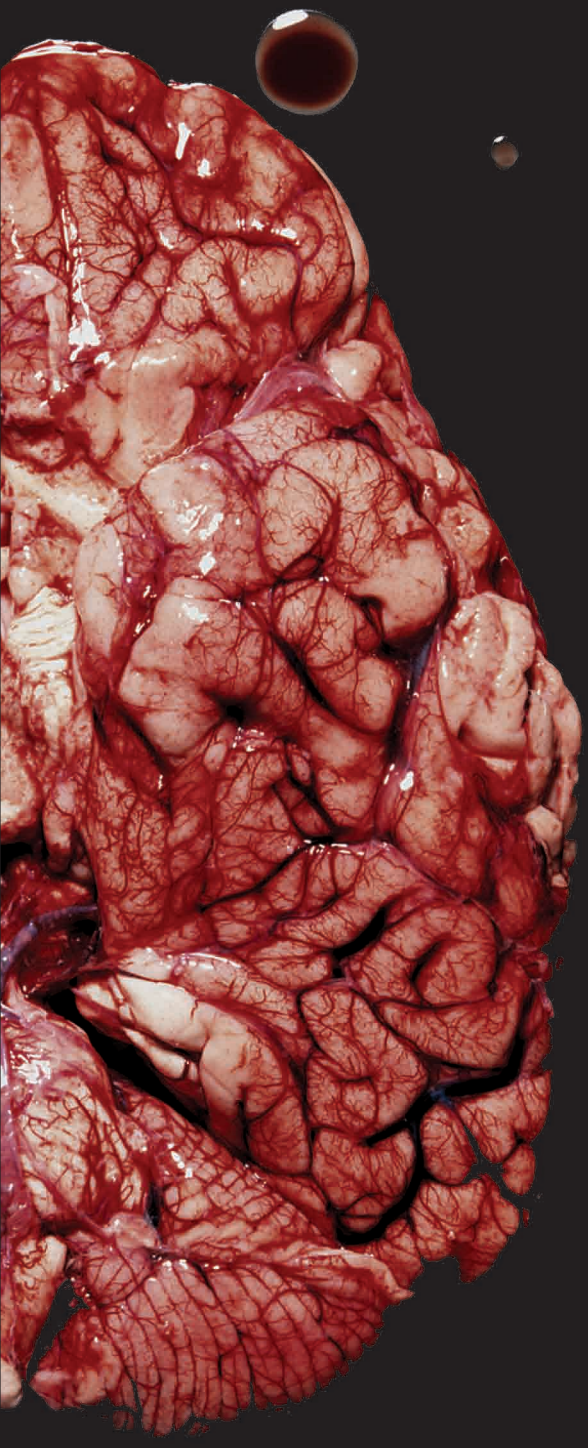

Multi-scale mechanics of traumatic brain injury

Rudy Cloots

Multi-scale mechanics of traumatic brain injury

Rudy Cloots

This work has been supported by the Dutch Technology Foundation STW, applied science division of NWO and the Technology Program of the Ministry of Economic Affairs.

A catalogue record is available from the Eindhoven University of Technology Library.

ISBN: 978-90-386-2909-4

Cloots, Rudolf J. H.

Multi-scale mechanics of traumatic brain injury

Eindhoven University of Technology, 2011.
Proefschrift.

Photograph on cover: Overdose - Congestive brain
© Fragile 2009 - courtesy Raphaël Dallaporta (used with permission)
Out of the series Fragile that has won the Foam Paul Huf Award 2011

This thesis is prepared with LaTeX 2_ε

Printed by Ipskamp Drukkers B.V., Enschede, The Netherlands.

Multi-scale mechanics of traumatic brain injury

Proefschrift

ter verkrijging van de graad van doctor
aan de Technische Universiteit Eindhoven,
op gezag van de rector magnificus, prof.dr.ir. C.J. van Duijn,
voor een commissie aangewezen door het College voor Promoties
in het openbaar te verdedigen op
maandag 21 november 2011 om 16.00 uur

door

Rudolf Johannes Hubertinus Cloots

geboren te Sittard

Dit proefschrift is goedgekeurd door de promotor:

prof.dr.ir. M.G.D. Geers

Copromotor:
dr.ir. J.A.W. van Dommelen

Contents

Summary

Multi-scale mechanics of traumatic brain injury

Traumatic brain injury (TBI) can be caused by road traffic, sports-related or other types of accidents and often leads to permanent health issues or even death. For a good prevention or diagnosis of TBI, brain injury criteria are used to assess the probability of brain injury as a result of a mechanical insult. TBI is concerned with a wide range of length scales from several decimeters at the head level, where the mechanical insult is applied, to several micrometers at the cellular level, where the actual injury occurs in case of diffuse axonal injury (DAI). However, a well-defined relation between these levels has not been established yet. The most used method to assess the likelihood of brain injury is based on head level kinematics, but suffers from a number of drawbacks and does not consider the mechanisms by which brain injury develops. Finite element models are being developed to predict brain injury based on tissue level injury criteria.

Because most finite element head models used nowadays for injury prediction do not contain anatomical details at the tissue level, the first part of this research is concerned with the influence of the heterogeneous substructure of the brain on the mechanical loading of the tissue. For this, four finite element models with different geometries were developed, where three models have a detailed geometry representative for a small part of the cerebral cortex including the sulci and gyri. The fourth model has a homogeneous geometry and it is used together with the heterogeneous models to analyze the influence of the morphological heterogeneities in the cerebral cortex. The results of the simulations show concentrations of the equivalent

stress that correspond to pathological observations of injury in literature. This implies that tissue-based injury criteria may not be directly applied to most computational head models used nowadays, which do not account for sulci and gyri.

The next step in this research is involved with the relation between the tissue and the cellular-level mechanics since the microstructural organization will affect the transfer of mechanical loads from the tissue level to the cellular constituents and will thereby affect the sensitivity of brain tissue to mechanical loads. According to literature, discrete axonal impairments caused by a mechanical insult on the brain are located where axons have to deviate from their normal course due to the presence of an inclusion, such as a blood vessel or a cell body. Based on the hypothesis that the observed discrete injuries are caused by the micromechanical heterogeneities, finite element models representing a critical volume for discrete local impairment of the axons have been developed. From the results of these simulations, concentrations of axonal strains are located at similar locations as the axonal impairments. Furthermore, it is concluded that the sensitivity of brain tissue to a mechanical load is orientation-dependent. In a multi-scale approach, finite element models of the head and the axonal level are coupled, where it is observed that the maximum axonal strains do not correlate with the strain levels of the head model in a straightforward manner. An anisotropic criterion for brain injury based on tissue-level strains is proposed that describes the orientation dependent sensitivity of brain tissue to mechanical loads and is derived from the observed axonal strain in the micromechanical simulations. With the anisotropic brain injury criterion, computational head models will be able to account for aspects of DAI at the cellular level and will therefore more reliably predict injury.

Notation

In the following definitions, a Cartesian coordinate system with unit vector base $\{\vec{e}_1, \vec{e}_2, \vec{e}_3\}$ applies and following the Einstein summation convention, repeated indices are summed from 1 to 3.

Quantities

scalar	a
vector	$\vec{a} = a_i \vec{e}_i$
second order tensor	$\boldsymbol{A} = A_{ij} \vec{e}_i \vec{e}_j$
local quantities	a, $\boldsymbol{A}$
global quantities	$\bar{a}$, $\bar{\boldsymbol{A}}$
relative quantities	$\hat{a} = \frac{a}{\bar{a}}$
normalized quantities	$\check{a} = \frac{\bar{a}}{\bar{a}_{\text{reference}}}$

Operations

transpose	$\boldsymbol{A}^T = A_{ji} \vec{e}_i \vec{e}_j$
inverse	$\boldsymbol{A}^{-1}$
determinant	$\det(\boldsymbol{A}) = (\boldsymbol{A} \cdot \vec{e}_1) \cdot (\boldsymbol{A} \cdot \vec{e}_2) \times (\boldsymbol{A} \cdot \vec{e}_3)$
trace	$\operatorname{tr}(\boldsymbol{A}) = \boldsymbol{A} : \vec{e}_i \vec{e}_i = A_{ii}$

isochoric part	$\tilde{\boldsymbol{A}} = \det(\boldsymbol{A})^{-\frac{1}{3}}\boldsymbol{A}$
deviatoric part	$\boldsymbol{A}^d = \boldsymbol{A} - \frac{1}{3}\mathrm{tr}(\boldsymbol{A})\boldsymbol{I}$
first invariant	$I_1 = \mathrm{tr}(\boldsymbol{A})$
second invariant	$I_2 = \frac{1}{2}\left[\mathrm{tr}(\boldsymbol{A})^2 - \mathrm{tr}(\boldsymbol{A}^2)\right]$
third invariant	$I_3 = \det(\boldsymbol{A})$
fourth invariant	$I_4 = \boldsymbol{A} : \vec{n}\vec{n}$
Macaulay operator	$\langle a \rangle = \frac{1}{2}(\lvert a \rvert + a)$
time derivative	$\dot{\boldsymbol{A}}$
multiplication	$c = ab$
	$\vec{c} = a\vec{b}$
	$\boldsymbol{C} = a\boldsymbol{B}$
dyadic product	$\boldsymbol{C} = \vec{a}\vec{b} = a_i b_j \vec{e}_i \vec{e}_j$
cross product	$\vec{c} = \vec{a} \times \vec{b}$
inner product	$c = \vec{a} \cdot \vec{b} = a_i b_i$
	$\boldsymbol{C} = \boldsymbol{A} \cdot \boldsymbol{B} = A_{ij} B_{jk} \vec{e}_i \vec{e}_k$
double inner product	$c = \boldsymbol{A} : \boldsymbol{B} = A_{ij} B_{ji}$

Chapter one

Introduction

1.1 General introduction

Traumatic brain injury (TBI) caused by a mechanical insult on the head causes high rates of mortality and disability [1,2]. The social costs of traffic accidents are evaluated at some 160 billion euro per year in the European Union alone [3]. Other major causes of head injuries are sports and falls [4]. In collision sports such as soccer, ice hockey, rugby and American football, a high frequency of concussions is documented [5–10]. In the Netherlands for example, 54% of professional soccer players and 50% of amateur players experience a concussion at some point in their career [7,8]. Although the severity of the head injuries resulting from collisions in sports or falls are generally lower than those resulting from traffic accidents, their effects can also be long-lasting or even cause disabilities [11,12]. This is especially true for axonal injury, which is a common pathology resulting from brain trauma [13–15].

During accidents, the mechanical impact on the head is translated into stresses and strains of brain tissue. It is generally agreed that tissue damage associated with injury to the central nervous system (CNS) is a consequence of an extended neuro-chemical cascade on the cellular level, set in motion by deformation of brain tissue inside the head [16–20]. Thus, the mechanism of TBI involves biomechanics at various length scales; from the macro level

at which the external loads occur to the micro level at which brain cells are injured (see Figure 1.1).

In this chapter, background information on TBI will be given at the individual length scales followed by the objective of this study and the outline of this thesis.

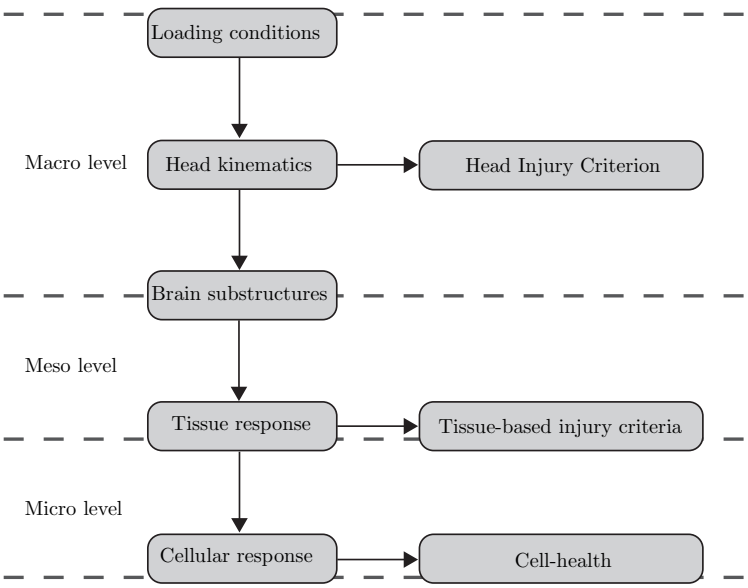

Figure 1.1: Schematic representation of different length scales that are involved in the mechanism of TBI development due to a mechanical load on the head and the criteria for injury at these different levels.

1.2 Traumatic brain injury: from macro to micro

In this section, the aspects of TBI at the macro, the meso and the micro level will be elaborated (see Figure 1.1). Each of the following subsections presents the anatomy and the injury biomechanics of these length scales.

1.2.1 Macro level

This section covers the aspects of TBI on the length scale that is typical for the whole head including its most important substructures.

Anatomy – macro level

The central nervous system (CNS) consists of the brain and the spinal cord [21,22]. Protection against mechanical loads is provided by the cranium (i.e., the part of the skull holding the brain) and by the vertebrae. The brain consists of the cerebrum, the diencephalon (which is sometimes considered to be a part of the cerebrum), the cerebellum and the brain stem (Figure 1.2). The latter is connected to the spinal cord. The cerebrum accounts for about 83% of the total brain mass and it consists of the two cerebral hemispheres [21].

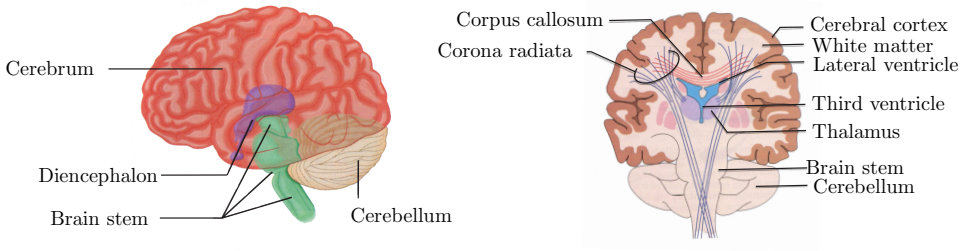

Figure 1.2: Anatomy of the human brain (adapted from [21]). (a) Left lateral view. (b) Coronal cross-section.

The meninges are the membranes that cover the CNS and thereby provide additional protection [21,22]. Three types of meninges exist: dura mater, arachnoid, and pia mater (Figure 1.3). The dura mater is the strongest meninx and it is attached to the inside of the cranium [21,22]. At several places in the cranium, the dura mater extends inwards forming dural septa, which provide mechanical stability. The dural septa include the falx cerebri (separating the cerebral hemispheres), the falx cerebelli (separating the

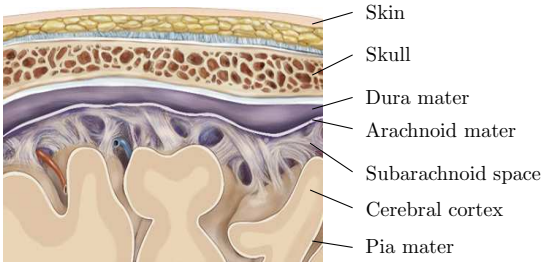

Figure 1.3: Schematic representation of a cross section of a part of the skull and meninges [23,24].

cerebellar hemispheres), and the tentorium cerebelli (separating cerebrum and cerebellum). The arachnoid is a thin meningeal layer between the other two meninges [21,22]. It is attached to the dura mater bridging the folding structure of the outer surface of the cerebrum. This causes the existence of the subarachnoid space, which contains cerebrospinal fluid (CSF) and blood vessels. The arachnoid is connected to the pia mater by arachnoid trabeculae, which help suspend the brain within the meninges. This might have a mechanical influence. These trabeculae are more existent outside the sulci and almost not existent inside the sulci. The pia mater also is a thin meningeal layer and it is attached to the surface of the CNS, which means that it follows the irregularities of the surface of the CNS [21,22]. It contains small blood vessels that penetrate the cerebrum.

The brain and spinal cord are surrounded by CSF [21,22,25]. It is thought to have a mechanical protective function for the brain. In case of a mechanical load applied to the head, it allows the brain to move independently to the cranium to some extent. Furthermore, it provides a physiologically stable internal environment, which is necessary for normal brain functioning [26]. Its total volume is approximately 150 ml, of which 25 ml is situated within four communicating ventricles inside the brain. The remaining part is located inside the subarachnoid space. It is composed of 99% water and is similar in composition to blood plasma, from which it originates [21,27]. The CSF is secreted mainly inside the ventricles and reabsorbed into the venous system at several sites in the arachnoid [22,25].

Injury biomechanics – macro level

Brain injury types can be categorized, according to their clinical appearance, in focal injury and diffuse injury [28]. Mechanical loading conditions that lead to TBI are subdivided into static (>200 ms) and dynamic (<200 ms) loads [28]. Static loads are associated with focal brain injuries. Dynamic loads can occur either from a contact load of the head inducing strain waves through the cranium and the brain and in some cases even skull fracture or from a non-contact acceleration of the head, in which the mechanical load is transmitted from the body to the head [28]. Dynamic contact loads are associated mainly with focal brain injuries, whereas non-contact loads are associated mainly with focal brain injuries for translational accelerations and diffuse brain injuries of cerebral white matter for rotational accelerations. However, some more recent studies have shown that rotational accelerations lead to high local stresses in the cerebral cortex (gray matter) [29–31]. A translational acceleration of the head leads to compressive hydrostatic stresses in one side of the brain and tensile hydrostatic stresses in the opposite side. However, if the brain deforms inhomogeneously due to virtually incompressibility, deviatoric stresses occur as well. In case of a rotational acceleration of the skull, the rotation of the brain is delayed because of inertia. As a consequence, deviatoric stresses occur within the brain.

The most commonly used brain injury criterion in the automotive industry is the Head Injury Criterion (HIC), which is based on global head kinematics and is defined as [32]:

$$\mathrm{HIC} = \left\{ (t_2 - t_1) \left[\frac{1}{t_2 - t_1} \int_{t_1}^{t_2} a(t) dt \right]^{2.5} \right\}_{max}, \tag{1.1}$$

in which $a(t)$ refers to the translational head acceleration in g as a function of time, and t_1 and t_2 refer to the initial and final time in seconds, respectively. These times are chosen such that the HIC obtains a maximum value, provided the time interval between t_1 and t_2 does not exceed an empirically determined maximum. The HIC is based on experimental data, in which only anterior-posterior contact loading has been applied to human cadavers, not accounting for angular accelerations of the head.

For a better approximation of the relation between TBI and a mechanical load, more advanced methods have been developed in which the internal head response is investigated. These methods include the usage of physical and numerical models of the head and brain. Margulies et al. [33] found that the falx cerebri has a strain reducing effect on the brain tissue using a physical experiment. Ivarsson and co-workers [34,35] investigated the influence of the cerebral ventricles by means of a physical set-up. They found a reduction in the strain in the sagittal and coronal plane due to the ventricles.

Numerical models to predict head injury were initially developed in the 1970s and early 1980s, but newer numerical head models were not developed until the early 1990s [27]. From then on, numerical head models were being refined to include more and more details of the anatomy and mechanical behavior of the head and brain. The latest three-dimensional numerical head models contain viscoelastic material behavior and its geometries contain the main anatomical substructures, such as the ventricles and the falces (e.g., [36–39]). Two of these head models are depicted in Figure 1.4. A three-dimensional head model containing the detailed substructures of the cerebral cortex has been developed by Ho and Kleiven [40]. These head models form a bridge towards the loads at the tissue level.

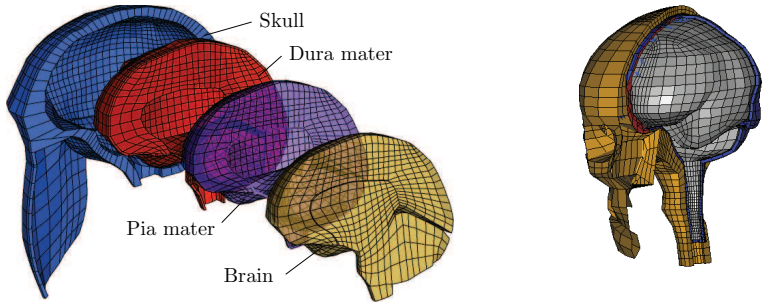

Figure 1.4: Numerical head models developed for predicting TBI developed by (a) Hrapko et al. [39] and (b) Kleiven [37]

The CSF is considered to have a protective function for the brain during mechanical loading, making it an important constituent of the head with respect to TBI. Therefore, it is important to provide a good representation of CSF in a numerical head model. Some of the current models simulate CSF, arachnoid and dura mater as one material [41–43]. Because of this assumption, the CSF is modeled too stiff in terms of its shear modulus. Perhaps, this has been done because a low shear modulus can result in numerical instability [44]. A different approach used in some FE head models to represent the CSF is by means of a sliding interface (e.g., [37,45]).

1.2.2 Meso level

In this section, the anatomical and mechanical details leading to a heterogeneous injury distribution of the tissue are discussed.

Anatomy – meso level

Besides the larger substructures of the head discussed in the previous section, also small anatomical heterogeneities exist in the head that can influence the development of TBI. At the tissue level, the convolutions of the cerebral cortex can be distinguished, where gyri are separated by sulci [21]. Some of the sulci are deeper and they divide the brain into brain lobes. The cortex contains gray matter and is 2 to 5 mm in thickness [21,22,25,27,46]. The gyral regions have an average and standard deviation thickness of 2.7±0.3 mm versus 2.2±0.3 mm for the sulcal regions [46]. Still, it accounts for about 40% of the total brain mass [21].

Inferior to the cerebral cortex lies the cerebral white matter [21]. It contains mainly neurons with myelinated axons, which give the white matter its color. The white matter is also found in other parts of the CNS, e.g., the brain stem, the cerebellum, and the spine. The function of the white matter neurons is the communication between cerebral areas and between the cerebral cortex and the lower CNS areas [21]. Neurons connecting more distant areas are bundled. The largest bundle of neurons connecting the two cerebral hemispheres is the corpus callosum (Figure 1.2b). The axons in the corona radiata connect the cerebral cortex to the spinal cord, as is depicted in Figure 1.2b, as well as the neurons throughout the cortex to one another.

Injury biomechanics – meso level

In a study by Bradshaw et al. [47], a gel-filled chamber that represented the brain and skull in a coronal plane including the falx cerebri and the sulci of the cerebral cortex has been used. They have found an increase of the maximum principle strain in the cerebral cortex due to the sulci.

Many studies have been conducted to characterize the material behavior of brain tissue, but the discrepancy between the results of these studies is large. According Hrapko and co-workers [48], the storage and loss modulus to describe the linear viscoelastic behavior differs orders of magnitude between the various studies in literature. More recent non-linear viscoelastic constitutive models for brain tissue have been developed by Hrapko et al. [49] and Shen et al. [50]. Their independently measured data are relatively similar. Hrapko and co-workers have taken their samples from the corona radiata, whereas the samples from Shen and co-workers are a combination of white matter from the corona radiata and gray matter from the cerebral cortex. These experiments have been performed with porcine brain tissue. Experiments on fresh human brain tissue material have indicated that its mechanical properties are approximately 30% stiffer than those of fresh porcine brain tissue [51].

Differences in mechanical properties and variation of anisotropy of the tissues between the various regions in the brain can constitute mechanical heterogeneities. In their results, Prange et al. [51] found differences between the average material properties of the corpus callosum and the cerebral cortex, but not between the corona radiata and the cerebral cortex. The shear modulus of the brainstem was found to be almost twice as high as the shear modulus of the cerebrum [52]. Several studies conducted by Elkin and co-workers showed heterogeneities of the mechanical properties within the hippocampus and the cortex [53,54] as well as between different regions of the brain [55,56]. Anisotropy has been found for the corona radiata, where the ratios of the shear moduli in different directions was found to be up to 1.5 [51,57]. For the brainstem, these ratios are between 1.1 and 1.2 [52]. The material properties of the brainstem were determined by Ning et al. [58]. The initial shear modulus of the matrix was 12.7 Pa, whereas initial modulus of the fibres was 121.2 Pa.

In research performed by Bain and co-workers [59,60], tissue strains are related to axonal injury. For the white matter of the optic nerve of the guinea pig, morphological injury does not occur below a Lagrange tissue strain 0.14, whereas all axons were injured for a strain above 0.34. The functional impairment of the optic nerve in the same study was tested by exposing the eye to light flashes. No functional impairment of the axons occurred below a tissue strain of 0.13, whereas all axons experienced impairment above a tissue strain of 0.28. In most cases, the functionality returned to pre-injury levels after 72 h.

Morrison III et al. [61] used a method in which organotypic brain slice cultures were stretched on a membrane. By using organotypic brain slices, the three-dimensional cellular structure of brain tissue was accounted for in the experiments. It was found that a biaxial Lagrange strain between 0.2 and 0.5 at a strain rate of 10 s^{-1} applied to rat organotypic hippocampal slice cultures resulted in cell injury at two days after loading, but this was decreased at four days. For strain rates of 20 and 50 s^{-1}, injury was not existent at two days after injury, but it was at four days. A Lagrange strain of 0.35 at a strain rate of 10 s^{-1} caused about twice as much cell damage as a 0.10 Lagrange strain at a strain rate of 20 s^{-1} [62]. In a following study, however, using more statistical data it was concluded that hippocampal cell death is dependent on tissue strain, but not on strain rate [63].

For an improved interpretation of mechanical tissue responses in FE head models, meso-level axonal orientations have been accounted for in recent studies. Chatelin and co-workers [64] investigated the possibility of obtaining tissue strain in the axonal directions using diffusion tensor imaging (DTI). Colgan et al. [65] used the fiber-reinforced Holzapfel-Gasser-Ogden model together with DTI to describe the anisotropic behavior of brain tissue in an FE head model. In a study performed by Wright and Ramesh [66], local variations of axonal orientations at the tissue level obtained from DTI were used for the anisotropic tissue behavior as well as for the axonal strains in a plane strain model with dimensions of 7 by 7 mm. The results of these three studies showed a significant influence of the axonal orientation in terms of the axonal strains as well as the anisotropic mechanical behavior.

1.2.3 Micro level

The micro level is here defined as the typical length scale at which individual cells or their processes can be distinguished.

Anatomy – micro level

Nervous tissue consists of two types of cells: neurons and glial cells [21, 22]. The structure of the neurons consists of a soma (i.e., cell body) and processes that extend from the soma. Typically, a (multipolar) neuron has multiple dendrites which are short processes, whereas it has a single axon that is much longer. In the CNS, including both gray and white matter, the average ratio of glial cells to neurons is 9 to 1. Glial cells make up about half the mass of the brain and of these glial cells, the astrocytes are the most abundant and have numerous radiating projections that cling to neurons and capillaries. Other glial cells are the oligodendrocytes, the microglia and the ependymal cells. Oligodendrocytes have fewer branches than the astrocytes and they wrap their processes around the thicker fibers in the CNS producing myelin sheaths (i.e., insulating coverings). Microglia are small ovoid cells with processes that touch nearby neurons. Ependymal cells are in different shapes and they line the central cavities of the CNS.

Pyramidal cells have a conical soma from which multiple processes emerge [22]. Pyramidal cells range in size from 10 μm in diameter all the way up to the 70 to 100 μm giant pyramidal cells (Betz cells) of the motor cortex, which are among the largest neurons in the CNS. Several studies show somal sizes of (healthy) cortical and hippocampal neurons of about 10 to 20 μm [67–72]. Pyramidal cells have long axons that leave the cortex to reach either other cortical areas or various subcortical sites. Axons are uniform in diameter and can be many centimeters long, whereas dendrites taper away from the cell body and rarely exceed 500 μm in length [73]. The nonpyramidal cells are small (i.e., often less than 10 μm) granular cells, but a variety of other types and sizes have been described. Glial cells have a spherical soma and most of them have a diameter of about 5 to 10 μm [68,70]. In the cerebral cortex, the ratio of glia to neurons is in the range of about 1.0 to 2.0 [70,74–76].

Injury biomechanics – micro level

The response of neurons to a traumatic mechanical load can be divided in three phases [77]:

1. Initial physical damage of cellular structures, especially the plasma membrane, and the immediate consequences of this damage, e.g., membrane depolarization and increase of the intracellular calcium level.

2. Injured neurons either recover to some degree or they die within 24 hours, typically characterized by necrosis, i.e., unregulated cell death.

3. After 24 hours still cell death can occur, but typically via apoptosis, i.e., programmed cell death. The causation of cell death during this period is much less clear than in phase 2.

Mechanical and functional injury of the neurons and glial cells has been investigated in several different studies. The measured quantities indicative of injury were amongst others: change of intracellular Ca^{2+} concentration, uptake by the cells of molecules that are normally impermeable to the cell membrane, blocking of certain channels in the cell membrane, swelling, signal conduction, gene expression and axotomy. In these studies, brain cells are stretched individually or by means of a stretched membrane on which the cells are adhered. Uniaxial and biaxial linear strains up to 0.5 of rat cortical neurons did not lead to cell death within 24 hours after the applied strain according to a study conducted by Geddes-Klein et al. [78]. In that same study, however, it was evidenced that biaxial strains resulted in much more injury than uniaxial strain. Floyd and colleagues [79] concluded that a mechanical load applied to rat cortical astrocytes results in about 20% up to almost 60% cell death within 24 hours caused by a linear strain of 0.3 and 0.5, respectively. Axotomy of cultured human neurons did not occur at a linear strain below 0.65 according to Smith and co-workers [80]. According to a study by Lusardi et al. [81], uniaxial straining of rat hippocampal neurons led to an injury response for linear strains between 0.01 and 0.17 with strain rates ranging from 0.007 to 8 s^{-1}. However, cell death at 24 hours after loading did only occur for strains above 0.5. Experiments conducted by Singh and colleagues [82] showed that the

strength and conduction velocity of the action potential in rat dorsal nerve roots was influenced for linear strains below 0.1 and completely blocked above 0.2, which indicates that physiological damage of neurons is related to mechanical loading in a gradual manner.

According to a pathological study performed by Povlishock et al. [15], DAI is not associated with direct mechanical tearing of axons in the white matter, but with discrete focal impairment of individual axons. The impairments were all found at locations where the axon changed its anatomical course, e.g., near a blood vessel, a nucleus, or another, decussating axon. Furthermore, they have found that damaged axons could be found intermingled with intact axons.

In addition to the research that tries to relate mechanical loading to cellular injury, several studies were performed on the local mechanics at the cellular or axonal level. According to the results of the experiments conducted by Lu et al. [83], pyramidal cells and astrocytes are much softer than most other eukaryotic cells. Furthermore, they found that the storage modulus of pyramidal and glial processes amounted to about one-third of their respective somata. In a study by Heredia et al. [84], the myelinated layer covering white matter axons had no significant influence on the mechanical behavior for a load in the direction perpendicular to the axonal axis using AFM. For both myelinated and demyelinated axons, the Young's modulus was similar, i.e., 0.9 ± 0.7 MPa and 0.8 ± 0.5 MPa, respectively. The mechanical stiffness of the axons was studied by Dennerll and co-workers [85] as well as by Bernal and co-workers [86]. An important observation by Dennerll et al. was that chick dorsal root ganglion neurites had a stiffness 10 times that of PC12 neurites. According to Dennerll and co-workers, this difference in stiffness was possibly contributed to the existence of the neurofilaments in the DRG neurites, which are not a significant feature of the PC12 ultrastructure.

Bain and co-workers [87] developed a micromechanical analytical model that accounted for the undulation of the axons. Arbogast and Margulies [88] made a micromechanical analytical model representing several aligned fibers in the brainstem. The model consists of a fiber volume fraction and a matrix volume fraction, in which the material properties of the fibers were obtained from mechanical experiments with a guinea pig optic nerve that was assumed to consist completely of fibers. After that, the material prop-

erties of the matrix were determined by obtaining the volume fractions of fibers and matrix of the brainstem and fitting the model to the mechanical tissue properties of the brainstem.

It is clear that each length scale has its own characteristics with respect to TBI. Moreover, these characteristics are related to each other, both within and across length scales, which makes TBI a multi-scale phenomenon.

1.3 Objective

A crucial step in understanding the mechanism by which TBI develops and being able to predict TBI, is to translate the global head loads to the local loading conditions, and consequently damage, of the cells and to project cellular level and tissue level injury criteria back towards the level of the head. Although much research has focused on head injury at individual length scales, the relation between these levels has not been established yet. Therefore, the objective of this research is to bridge the various length scales that are involved in the mechanism of TBI development due to impact, such that the macroscopic mechanical loads are translated into mechanical loading of brain tissue and individual cells via the underlying microstructure at various levels. For this, several numerical models at different length scales are used, which will be introduced in the next section.

1.4 Outline of the thesis

In this thesis, a computational multi-scale approach is used to obtain the tissue and the cellular response due to a mechanical load on the head.

In Chapter 2, a meso-level model is developed, which represents a detailed part of the cerebral cortex. This model forms the bridge between the head and the tissue by accounting for the influence of the heterogeneous substructures of the brain, in particular the gyri and sulci of the cerebral cortex. The loading conditions of the meso-level model are obtained from a head model simulation (see Figure 1.5).

A critical volume element (CVE) is developed in Chapter 3 representing

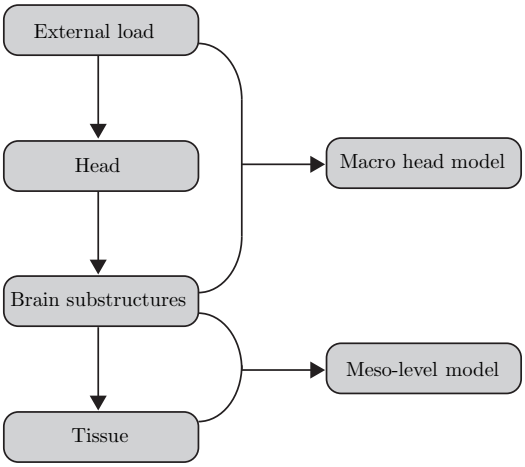

Figure 1.5: Modeling approach of the study in Chapter 2.

a critical region for axonal injury at the cellular level in a single scale plane strain modeling approach (see Figure 1.6). The CVE is based on the observations of a pathological study conducted by Povlishock [15] and it relates axonal strains to tissue strains.

The CVE is extended in Chapter 4 to a three-dimensional model in a single scale approach. Furthermore, an anisotropic equivalent strain measure is developed that is able to predict axonal strains from tissue strains and thereby forms an alternative to a full multi-scale approach using the three-dimensional CVE (see Figure 1.6).

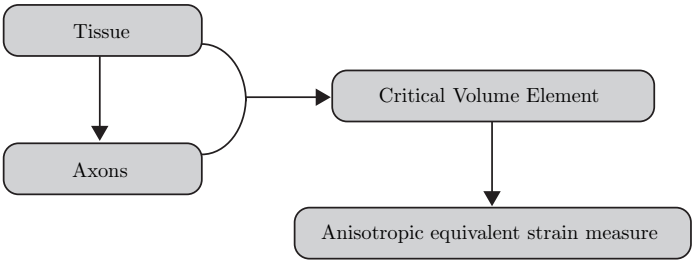

Figure 1.6: Modeling approach of the study in Chapters 3 and 4.

In Chapter 5, the three-dimensional CVE is used in a multi-scale framework where a computational head model is used at the macro level (see Figure 1.7). In addition to this, a single (macro) scale approach is used, in which the anisotropic equivalent strain measure is used to predict axonal strains directly from the tissue strains in the head model.

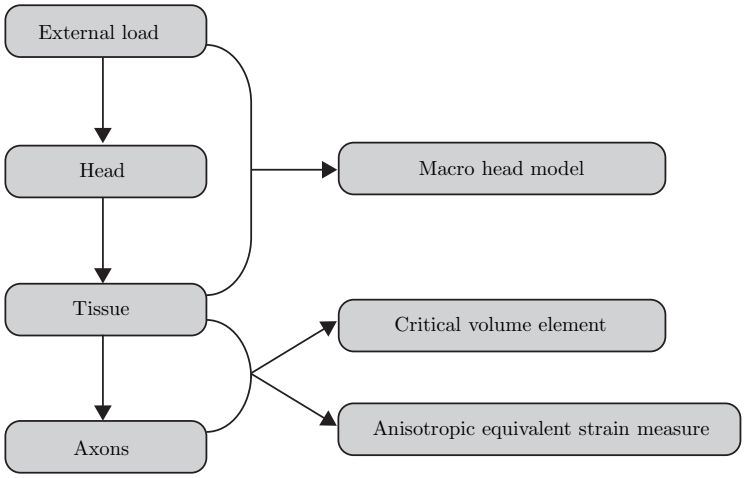

Figure 1.7: Modeling approach of the study in Chapter 5.

In Chapter 6, a general discussion, conclusions and future recommendations concerning the multi-scale modeling of TBI as well as the development and use of the anisotropic equivalent strain measure are given.

The finite element implementation of the non-linear viscoelastic material model used in Chapter 2 is explained in Appendix A.

Chapter two

Injury Biomechanics of the Cerebral Cortex

Traumatic brain injury (TBI) can be caused by accidents and often leads to permanent health issues or even death. Brain injury criteria are used for assessing the probability of TBI, if a certain mechanical load is applied. The currently used injury criteria in the automotive industry are based on global head kinematics. New methods, based on finite element modeling, use brain injury criteria at lower scale levels, e.g., tissue-based injury criteria. However, most current computational head models lack the anatomical details of the cerebrum. To investigate the influence of the morphologic heterogeneities of the cerebral cortex, a numerical model of a representative part of the cerebral cortex with a detailed geometry has been developed. Several different geometries containing gyri and sulci have been developed for this model. Also, a homogeneous geometry has been made to analyze the relative importance of the heterogeneities. The loading conditions are based on a computational head model simulation. The results of this model indicate that the heterogeneities have an influence on the equivalent stress. The maximum equivalent stress in the heterogeneous models is increased by a factor of about 1.3 to 1.9 with respect to the homogeneous model, whereas the mean equivalent stress is increased by at most 10%. This implies that tissue-based injury criteria may not be accurately applied to most computational head models used nowadays, which do not account for sulci and gyri.

Reproduced from: R.J.H. Cloots, H.M.T. Gervaise, J.A.W. van Dommelen and M.G.D. Geers (2008). Biomechanics of Traumatic Brain Injury: Influences of the Morphologic Heterogeneities of the Cerebral Cortex. *Annals of Biomedical Engineering*, **36** (7), 1203-1215.

2.1 Introduction

The brain is often one of the most seriously injured parts of the human body in case of a road traffic crash situation [89–91]. The incidence rate and mortality rate in Europe are estimated to be 235 and 15.4 per 100,000 of the population per year, respectively [89]. Traumatic brain injury (TBI) is therefore considered as a widespread problem. Understanding the mechanisms inducing TBI is necessary for reducing the number of occurrences, e.g., by developing more appropriate protective systems and diagnostic tools.

Brain injury criteria are used for the assessment of the probability of TBI for certain mechanical loading conditions. The most commonly used injury criterion in the automotive industry is the Head Injury Criterion (HIC) [92,93]. It is developed to predict TBI resulting from a translational acceleration of the head. One of the drawbacks of the HIC is that it is based on global kinematic data to predict TBI, whereas actual brain damage is caused at the cellular level as a consequence of tissue strains and stresses [94]. Furthermore, it is based on experimental data, in which only anterior-posterior contact loading has been applied to human cadavers, not accounting for angular accelerations of the head. For a better approximation of the relation between TBI and a mechanical load, more advanced methods have been developed. For instance three-dimensional finite element (FE) head models have been developed to predict brain injury [41–45,95–99]. With these numerical head models, different injury mechanisms and loading conditions can be distinguished. However, in these models, the heterogeneous anatomy of the cerebrum is usually represented by a relatively homogeneous geometry. A comparison between the homogeneous geometry of a typical finite element head model and the complex structure of a real brain is given in Figure 2.1. The main function of the heterogeneous morphology is to increase the cortical surface in order to obtain a more complex level of the brain functions [22]. The most recent numerical head models include ventricles and the invaginations of the dura mater, but none include the convolutions of the cerebral cortex. Consequently, the stresses and strains that are predicted from these models likely do not represent actual tissue stresses and strains, at least in the cortex. Therefore, although tissue-based injury criteria may be used, their accuracy is expected to be limited. This

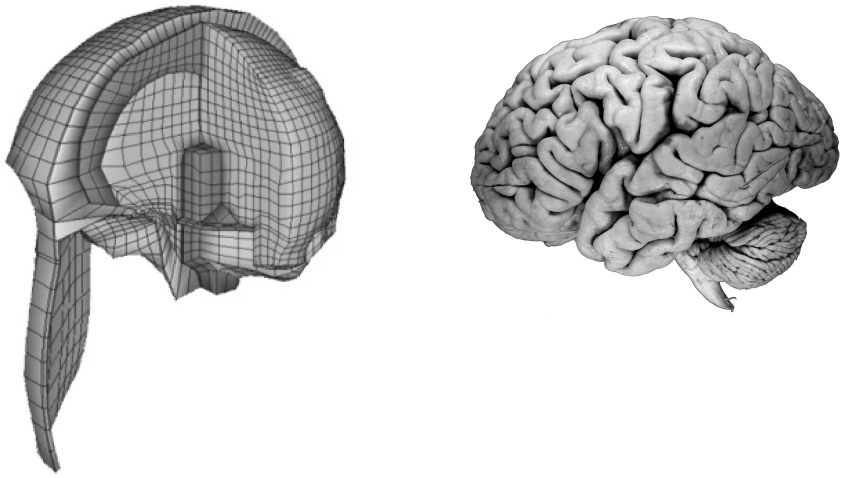

(a) (b)

Figure 2.1: (a) Numerical head model developed by Claessens [41,95]. (b) Lateral view of the human brain. Adapted from Welker et al. [100].

might prohibit the direct use of tissue-based injury criteria. Such criteria predict injury at the tissue level and are based on in vitro and in vivo experiments. [59–62,78,79,101] For a direct application of tissue-based injury criteria in a computational head model, a more detailed description of the biomechanical behavior of the cerebrum may be required, which can be achieved by including its morphologic heterogeneities in these models. A few two-dimensional FE models of the brain containing the convolutions of the cerebral cortex have been described in literature. Miller et al. [102] compared different modeling techniques for the relative motion between the brain and the cranium. Nishimoto and Murakami [103] developed a model to investigate the relation between brain injury and the HIC. However, these models have not been developed with the purpose of investigating the local biomechanics at the level of these convolutions. No conclusions have been drawn from these studies on the biomechanical influence of the heterogeneities of the cerebral cortex, due to the limited spatial resolution of the mesh.

Physical experiments have been conducted in several studies to investigate

the biomechanical consequences of the heterogeneities of the cerebrum [104]. In a study by Bradshaw et al. [47], a gel-filled chamber that represented the brain and skull in a coronal plane including the falx cerebri and the sulci of the cerebral cortex was subjected to a rotation with a peak acceleration of approximately 7800 rad s^{-2}. An increase of the maximum principle strain in the cerebral cortex due to the sulci was found.

The aim of this study is to investigate the biomechanical influences of the morphologic heterogeneities in the cerebral cortex. To achieve this, several two-dimensional FE models with detailed geometries of a part of the cerebral cortex have been developed. Also, a FE model with a homogeneous morphology of the cortex has been made. The loading conditions are based on simulations with a computational head model as used by Brands et al. [41]. The results of the simulations of the heterogeneous models will be compared to those of the homogeneous model.

2.2 Methods

In this study, plane strain models of small sections of the cerebrum are made using the FE code Abaqus 6.6-1 (HKS, Providence, USA). An explicit time integration is used, anticipating a dynamic load with a high magnitude and a short duration. The time increments are limited by the stability condition, which is determined in the global estimator function in Abaqus.

2.2.1 Geometries

To investigate the influence of the heterogeneities of the cerebral cortex, a homogeneous model and three heterogeneous models have been developed. The heterogeneous models, which are shown in Figure 2.2b, d, and e have detailed geometries of a small part of the cerebrum, including also a part of the cerebrospinal fluid (CSF). The cranium is modeled by a boundary constraint, as will be detailed further on. Since the dura mater and the arachnoid are connected to the inside of the cranium in the region that is modeled [21,22], it is assumed that they can be ignored for this situation. The pia mater, which is a thin and delicate membrane covering the brain [21,22], is also not included, since it is expected to have no mechanical

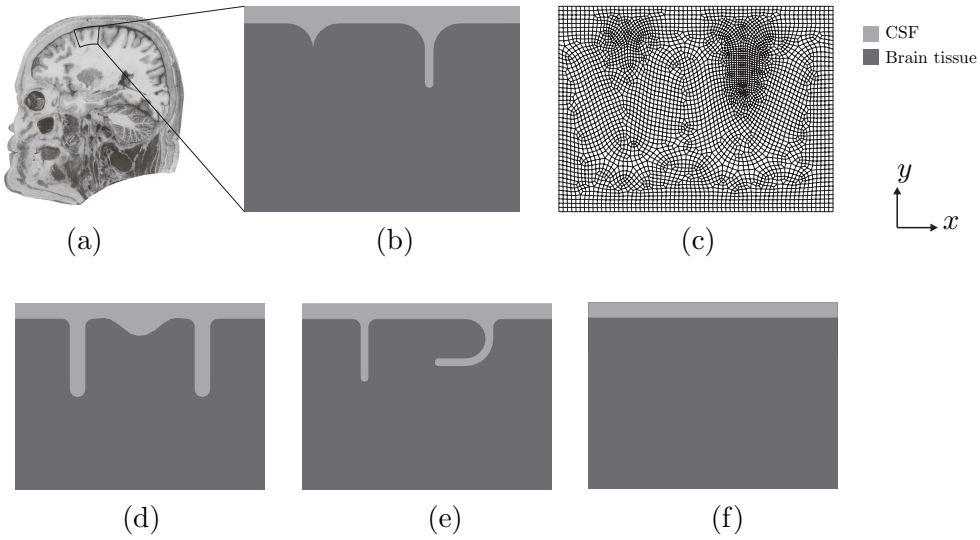

Figure 2.2: (a) Sagittal cross-section of a human head (adapted from Mai et al. [105]). (b) Heterogeneous geometry 1 and (c) its spatial discretization. (d) Heterogeneous geometry 2. (e) Heterogeneous geometry 3. (f) Homogeneous geometry.

influence for the used loading conditions. The same assumption is used for the arachnoid trabeculae, which extend from the arachnoid to the pia mater and are less existent inside the sulci [22]. The first geometry has one narrow sulcus on the right hand side and a small part of a sulcus on the left hand side. The second geometry contains two deeper and wider sulci than the other two geometries. The third geometry consists of one vertical sulcus and one partly horizontal sulcus, where vertical and horizontal refer to the x- and y-direction, respectively. These geometries, which represent typical stylized shapes of the cerebral cortex, are based on the topological studies by Mai et al. [105]. The left and right boundaries of the models are chosen to be periodic, i.e., the internal geometries near the opposite boundaries match. The periodicity of the boundary conditions will be explained further on. The models do not distinguish between gray (cerebral cortex) and white matter. In Figure 2.2f, the homogeneous model is shown. Similar to the heterogeneous models, it also consists of CSF and brain tissue, but it does not contain any gyri and sulci. The outer dimensions of each model are

32 mm by 24 mm. The meshes consist of bi-linear, quadrilateral, reduced integration elements with hourglass control. The heterogeneous models also contain a small number of triangular elements. The total number of elements of the heterogeneous models ranges from 4243 to 4533 elements. The homogeneous geometry consists of 3072 elements.

2.2.2 Material properties

For the material properties of the CSF, a nearly incompressible, low shear modulus elastic solid has been assumed, since the shear stress in the brain tissue due to the applied loading conditions is estimated to be about a factor 10^4 higher than that in the CSF. The material properties are listed in Table 2.1. The shear modulus of CSF is estimated from the loading conditions that are described further on by using $G = \frac{\eta\dot{\gamma}}{\gamma}$, in which G is the elastic shear modulus, η is the viscosity, γ is the estimated shear strain, and $\dot{\gamma}$ is the estimated shear rate. Because two different loading conditions have been used, also two different estimates for the CSF shear modulus have been used. However, with these shear moduli being much lower than that of the brain tissue, the exact values of these estimates do

Table 2.1: Linear material parameters.

Material	Bulk modulus (GPa)	Shear modulus (Pa)	Time constant (s)
CSF	2.2	0.036[a]	∞
		0.12[b]	∞
Brain tissue	2.5	182.9	∞
		9884	0.00013
		835.5	0.012
		231.2	0.35
		67.1	4.62
		3.61	12.1
		2.79	54.3

[a] Shear modulus in case of loading condition A.

[b] Shear modulus in case of loading condition B.

not affect the outcome of this study. The bulk modulus is obtained from literature [44,45].

The material properties of the brain tissue are described by a non-linear viscoelastic constitutive model that has been developed by Hrapko et al. [49]. This model was found to accurately describe the response of brain tissue for large deformations in both shear and compression. This model is extended here to account for compressibility.

The constitutive model consists of an elastic part, denoted by the subscript e, and a (deviatoric) viscoelastic part, denoted by the subscript ve, with N viscoelastic modes. The total Cauchy stress tensor $\boldsymbol{\sigma}$ is written as

$$\boldsymbol{\sigma} = \boldsymbol{\sigma}_e^h + \boldsymbol{\sigma}_e^d + \sum_{i=1}^{N} \boldsymbol{\sigma}_{ve_i}^d, \tag{2.1}$$

in which the superscripts h and d denote the hydrostatic and the deviatoric part, respectively. For simplicity, the subscript i indicating the number of the viscoelastic mode will be omitted from this point on. The hydrostatic part of Equation 2.1 is defined as

$$\boldsymbol{\sigma}_e^h = K(J-1)\boldsymbol{I}, \tag{2.2}$$

where K is the bulk modulus and $J = \det(\boldsymbol{F})$ is the volume change ratio.

The deviatoric elastic mode describes a non-linear response to the deformation gradient tensor $\boldsymbol{F}$, which is given by

$$\begin{aligned}\boldsymbol{\sigma}_e^d =& \frac{G_\infty}{J}\left[(1-A)\exp\left(-C\sqrt{b\tilde{I}_1 + (1-b)\tilde{I}_2 - 3}\right) + A\right] \\ & \left[b\tilde{\boldsymbol{B}}^d - (1-b)(\tilde{\boldsymbol{B}}^{-1})^d\right],\end{aligned} \tag{2.3}$$

where G_∞ is the elastic shear modulus, $\tilde{\boldsymbol{B}} = J^{-\frac{2}{3}}\boldsymbol{B}$ is the isochoric part of the Finger tensor $\boldsymbol{B}$, and $\tilde{I}_1$ and $\tilde{I}_2$ are the first and second invariant of the isochoric Finger tensor $\tilde{\boldsymbol{B}}$, respectively. A, C, and b are fitting parameters describing the non-linearity of the elastic response.

The third term on the right hand side of Equation 2.1 consists of the summation of the viscoelastic modes. The deformation gradient tensor $\boldsymbol{F}$ is

partitioned into an elastic deformation gradient tensor $\boldsymbol{F}_e$ and a viscous deformation gradient tensor $\boldsymbol{F}_v$ by assuming multiplicative decomposition [106,107]:

$$\boldsymbol{F} = \boldsymbol{F}_e \cdot \boldsymbol{F}_v. \tag{2.4}$$

The decomposition involves a fictitious intermediate state, which could exist after application of merely the viscous deformation gradient tensor $\boldsymbol{F}_v$. This is the stress-free state, which after application of the elastic deformation tensor $\boldsymbol{F}_e$ transforms into the final state. The third term on the right hand side of Equation 2.1 describes the viscoelastic contribution to the stress as follows:

$$\boldsymbol{\sigma}_{ve}^{d} = \frac{G}{J}\left[a\tilde{\boldsymbol{B}}_e^{d} - (1-a)(\tilde{\boldsymbol{B}}_e^{-1})^{d}\right], \tag{2.5}$$

with G the shear modulus, $\tilde{\boldsymbol{B}}_e = J^{-\frac{2}{3}}\boldsymbol{B}_e$ the isochoric part of the elastic Finger tensor $\boldsymbol{B}_e$, and a a fitting parameter.

The viscous deformation $\boldsymbol{F}_v$ is assumed to be volume-invariant, i.e., $\det(\boldsymbol{F}_v) = 1$ and $J_e = \det(\boldsymbol{F}_e) = J$. The viscous rate of deformation tensor is calculated from the flow rule as

$$\boldsymbol{D}_v = \frac{\boldsymbol{\sigma}_{ve}^{d}}{2\eta(\tau)}, \tag{2.6}$$

where the dynamic viscosity η is a function of the scalar equivalent stress measure $\tau = \sqrt{\frac{1}{2}\boldsymbol{\sigma}^{d} : \boldsymbol{\sigma}^{d}}$, for which the Ellis model is adopted:

$$\eta(\tau) = \eta_\infty + \frac{\eta_0 - \eta_\infty}{1 + \left(\frac{\tau}{\tau_0}\right)^{(n-1)}}, \tag{2.7}$$

with subscripts 0 and ∞ denoting the initial and infinite values, respectively. The initial value for the viscosity is defined as $\eta_0 = G\lambda$, whereas the infinite viscosity is defined as $\eta_\infty = k\eta_0$.

Although differences between the material properties of the gray and white matter may exist, these differences are not well characterized. Therefore, no distinction between gray and white matter has been made in this study,

except for the investigation of the influence of varying the material properties of gray matter with respect to those of white matter (see Section 2.4 Discussion and conclusions). For simulating a head impact situation representative of road traffic accidents, an extra viscoelastic mode with a smaller time constant has been added to the behavior as characterized by Hrapko et al. [49]. The extra mode [57] is based on the experimental data from Hrapko and co-workers in combination with the data by Shen et al. [50]. The linear material properties are listed in Table 2.1. The values of the non-linear viscoelastic parameters are shown in Table 2.2.

Table 2.2: Non-linear material parameters for brain tissue.

Elastic			Viscous		
A	=	0.73	τ_0	=	9.7 Pa
C	=	15.6	n	=	1.65
a	=	1	k	=	0.39
b	=	1			

2.2.3 Boundary conditions

The boundary conditions have been chosen such that they represent the biomechanical influences of the surroundings on the cerebral cortex model. Figure 2.3 shows the labeling of the corner nodes and boundaries. The symbols x and y denote the components of position vector $\vec{x}$ with respect to a Cartesian vector basis $(\vec{e}_x, \vec{e}_y)$, whereas u and v are the components of

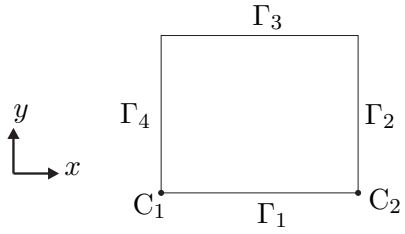

Figure 2.3: Labeling of corner nodes and boundaries.

the displacement vector $\vec{u}$ with respect to this basis.

The Young's modulus of the cranium is much higher than that of brain tissue [49,108]. Still, in a contact loading situation of the head, the deformation of the skull may be important. In this study, however, only inertial loading of the head is considered and therefore the cranium is assumed to be rigid. The cranium is incorporated in the boundary conditions at Γ_3. Because of the low shear modulus of the CSF, the influence of the rigid constraint associated with the cranium at boundary Γ_3 in the x-direction can be neglected. Provided no rotation of the model occurs, the constraint equation for all nodes on boundary Γ_3 is

$$v|_{\Gamma_3} = v_{\mathrm{s}}, \tag{2.8}$$

with v_{s} the vertical displacement of the skull.

The boundaries Γ_2 and Γ_4 are subjected to periodic boundary conditions [109]:

$$\vec{u}|_{\Gamma_2} - \vec{u}|_{\Gamma_4} = \vec{u}|_{\mathrm{C}_2} - \vec{u}|_{\mathrm{C}_1}. \tag{2.9}$$

These constraints imply that throughout the deformation process the shapes of the opposite boundaries, Γ_2 and Γ_4, remain identical to each other, while the tractions on opposite boundaries are opposite to satisfy stress continuity, which can be written as

$$\boldsymbol{\sigma} \cdot \vec{n}_2 = -\boldsymbol{\sigma} \cdot \vec{n}_4, \tag{2.10}$$

with $\boldsymbol{\sigma}$ the Cauchy stress tensor and $\vec{n}_i$ the unit outward normal vector of boundary Γ_i.

The lower boundary, Γ_1, of the brain tissue in the model lies adjacent to brain tissue in neighboring regions. Therefore, boundary Γ_1 has to be constrained accordingly. The applied constraint on Γ_1 is obtained by tying all nodal displacements on Γ_1 to a linear interpolation between the displacements of corners C_1 and C_2. For any node on boundary Γ_1, this results in

$$\vec{u}|_{\Gamma_1} = \vec{u}|_{\mathrm{C}_1} + \frac{|| \vec{x}_0|_{\Gamma_1} - \vec{x}_0|_{\mathrm{C}_1} ||}{|| \vec{x}_0|_{\mathrm{C}_2} - \vec{x}_0|_{\mathrm{C}_1} ||} \left(\vec{u}|_{\mathrm{C}_2} - \vec{u}|_{\mathrm{C}_1} \right), \tag{2.11}$$

with the subscript 0 denoting the initial configuration. The displacements of corner nodes C_1 and C_2 are prescribed and calculated from the applied

loading conditions.

The loading conditions of the cerebral cortex model (micro-level in Figure 2.4) are based on the loading conditions that have been used by Brands et al. [41] for a three-dimensional numerical head model (macro-level in Figure 2.4). In that model, an eccentric rotation has been applied to the skull to simulate an angular head acceleration around the neck-shoulder joint in the sagittal plane in the anterior-posterior direction. The eccentricity has been chosen to represent a typical neck length. The axis of rotation has been positioned at 155 mm below the anatomical origin, i.e., the ear hole projected to the sagittal plane. The rotation of the head model consists of two successive sine functions that describe the angular acceleration:

$$0 \text{ s} < t \leq 0.010 \text{ s} \quad : \quad \dot{\omega}(t) = 250\pi \sin\left(100\pi t\right), \tag{2.12}$$

$$0.010 \text{ s} < t \leq 0.030 \text{ s} \quad : \quad \dot{\omega}(t) = -125\pi \sin\left(50\pi(t - 0.010)\right). \tag{2.13}$$

In Equations 2.12 and 2.13, the angular acceleration $\dot{\omega}$ is given in rad s^{-2}.

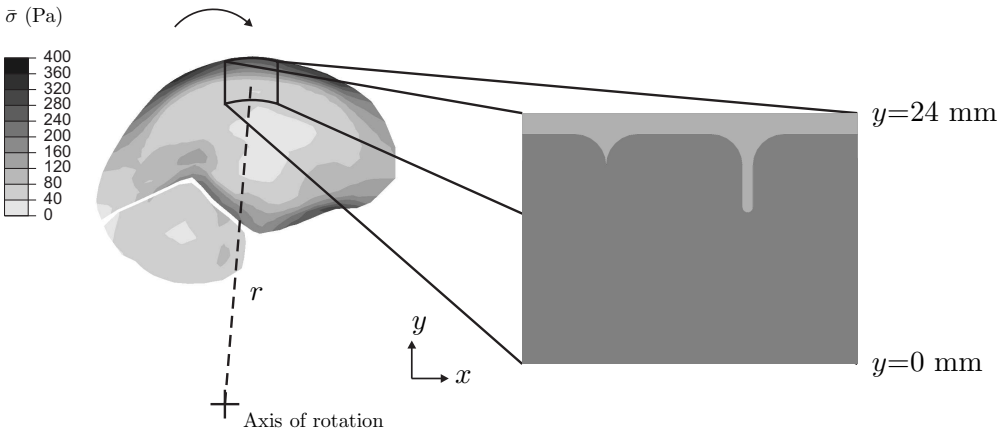

Figure 2.4: The loading conditions of the cerebral cortex model (micro-level) are derived from the region of interest in a parasagittal cross-section (15 mm offset from the midsagittal plane) of the head model (macro-level). Shown at the macro-level is the equivalent stress field of the head model at 10 ms.

The loading conditions are applied to the cerebral cortex model by means of body forces. In all integration points of the elements in the model, a non-uniform body force is imposed that reversely simulates the inertial forces:

$$\vec{q}(\vec{x},t) = \rho(\vec{x})\,\ddot{u}(y,t)\vec{e}_x, \tag{2.14}$$

in which $\vec{q}$ represents the distributed load per unit of volume, ρ is mass density, t is time, and $\ddot{u}$ refers to the acceleration in the x-direction that is represented by these body forces. Note that for the head model the loading conditions contain an angular component, whereas the cerebral cortex model uses translational loading conditions. Because only a small part of the head is modeled and because of the small rotation of the head model with a maximum of 4°, the loading of the cerebral cortex model is assumed to be translational in x-direction only.

The loading conditions of the cerebral cortex model, i.e., the representative accelerations $\ddot{u}(y,t)$, are calculated from the head model (from the region indicated in Figure 2.4) in two different approaches:

A. In the first approach, the input accelerations of the head model are used to define the loading condition of the cerebral cortex model. This approach will be referred to as loading condition A.

   The translational acceleration $\ddot{u}$ can be calculated using

   $$\ddot{u}(y,t) = \dot{\omega}(t)\,r(y), \tag{2.15}$$

   with $\dot{\omega}$ the angular acceleration, which is defined by Equations 2.12 and 2.13, and r the radius from the axis of rotation (neck-shoulder) in the head model to a point in the region of interest. The radius r is a function of the y-position in the cerebral cortex model. It varies between $r(0) = 0.251$ m at boundary Γ_1 to $r(0.024) = 0.275$ m at Γ_3. The accelerations $\ddot{u}$ at Γ_1 and Γ_3 are depicted in Figure 2.5a. All other accelerations are interpolated linearly between these two boundaries, thereby creating a gradient across the height of the model. The acceleration gradient is important for the resulting shear stresses. Figure 2.5b shows the acceleration profile of the cerebral cortex model. The accelerations are used to calculate the body forces as a function of both time and y-position.

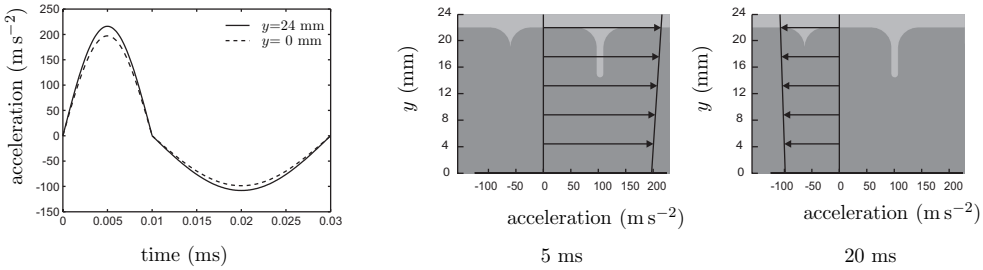

(a) (b)

Figure 2.5: Loading condition A. (a) Acceleration at the upper and lower boundary of the cerebral cortex model. (b) Acceleration profiles at different times.

The disadvantage of this loading condition is that a spatially constant acceleration gradient is assumed and therefore it does not account for the influence of the geometry of the cranium. To account for the geometry of the head, another loading condition has been developed that is described next.

B. The second approach, loading condition B, uses output accelerations from a global head model simulation as the input of the cerebral cortex model. For this, a modified version of the head model, as used by Brands et al. [41], has been employed in the simulation code Madymo, in which the constitutive model for brain tissue by Hrapko et al. [49] has been implemented. The accelerations obtained from the region inside the box in Figure 2.4 from the head model are imposed on the cerebral cortex model. Hence, the influence of the geometry of the head is modeled indirectly by means of an acceleration profile that is obtained from the head model.

   The displacements of the brain tissue in the head model in the field of interest are almost entirely in the x-direction justifying the assumption of inertial loading (of the cerebral cortex model) in the x-direction only. In Figure 2.6, the acceleration profiles as a function of the y-position are shown at 5 , 10, and 20 ms. Similar to loading condition A, the accelerations are used to calculate the body forces as a function of both time and y-position.

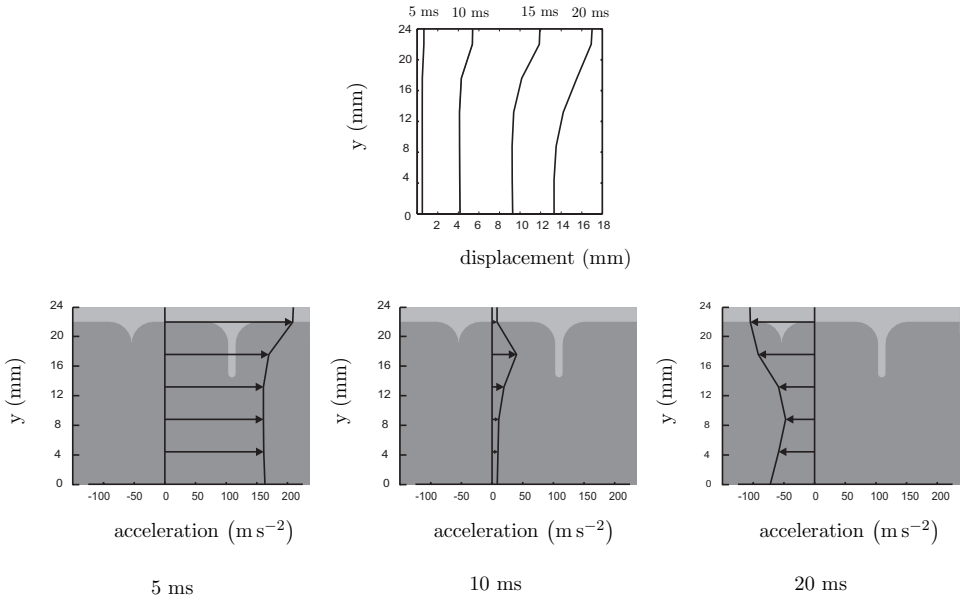

Figure 2.6: Loading condition B: displacement (top) and acceleration (bottom) profiles derived from the output of the head model.

In order to quantify the influence of the morphologic heterogeneities, the equivalent stress $\bar{\sigma} = \sqrt{\frac{3}{2}\boldsymbol{\sigma}^d : \boldsymbol{\sigma}^d}$ is used, in which $\boldsymbol{\sigma}^d$ is the deviatoric part of the Cauchy stress tensor $\boldsymbol{\sigma}$. The equivalent stress is chosen, because the simulations are based on an angular acceleration of the head, in which deviatoric stresses are considered to be the most important [102]. The maximum principal strain is considered important as well with respect to diffuse axonal brain injury [59,102]. Therefore, also the maximum principal logarithmic strain was used to quantify the influence of the morphologic heterogeneities.

2.3 Results

Figure 2.7 depicts the development in time of the equivalent stress fields for the homogeneous model (top row) and the heterogeneous models from

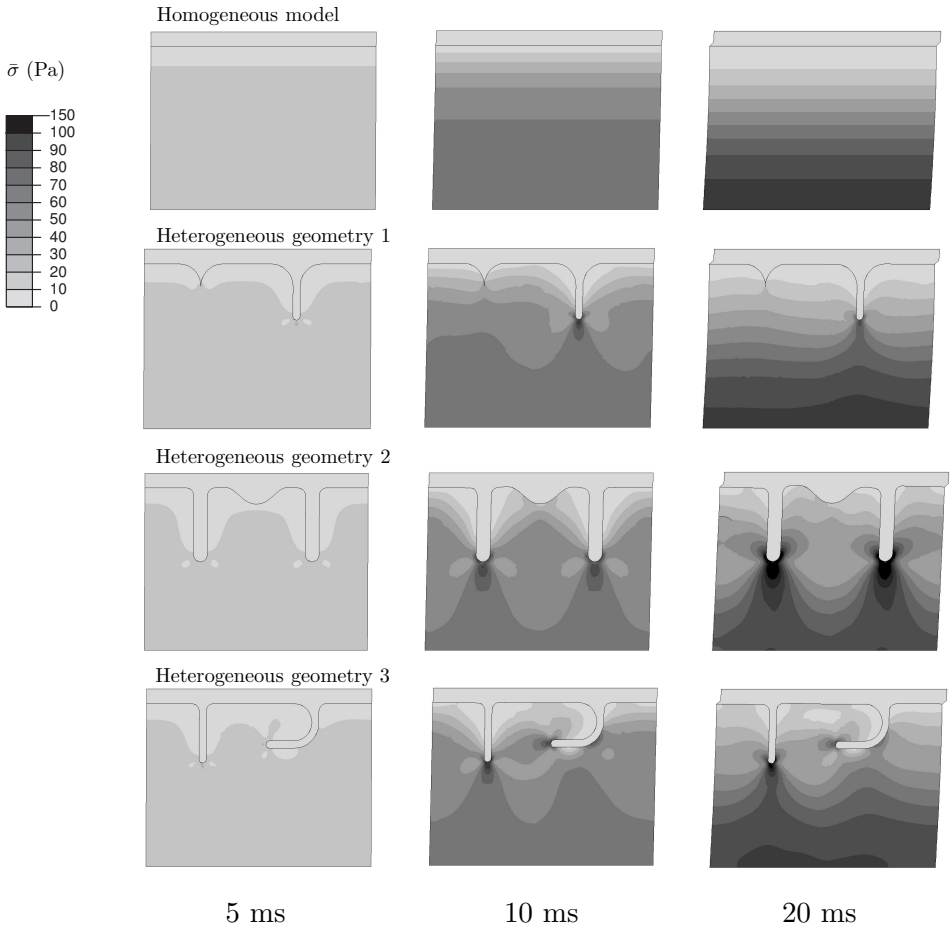

Figure 2.7: The equivalent stress fields as a result of loading condition A.

the simulation with loading condition A. Stress concentrations are present in the heterogeneous models at the surface of the brain tissue between two gyri at 5, 10 and 20 ms. Near boundary Γ_1, all heterogeneous models have lower equivalent stresses compared to the homogeneous model at 20 ms.

In order to obtain a good comparison of the results for all geometries during the complete simulation time, the maximum and mean equivalent stress from simulations with loading condition A are shown in Figure 2.8 as a

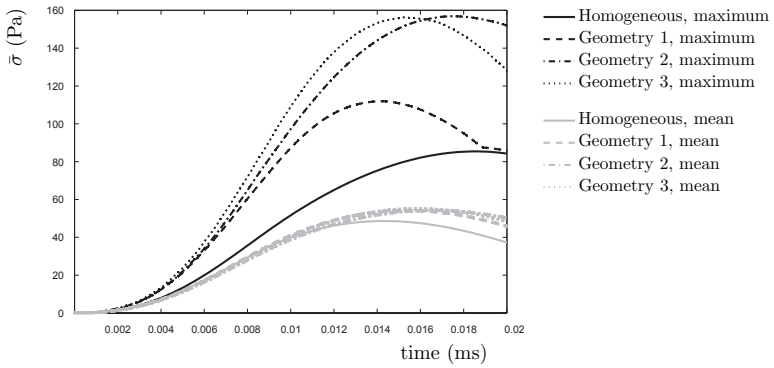

Figure 2.8: Maximum and mean equivalent stress for the heterogeneous and homogeneous models as a result of loading condition A.

function of time. It shows the stresses in the brain tissue only. It can be noticed that the heterogeneous models have a higher maximum equivalent stress than the homogeneous model. Among the heterogeneous configurations, geometry 1 causes a noticeably lower maximum equivalent stress of 112 Pa compared to geometries 2 and 3, with a maximum equivalent stress of approximately 156 Pa. The large maximum equivalent stress in heterogeneous geometry 2 lasts longer than the stresses of the other geometries. The maximum equivalent stress of the homogeneous model reaches a value of 80 Pa. The mean equivalent stresses are nearly the same for all geometries.

To investigate the influence of the heterogeneities, the equivalent stress of the cerebral cortex in the heterogeneous models is taken relative to that of the homogeneous model. For the maximum equivalent stress, this will be done by taking the maximum values, whereas for the mean equivalent stress, this will be done by taking the time averaged values. The maximum equivalent stress of the heterogeneous models 1, 2, and 3 is 1.31, 1.84, and 1.83 times higher than the homogeneous model, respectively. The mean equivalent stress of the heterogeneous models 1, 2, and 3 with respect to the homogeneous model is 1.09, 1.08, and 1.10, respectively.

The equivalent stress fields obtained with loading condition B are displayed in Figure 2.9. During the beginning of the simulation, the equivalent stress

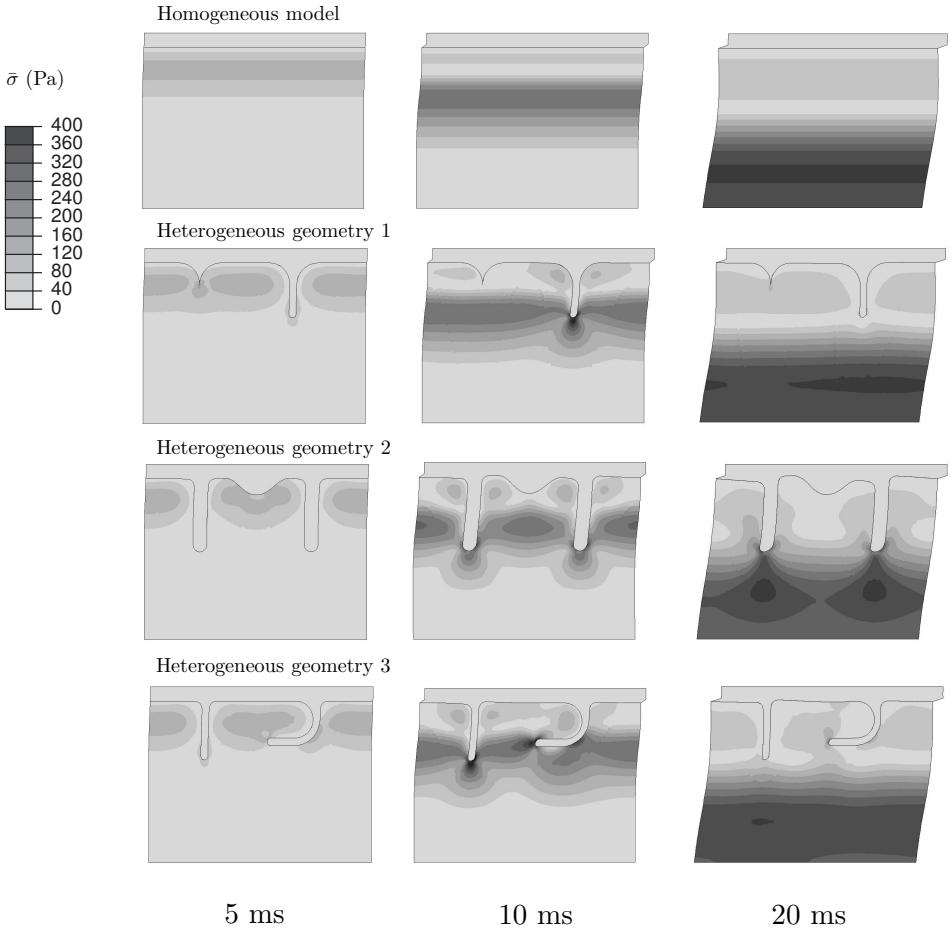

Figure 2.9: The equivalent stress fields as a result of loading condition B.

fields in the brain tissue are comparable for all models. When the field of higher equivalent stress moves downwards, the heterogeneities result in local peak stress concentrations, which can be seen at 10 ms for geometries 1 and 3. Later on, at 20 ms, the heterogeneous geometries 1 and 3 have less influence on the equivalent stress fields. The differences of geometry 2 with respect to geometries 1 and 3 are a consequence of the deeper sulci in geometry 2.

The maximum and mean equivalent stress of the cerebral cortex as a function of time obtained with loading condition B is shown in Figure 2.10. The maximum equivalent stress is higher for the heterogeneous models than for the homogeneous models, but not for the complete duration of the simulation. After about 10 to 15 ms, the maximum equivalent stress of the heterogeneous models drops to approximately the same magnitude as the one obtained for the homogeneous model. For the heterogeneous models, the maximum equivalent stress reaches values of approximately 470, 565, and 624 Pa for geometries 1, 2, and 3, respectively. The homogeneous model has a maximum equivalent stress reaching 325 Pa. Also, the moment in time at which the maximum occurs differs from one geometry to the other. The mean equivalent stress values of all the geometries are similar.

To quantify the influence of the heterogeneities, the equivalent stress of the brain tissue of the heterogeneous models is taken relative to the homogeneous model in the same manner as described previously for loading condition A. The maximum equivalent stress of the heterogeneous models 1, 2, and 3 has increased by 1.44, 1.74, and 1.92 with respect the homogeneous model, respectively. The mean equivalent stress of the heterogeneous models 1, 2, and 3 is 0.97, 0.99, and again 0.99 relative to the homogeneous model, respectively.

The distribution of maximum principal strains for loading condition B at

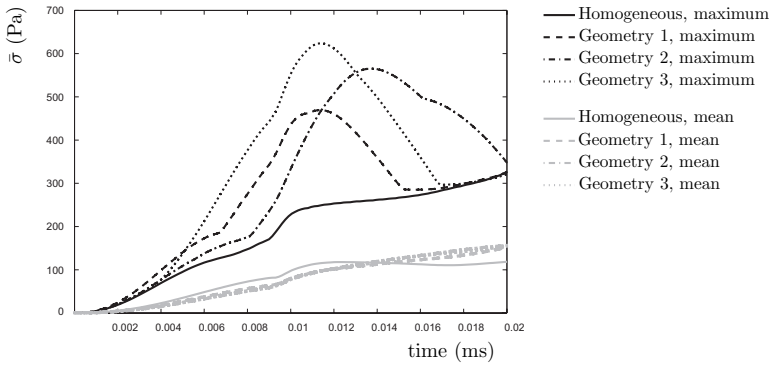

Figure 2.10: Maximum and mean equivalent stress for the heterogeneous and homogeneous models as a result of loading condition B.

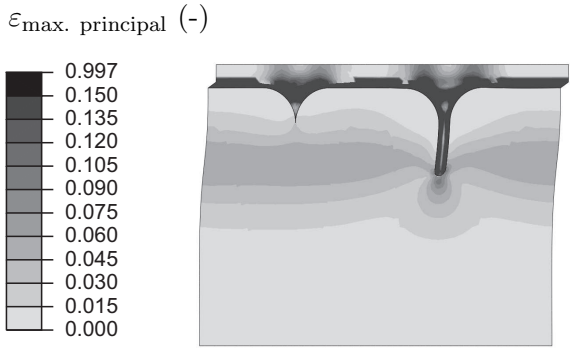

Figure 2.11: The maximum principal logarithmic strain field as a result of loading condition B at 10 ms.

10 ms is shown in Figure 2.11. One can notice that a concentration of maximum principal strains at 10 ms occurs in the same location as the equivalent stress concentration at 10 ms (Figure 2.9), both in case of loading condition B. The same method for the quantification of the influence of the heterogeneities is used, but with the maximum principal strain instead of the equivalent stress. For the simulations with loading condition A, the peak maximum principal strain in the brain tissue of the heterogeneous models 1, 2, and 3 has increased with respect to the homogeneous model by 1.22, 1.92, and 1.80, respectively. If loading condition B was used, the increases were 1.43, 1.84, and 1.90, respectively.

2.4 Discussion and conclusions

In this study, the influences of the heterogeneities in the cerebral cortex were investigated. This was done with FE models of several different geometries from small detailed parts of the cortex. In a preliminary study, the boundary constraints were tested. The loading conditions were derived from a numerical head model.

In order to determine which constraints on the boundaries would represent the surroundings best, a preliminary study was conducted in which several different constraints were applied to boundaries Γ_1 and Γ_3. The different

conditions on boundary Γ_3, i.e., rigid constraint or slip-condition in the x-direction, did not contribute to differences in the results of the brain tissue. This was probably caused by the low shear modulus of the CSF. For boundary Γ_1, several different boundary conditions were tested and compared to the results of models with the same width, but with twice the height of the models in this study. By comparing the 'normal' and the 'high' models, the boundary condition at boundary Γ_1 that represented adjacent brain tissue could be determined. The periodic boundary condition that were applied to boundaries Γ_2 and Γ_4, were used because of the assumed periodicity in the cerebral cortex.

Since the loading conditions were dynamic they could not be applied to the model by directly imposing a deformation, which would induce boundary effects. For this reason, an indirect deformation was imposed by means of body forces. This approach worked well for the first 20 ms of the simulation, which had a total duration of 30 ms. After 20 ms the deformations of the brain tissue differed from the deformations derived from the head model that were indirectly applied to the model (Figures 2.6 and 2.9). Therefore, only the first 20 ms of the simulation are considered to be realistic.

Loading condition A was derived from the acceleration pulse that has been applied to a head model [41,110]. The equivalent stress fields of the homogeneous models caused by loading condition A (Figure 2.7) showed no similarities to the equivalent stress field of the head model (Figure 2.4). Provided that the equivalent stress field of the head model is realistic, loading condition A can be considered unrealistic. Loading condition B was obtained from the resulting accelerations in the region of interest of the head model. The equivalent stress fields of the homogeneous models from simulations with loading condition B (Figure 2.9) were approximately similar to the stress fields in the corresponding region of the head model (Figure 2.4) during the first 20 ms. Nevertheless, differences in the equivalent stress fields existed at the surface of the cortex. This is due to the CSF layer in the cerebral cortex model being described elastically with a low shear modulus, as opposed to the head model, which contains a relatively stiff CSF/dura layer. In spite of all these obvious differences, by comparing these two loading conditions, it was shown that the different loading conditions have hardly any effect on the relative mean and maximum equivalent stress and the relative peak maximum principal logarithmic strain. Hence,

the mechanical influences of the heterogeneities of the cerebral cortex seem to be independent of the loading conditions.

The constitutive model for brain tissue was based on experiments on porcine white matter [49]. This was used as a substitute for human brain tissue, as it was readily available and it allowed to conduct experiments with a shorter post-mortem time [110,111]. Experiments conducted by Prange et al. [51] on fresh human brain tissue indicated that its mechanical properties are approximately 30% stiffer than those of fresh porcine brain tissue. Although the constitutive model for brain tissue in the cerebral cortex model was not based on human brain tissue, the geometries of the models were based on the human cerebrum. This assumption is expected to have more effect on the absolute equivalent stress than on the relative equivalent stress, which is dominated by the heterogeneities of the model. Furthermore, no distinction between the mechanical properties of white and gray matter was made, so that the material properties of the cerebral cortex, which consists of gray matter, were based on experiments on white matter, as well. In their results, Prange et al. [51] found differences between the material properties of the corpus callosum, i.e., the white matter that connects the two cerebral hemispheres, and the cerebral cortex, but not between the corona radiata, i.e., the white matter that lies inferior to the cerebral cortex, and the cerebral cortex. Nevertheless, in several other studies of head and brain models, different material properties were used for gray and white matter based on the assumption that white matter was more fibrous than gray matter [44,45,102,112]. Therefore, simulations of the cerebral cortex model with shear moduli for gray matter ranging from 75% to 125% with respect to the shear moduli white matter were conducted as well. The results of these simulations indicated that the material properties had an effect on the magnitude of the equivalent stress, but not on the regions in which the peak equivalent stress was observed. The equivalent stress of the heterogeneous model relative to the homogeneous model was hardly affected by the different material properties.

In this model, the meninges and the blood vessels were considered to have no mechanical influence on the cerebral cortex for the used loading conditions. Although it was suggested in literature that the pia mater [113] and the pia-arachnoid complex [114] can have a mechanical influence on the brain tissue during an impact, it is still not clear if it would affect the

influence due to the gyrification of the cerebral cortex. However, it is expected that stress and strain concentrations near the sulci will also occur in the presence of the meninges. In a study performed by Ho and Kleiven [99], it was found that the vasculature of the brain can be neglected, as far as the mechanical influences are concerned in a head model not containing the gyrification of the cortex.

In order to validate this model, a comparison with physical experiments is required. However, data of physical experiments at a typical length scale of this level is rather limited. Parallel to this study, the results of physical experiments, in which brain slices have been accelerated, showed increased equivalent strains near the sulci [115]. In a later study conducted by Ho and Kleiven [116], using an FE head model with a detailed geometry containing the sulci, it was shown that the sulci caused local strain concentrations, although the overall response involved a decrease of the strain values. Furthermore, some studies showed that angular accelerations of the head induce high stress concentrations in and near the cerebral cortex [30,31]. Another method of validation can be performed by comparing the results of the model to clinically observed injury. It has been shown that small cortical infarcts exist in diffuse brain injury at the bottom of the sulci [117]. This is in accordance with the locations of the high stress and strain regions in the cerebral cortex model.

The two loading conditions and the different geometries resulted in different equivalent stress fields. The simulations with loading condition A resulted in a lower mean and maximum equivalent stress compared to the simulations with loading condition B. However, relative to the homogeneous model, it was observed that the equivalent stress was almost independent of the different loading conditions used in this study. The differences between the several heterogeneous geometries had more influence on the relative mean and maximum equivalent stress. The morphologic heterogeneities of the cerebral cortex led to an increase of the maximum equivalent stress by a factor of about 1.3 to 1.9, depending mostly on the geometry, whereas the relative mean equivalent stress values of all the geometries were 1.1 and 1.0 for loading condition A and B, respectively. Furthermore, the peak maximum principal logarithmic strain was increased by a factor of about 1.2 to 1.9 due to the morphologic heterogeneities of the cerebral cortex. This is a strong indication that predictions of brain injury obtained from head

models with a homogeneous cerebrum should be interpreted with care. To obtain a more accurate assessment of injury, the influence of the morphologic heterogeneities in the cerebral cortex should be accounted for.

3

Chapter three

Micromechanics of Diffuse Axonal Injury

Multiple length scales are involved in the development of traumatic brain injury, where the global mechanics of the head level are responsible for local physiological impairment of brain cells. In this study, a relation between the mechanical state at the tissue level and the cellular level is established. A model has been developed that is based on pathological observations of local axonal injury. The model contains axons surrounding an obstacle (e.g., a blood vessel or a brain soma). The axons, which are described by an anisotropic fiber reinforced material model, have several physically different orientations. The results of the simulations reveal axonal strains being higher than the applied maximum principal tissue strain. For anisotropic brain tissue with a relatively stiff inclusion, the relative logarithmic strain increase is above 60%. Furthermore, it is concluded that individual axons oriented away from the main axonal direction at a specific site can be subjected to even higher axonal strains in a stress driven process, e.g., invoked by inertial forces in the brain. These axons can have a logarithmic strain of about 2.5 times the maximum logarithmic strain of the axons in the main axonal direction over the complete range of loading directions. The results indicate that cellular level heterogeneities have an important influence on the axonal strain, leading to an orientation and location dependent sensitivity of the tissue to mechanical loads. Therefore, these effects should be accounted for in injury assessments relying on finite element head models.

Reproduced from: R.J.H. Cloots, J.A.W. van Dommelen, T. Nyberg, S. Kleiven and M.G.D. Geers (2011). Micromechanics of diffuse axonal injury: influence of axonal orientation and anisotropy. *Biomechanics and Modeling in Mechanobiology*, **10** (3), 413-422.

3.1 Introduction

Traumatic brain injury (TBI) can be caused by accidents, for instance in road traffic or sports, leading to serious health issues or even death. The incidence rate and mortality rate in Europe are estimated to be 235 and 15.4 per 100,000 of the population per year, respectively [89]. One of the most frequently occurring types of TBI is diffuse axonal injury (DAI), which is primarily involved with dynamic non-contact loads, although it is believed to occur in closed head impacts as well and is associated with widespread injury in the brain [118,119].

The most commonly used brain injury criterion, which relates brain injury to mechanical loading, in the automotive industry is the Head Injury Criterion (HIC) [92]. However, the application of HIC is limited, since it is based on experimental data of head accelerations, in which only anterior-posterior contact loading has been applied to human cadavers, not accounting for head angular accelerations or brain tissue strains and stresses. Therefore, finite element (FE) head modeling provides a more sophisticated method for assessing the likelihood of brain injury as a result of a mechanical load [41,43,45,97,98]. These models simulate the consequences of mechanical loads on the head by predicting the stress and strain inside the brain. However, at present, there is no direct link between mechanical load of the tissue and cellular injury.

To investigate the mechanophysical mechanisms of TBI, different length scales of the brain are distinguished (see Figure 3.1). At the head level, the mechanical load is applied and transmitted to and through the brain. In order to predict a true tissue stress and strain, the geometrical details of the brain are important because of the induced concentrations of stress and strain in the tissue (see Chapter 2 as well as [47,115,116]). Even more, these tissue level strains will lead to a mechanical loading of brain cells, possibly leading to physiological damage. Therefore, it is assumed that investigating the mechanical phenomena at the cellular level might provide information about the fundamental triggers of DAI. At this level, the individual brain cells and their constituting elements can be distinguished. Neurons and glial cells consist of a soma (i.e., a cell body) and processes (i.e., axons and dendrites), which extend from the soma [21,22]. Somal sizes are about 5 μm in diameter for the glial cells and often less then 10 μm for nonpyramidal

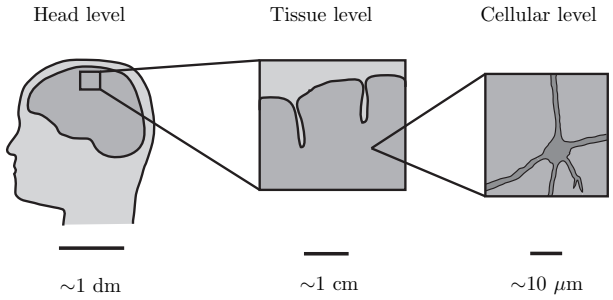

Figure 3.1: The length scales involved with TBI ranging from decimeters for the head level to micrometers at the cellular level.

cells and up to 20 μm for other cortical and hippocampal neurons [67–72]. Most of the somata of the neurons are found in the cortex from which the axons extend into other parts of the brain. Axons have a uniform diameter and can be many centimeters long, whereas dendrites taper away from the soma and rarely exceed 500 μm in length [73]. The majority of the brain tissue volume consists of axons. Even in the cerebral cortex, which is relatively rich in somata and blood vessels in comparison with other parts of the brain, about 5% to 10% consists of glial processes, 60% to 70% of neuronal processes (including their boutons and spines), 10% to 20% of somata and blood vessels, and the remaining part is the extracellular space [120–123].

Povlishock [15] found that DAI is not associated with direct mechanical tearing of axons in the white matter, but with the discrete focal impairment of axoplasmic transport leading to local axonal swelling and lobulation, which were all found at locations where the axon changed its anatomical course (e.g., near a blood vessel or a soma). Furthermore, Povlishock observed that damaged axons could be found intermingled with intact axons. These findings are still supported in more recent literature [124,125]. In the current study, it is therefore assumed that these locally occurring injuries are caused by locally increased strains, since the brain is loaded mechanically prior to injury. Furthermore, it is assumed that axonal ori-

entation and the presence of inclusions (e.g., a blood vessel or a soma) in the pathway of the axons are the main triggers of locally increased strains.

Computational mechanical modeling of the brain at the cellular level has been done to some extent [88,126–128]. These studies were mainly focused on the relation between the tissue level mechanical behavior and the cellular level structures. This study, however, focuses on injury sensitivity as a function of the micromechanical characteristics. The aim is to assess the relation between tissue level mechanical loading and cellular level injury. Since local axonal damage has been observed for DAI, it is hypothesized that locally a higher strain occurs due to geometric or mechanical heterogeneities, constituting a precursor of local damage.

3.2 Methods

In this study, a plane strain FE model that relates tissue level mechanical loads to cellular level brain injury has been developed. In the simulations, mechanical loads representing tissue level deformations have been applied on a model with a length scale that is typical for individual cells. Based on the pathological findings mentioned in the introduction, the model of interest contains typically one inclusion surrounded by axons. In order to determine which factors are critical for axonal strain concentrations, the axonal orientations and the mechanical properties are varied.

3.2.1 Geometry

The geometry of the model is based on the anatomical and pathological observations for axonal injury. The geometry contains a cylindrical inclusion (e.g., a blood vessel or a soma) with a diameter of 8 μm. It is assumed that the remaining part of the tissue consists of axons only. The interface between the inclusion and the surrounding tissue is assumed to be fully tied. The tissue surrounding the inclusion is modeled as a regular continuum where the behavior in each material point corresponds to the response of a mixture of axons. The spatial distribution of axonal orientations is either oriented or unoriented (i.e., random). For the oriented models, the axons are oriented fully uniaxially in every material point. However, the

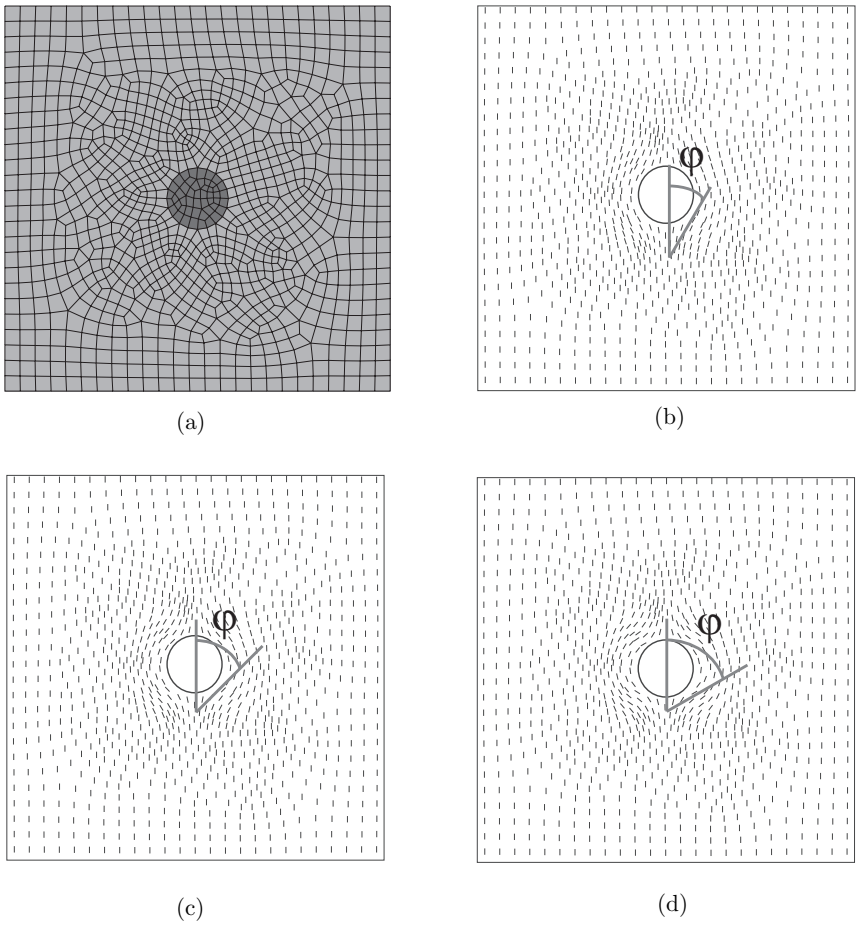

Figure 3.2: (a) Discretization and (b)-(d) axonal orientations of the model. The maximum diversion angle φ is (b) 30°, (c) 45°, and (d) 60°. The outer dimensions are 50 μm by 50 μm.

axonal orientation in different material points differs as shown in Figure 3.2. The axons are diverting from the inclusion, and the amount of diversion is defined as the maximum angle φ between the local axon orientation and the main axonal direction in the far field. To investigate the influence of the diversion angle, it is chosen to model configurations with $\varphi = 30°$,

45°, and 60°. Also, analytical computations of the fiber-reinforced material model, which will be explained later, are used, representing a homogeneous geometry (i.e., without an inclusion) with oriented fibers. This situation is referred to as $\varphi = 0°$. To study the effect of the main axonal orientation, the principal loading direction is varied with respect the main axonal orientation, as will be detailed further on.

3.2.2 Boundary conditions

Since the part of the brain that is modeled here is in reality surrounded by adjacent brain tissue, periodic boundary conditions are adopted to include that influence [109]:

$$\vec{u}|_{\Gamma_{34}} - \vec{u}|_{\Gamma_{12}} = \vec{u}|_{c_4} - \vec{u}|_{c_1}, \tag{3.1}$$

$$\vec{u}|_{\Gamma_{23}} - \vec{u}|_{\Gamma_{14}} = \vec{u}|_{c_2} - \vec{u}|_{c_1}, \tag{3.2}$$

where c_i are the corner nodes, Γ_{ij} represent the boundaries of the model as shown in Figure 3.3 and $\vec{u}$ represents the displacement vector. An isochoric overall deformation is applied, in which the principal strain direction is varied. This direction is indicated by the angle θ with respect to the global 1-direction of the model that corresponds with the main axonal direction. The deformation gradient tensor prescribed is defined as

$$\bar{\boldsymbol{F}} = \bar{\lambda}\vec{m}_1\vec{m}_1 + \frac{1}{\bar{\lambda}}\vec{m}_2\vec{m}_2 + \vec{m}_3\vec{m}_3, \tag{3.3}$$

in which $\bar{\lambda} = 1.01$ is the globally applied stretch ratio and the vectors $\vec{m}_i$ (for $i = 1, 2, 3$) can be expressed in terms of the Cartesian vectors $\vec{e}_j$ (for $j = 1, 2, 3$) and the angle θ. The deformation gradient tensor is imposed on the unit cell in a standard manner through the displacements of the corner nodes c_1, c_2, and c_4. This way, only the average deformation of the model is prescribed, whereas the exact local deformations follow from the equilibrium conditions and the heterogeneity of the model.

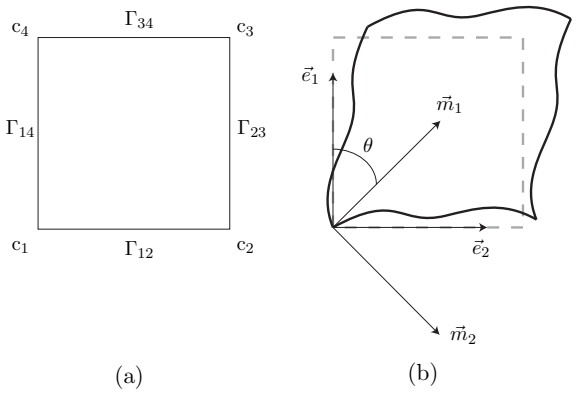

Figure 3.3: (a) Labeling of the corner nodes and the boundaries. (b) Schematic representation of the deformation defined by the loading angle θ and the periodic boundary conditions.

3.2.3 Mechanical properties

The mechanical behavior of brain tissue is not homogeneous throughout the brain. One marked aspect of the mechanical properties that shows interregional variation is the degree of anisotropy. Areas in which the axons are more aligned have a higher fractional anisotropy (FA), which is a measure to quantify the morphological anisotropy [129], as well as a higher mechanical anisotropy [51,57,130]. Inside each axon, fibers are aligned in the direction of the axon itself [73]. These fibers are the neurofilaments and they provide the axon its mechanical strength. The mechanical response of the brain tissue with a fibrous microstructure is described with the following anisotropic strain energy potential [131]:

$$W = \frac{G}{2}(\tilde{I}_1 - 3) + K\left(\frac{J^2-1}{4} - \frac{1}{2}\ln J\right) + \frac{k_1}{2k_2}\sum_{\alpha=1}^{N}\left(e^{k_2\langle\tilde{E}_\alpha\rangle^2} - 1\right), \quad (3.4)$$

where the third term on the right hand side is the Holzapfel-Gasser-Ogden form [132] with

$$\tilde{E}_\alpha = \kappa(\tilde{I}_1 - 3) + (1 - 3\kappa)(\tilde{I}_{4\alpha} - 1). \quad (3.5)$$

In Equation 3.4, W is the strain energy per unit of reference volume, K is the bulk modulus, G is the shear modulus N is the number of fiber families, $\tilde{I}_1$ is the first invariant of the isochoric Cauchy-Green deformation tensor, $J = \det(\boldsymbol{F})$ is the volume ratio, and k_1, k_2, and κ are material parameters for describing the behavior of the fibers. Furthermore, $\tilde{I}_{4\alpha} = \tilde{\boldsymbol{C}} : \vec{n}_{0\alpha}\vec{n}_{0\alpha}$ where $\tilde{\boldsymbol{C}} = J^{-\frac{2}{3}}\boldsymbol{C}$ is the isochoric part of the right Cauchy-Green deformation tensor $\boldsymbol{C}$ and $\vec{n}_0$ is the fiber direction vector in the reference configuration with unit length. The material parameter κ describes the dispersion of the fiber orientations around the preferred fiber direction $\vec{n}_{0\alpha}$. The two limits of κ are 0 for fully aligned fibers (i.e., full transverse anisotropy) and $\frac{1}{3}$ for randomly orientated fibers (i.e., isotropy). The Macaulay brackets $\langle\cdot\rangle$ impose $\langle\tilde{E}_\alpha\rangle$ to become 0 if $\tilde{E}_\alpha$ is negative, and therefore, the fibers contribute only in tension and not in compression. The Cauchy stress tensor is then expressed as

$$\boldsymbol{\sigma} = \boldsymbol{\sigma}^h + \boldsymbol{\sigma}^d. \tag{3.6}$$

The hydrostatic part is given by

$$\boldsymbol{\sigma}^h = \frac{K}{2}\frac{J^2-1}{J}\boldsymbol{I} \tag{3.7}$$

and the deviatoric part is

$$\boldsymbol{\sigma}^d = \frac{1}{J}\left(G\tilde{\boldsymbol{B}}^d + 2k_1\sum_{\alpha=1}^{N} e^{k_2\langle\tilde{E}_\alpha\rangle^2}\langle\tilde{E}_\alpha\rangle\left(\kappa\tilde{\boldsymbol{B}}^d + \tilde{I}_{4\alpha}(1-3\kappa)(\vec{n}_\alpha\vec{n}_\alpha)^d\right)\right), \tag{3.8}$$

where $\boldsymbol{I}$ is the unit tensor and $\tilde{\boldsymbol{B}}^d$ is the deviatoric part of the isochoric Finger tensor $\tilde{\boldsymbol{B}} = J^{-\frac{2}{3}}\boldsymbol{B}$.

The material properties of the part consisting of axons only and the corresponding geometrical conditions are summarized in Table 3.1 for three different configurations. The material properties of the fiber-reinforced oriented axons are based on the study performed by Ning et al. [58]. Also, two other configurations are used: fiber-reinforced unoriented axons and oriented axons without fiber-reinforcement. The fiber-reinforced oriented configuration results in anisotropic tissue behavior, whereas the other two

Table 3.1: Brain tissue material properties and maximum fiber diversion angle φ for three configurations.

Tissue	G (Pa)	k_1 (Pa)	κ	φ without inclusion	φ with inclusion
Fiber-reinforced with:					
- oriented axons	12.7	121.2	0	0°	30°/45°/60°
- unoriented axons	12.7	121.2	$\frac{1}{3}$	N/A	N/A
No fiber-reinforcement, but with oriented axons	12.7	0	0	0°	30°/45°/60°

configurations result in isotropic tissue behavior. For the fiber-reinforced unoriented axons, isotropy is caused by the random distribution of axons, which can be found closer to or within the cerebral cortex. For the oriented axons without fiber-reinforcement, however, the fiber contribution to the stiffness is ignored. Note that this reduces Equation 3.8 to a Neo-Hookean constitutive equation. The main reason to include the latter isotropic configuration, is to investigate the separate effects of anisotropic stiffness and oriented axonal stretching. The material model is further simplified by using one fiber family (i.e., $N = 1$) and therefore, the axons are locally fully aligned. However, the fiber orientation can be spatially heterogeneous, as described previously. Furthermore, fiber contribution to the stiffness is assumed to be linear and therefore the non-linear parameter $k_2 \to 0$ is used. With these assumptions, Equation 3.4 can be rewritten as

$$W = \frac{G}{2}(\tilde{I}_1 - 3) + K\left(\frac{J^2 - 1}{4} - \frac{1}{2}\ln J\right) + \frac{k_1}{2}\langle\tilde{E}_1\rangle^2. \tag{3.9}$$

The bulk modulus K is assumed to be constant over the whole volume of the tissue and is reported to range from 2.1 GPa [133] to 2.5 GPa, based on the velocity of the dilatational waves in brain tissue of approximately 1550 m s^{-1} measured in ultrasonic experiments [134–136]. In this study, a bulk modulus of 2.5 GPa is chosen.

The inclusion is assumed to be isotropic and its material properties are based on the surrounding tissue. In case the inclusion represents a cross-

section of a soma, which is assumed to consist of similar material as the axons, the material properties are the same as the fiber-reinforced unoriented configuration for the brain tissue (see Table 3.1). For other cases (e.g., blood vessels), the material properties of the inclusion are varied in order to investigate the mechanical influence of the inclusion stiffness on the surrounding axons.

3.2.4 Numerical approximation

The model has been developed within Abaqus 6.8-2 [131]. A geometrically nonlinear approach is adopted using a model that contains 1076 quadrilateral bilinear elements with hourglass control and reduced integration because of the near incompressibility of brain tissue.

3.2.5 Output quantities

This study is especially focussed on the local consequences of a global mechanical load on brain tissue. As mentioned previously, DAI is found to be related to discrete focal impairment of axons [15]. Therefore, a relative measure of the axonal strain with respect to a global load measure is used. The axonal strain ε is defined as the maximum logarithmic strain in the axonal direction, which is the material 1-direction for oriented axons and the maximum principal strain direction for unoriented axons. By taking the maximum principal tissue strain $\bar{\varepsilon} = \ln(\bar{\lambda})$, which is imposed on the boundaries, as the global load measure, the relative strain becomes $\hat{\varepsilon} = \frac{\varepsilon}{\bar{\varepsilon}}$.

During realistic loading conditions responsible for DAI, however, the tissue deformation is strongly driven by stress, because of the inertial forces acting on the brain. Therefore, also the maximum local strain with respect to the global normal stress difference of the tissue is considered. This measure is representative for a process driven by a uniaxial stress and is defined as $\bar{\varepsilon}_\sigma = \frac{\varepsilon}{(\bar{\sigma}_{11} - \bar{\sigma}_{22})}$, where $\bar{\sigma}_{11}$ and $\bar{\sigma}_{22}$ are the homogenized stress components in the rotated coordinate system $\{\vec{m}_1, \vec{m}_2\}$, which are computed as in [109]. This normal stress difference corresponds to the maximum in-plane shear stress. Then, the axonal strain relative to the applied stress is normalized with this quantity for a reference situation, $\check{\varepsilon}_\sigma = \frac{\bar{\varepsilon}_\sigma}{\bar{\varepsilon}_{\sigma,\mathrm{ref}}}$, where the reference

situation is the homogeneous fiber-reinforced tissue with unoriented axons. The above mentioned output measures are summarized in Table 3.2.

Table 3.2: Summary of the output measures.

Output measure	Description
$\bar{\lambda}$	applied tissue stretch
$\bar{\varepsilon} = \ln(\bar{\lambda})$	applied tissue strain
ε	maximum axonal strain
$\hat{\varepsilon} = \frac{\varepsilon}{\bar{\varepsilon}}$	maximum axonal strain relative to the applied tissue strain
$\bar{\varepsilon}_\sigma = \frac{\varepsilon}{(\bar{\sigma}_{11} - \bar{\sigma}_{22})}$	maximum axonal strain relative to the applied tissue stress
$\bar{\varepsilon}_{\sigma,\mathrm{ref}}$	reference axonal strain relative to the applied tissue stress
$\check{\varepsilon}_\sigma = \frac{\bar{\varepsilon}_\sigma}{\bar{\varepsilon}_{\sigma,\mathrm{ref}}}$	normalized maximum axonal strain relative to the applied tissue stress

Besides relative or absolute axonal strains, an invariant stress measure will be used as well to investigate the influence of the global loads. For this, the equivalent stress $\sigma^{eq} = \sqrt{\frac{3}{2}\boldsymbol{\sigma}^d : \boldsymbol{\sigma}^d}$ is used, in which $\boldsymbol{\sigma}^d$ is the deviatoric part of the Cauchy stress tensor $\boldsymbol{\sigma}$.

3.3 Results

This study is concerned with the global mechanical influences on axonal injury and therefore, the results, including the field plots, depict the tissue part that consists of axons, but not the inclusion. Figure 3.4 shows the results of the simulations with oriented fiber-reinforced axons and a maximum diversion angle of 45° at three different loading angles. For both the equivalent stress and the axonal logarithmic strain, it is obvious that the values decrease for higher loading angles. Furthermore, at the same loading angles, maximum values are located similarly for the stress and strain fields.

At a loading angle of $\theta = 0°$, all axonal strain values are positive (i.e., all the axons are stretched), whereas all axonal strain values are negative (i.e., all the axons are compressed) at $\theta = 90°$.

In Figure 3.5, the maximum relative axonal strains, which were defined previously, are plotted as a function of the loading angle for the configurations with the oriented fibers. Unoriented fiber configurations as well as the homogeneous oriented fiber configuration are not shown, because the relative strain in these cases has a value of 1 over the entire range of loading direc-

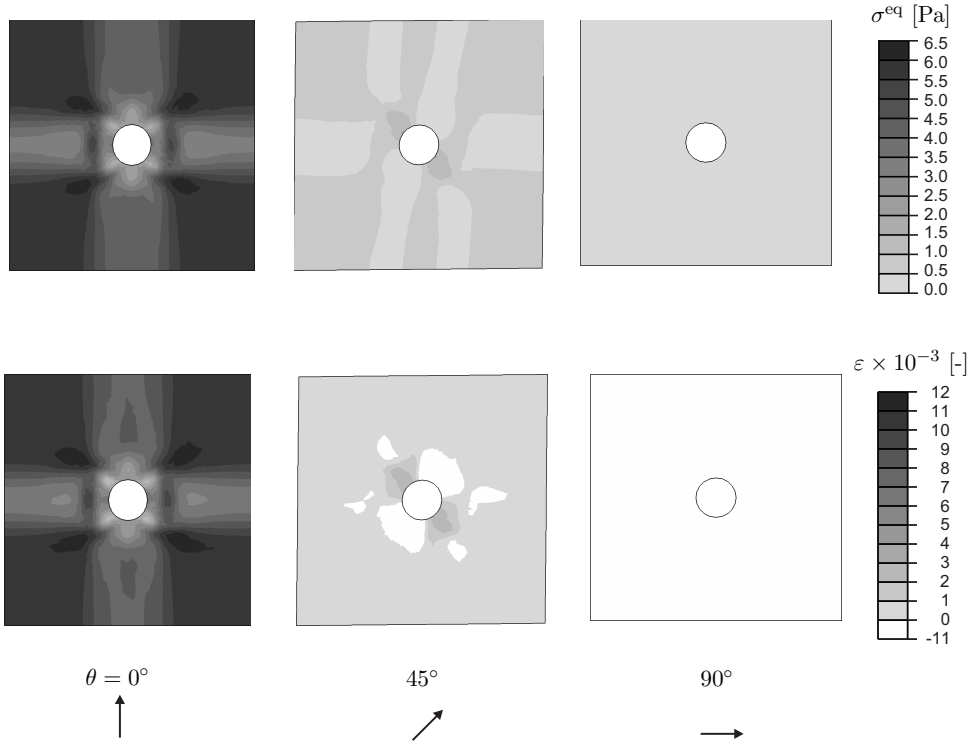

Figure 3.4: Equivalent stress (upper row) and axonal logarithmic strain (lower row) fields of the fiber-reinforced model with a maximum diversion angle of $\varphi = 45°$, and principal loading directions at an angle of $\theta = 0°$, 45°, and 90°. Note that the stress and strain in the inclusion is not shown in these field plots.

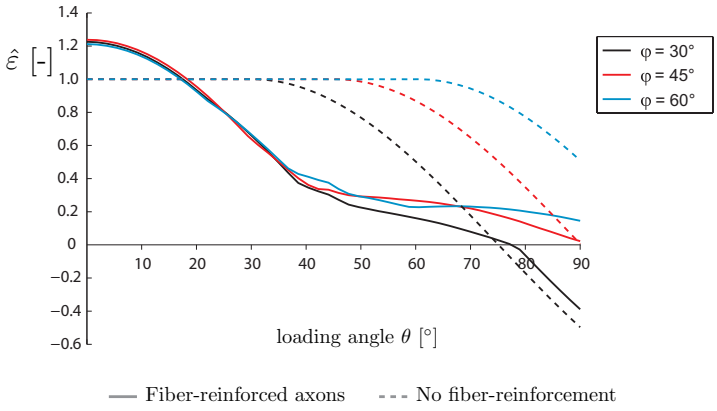

Figure 3.5: The maximum relative local axonal strain as a function of the principal loading angle θ for the oriented fibers with maximum diversion angles of $\varphi = 30°$, 45°, and 60°.

tions. The highest maximum axonal strain relative to the globally applied strain is about 1.2 for the fiber-reinforced case. This value is obtained when the tissue is loaded in the main axonal direction. Large axonal strains are found for a small range of loading angles. In case of no fiber-reinforcement, the local strain is never above the globally applied strain and the maximum relative strain decreases depending on the maximum diversion angle. The maximum relative strain is more dependent on the loading direction for lower maximum diversion angles.

The maximum axonal strain relative to the applied stress normalized by a reference value for homogeneous tissue is depicted in Figure 3.6 as a function of the loading angle for configurations with oriented fibers. Unoriented fiber configurations are not shown, because the normalized relative strain in these cases has a value of 1 over the entire range of loading directions. The results of the model without fiber-reinforced axon are the same as for the axonal strain relative to the tissue level strain. For loading angles above approximately $\theta = 45°$, this is also the case for results of simulations with the fiber-reinforced axons. At around a 45° loading angle, the fiber-reinforced tissue reaches a normalized maximum axonal strain relative to the applied stress that is 2.4, 2.5, and 2.8 times the value obtained at the loading direction in the main axonal direction (i.e., $\theta = 0°$) for φ =30°, 45°,

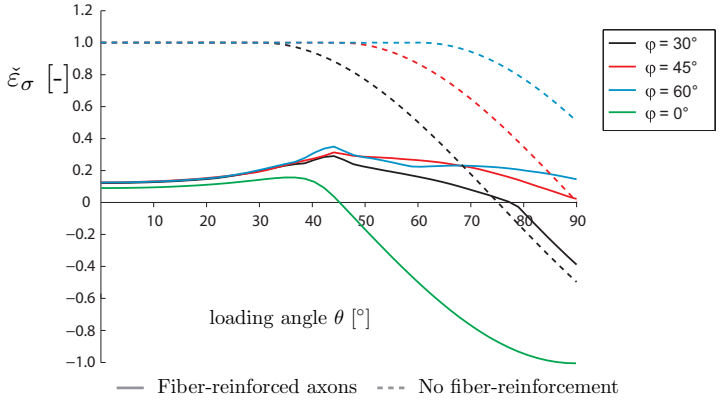

Figure 3.6: The maximum local axonal strain relative to the applied stress as a function of the principal loading angle θ for the oriented fibers with maximum diversion angles of $\varphi = 0°$, 30°, 45°, and 60°.

and 60°, respectively. For lower loading angles, the normalized maximum strains relative to the applied stress are lower than for the 45° loading angle, because of the stiffening effect of the fibers that are oriented closely towards the loading angle. For higher loading angles, however, the normalized maximum strain relative to the applied stress decreases, because it is affected by the decrease of the axonal strain relative the applied strain. The homogeneous oriented fiber configuration (i.e., $\varphi = 0°$) has a peak value at around $\theta = 36°$, which is 1.7 times the value obtained at $\theta = 0°$. For higher loading angles, the normalized maximum axonal strain relative to the applied stress drops to lower values more rapidly than the heterogeneous orientations (i.e., $\varphi = 30°$, 45°, 60°). Furthermore, it is observed that the peak values for the heterogeneous configurations are a factor of 1.8 to 2.2 with respect to the peak value reached for the homogeneous configuration. For the loading direction in the main axonal direction, the normalized maximum strain relative to the applied stress for the heterogeneous cases is increased by a factor 1.3 to 1.4 with respect to the homogeneous case.

In Figure 3.7, the strain in the axonal direction is displayed for the simulations with $\varphi = 45°$ at a 0° loading angle for two different values of the relative inclusion stiffnesses, which is defined as $\frac{G_{inclusion}}{G_{tissue}} = \frac{k_{1,inclusion}}{k_{1,tissue}}$. For all cases, it can be noticed that a higher relative inclusion stiffness

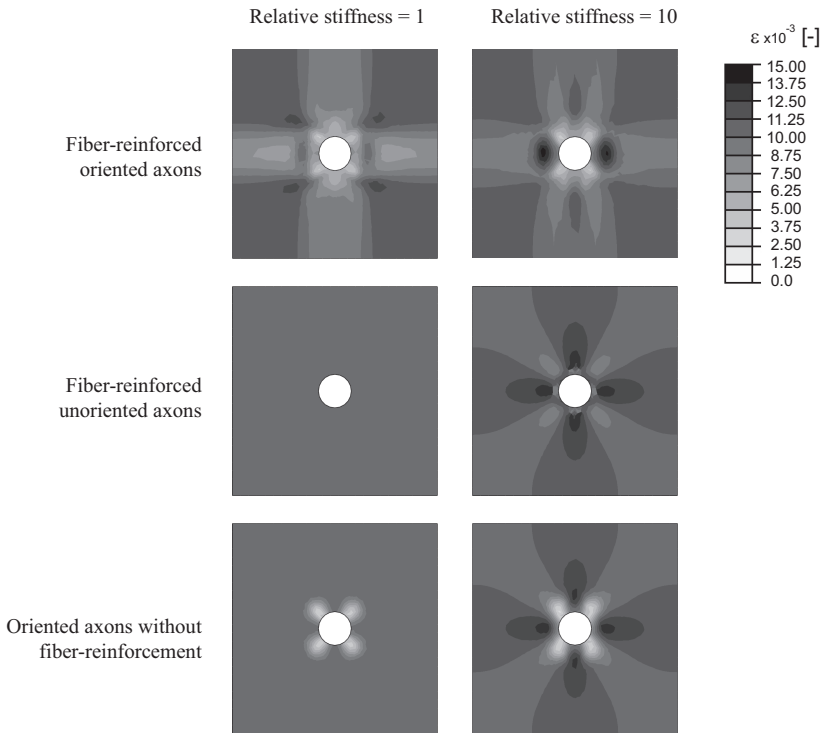

Figure 3.7: Strain in the axonal direction for the simulations with a loading angle $\theta = 0°$ and different relative stiffnesses of the inclusion. For the oriented configurations, a maximum diversion angle of 45° is used. Note that the strain in the inclusion is not shown in these field plots.

results in higher axonal strains. If only the subset of the three different configurations with a relative stiffness of 1 are compared to each other, it is observed that axonal alignment causes a heterogeneous strain field. Axonal alignment only leads to locally lower axonal strains, whereas alignment in combination with fiber-reinforcement causes locally higher axonal strains. In case the relative stiffness is 10, the axonal strain distribution is similar for both the fiber-reinforced unoriented axons and the oriented axons without fiber-reinforcement (i.e., the two situations with isotropic tissue behavior). Maximum values are located equatorial as well as polar to the inclusion.

However, the locations with lower axonal strain in the latter configuration are similar to those observed for the situation with a relative stiffness of 1. The configuration with fiber-reinforced oriented axons and an inclusion stiffness 10 times the surrounding tissue results in maximum values that are located equatorial to the inclusion only.

In order to investigate the influence of the stiffness of the inclusion on the axonal strain more carefully, the maximum relative axonal strain is plotted against the relative inclusion stiffness in Figure 3.8. For a high relative stiffness of the inclusion and fiber-reinforced oriented axons, the maximum axonal strain can exceed 1.7 times the global maximum principal tissue strain. This value is approximately 1.4 for the fiber-reinforced unoriented axons as well as for the oriented axons without fiber-reinforcement.

3.4 Discussion

From the results of all simulations, the most general observation is that the heterogeneities in the mechanical properties of brain tissue induce axonal strains higher than the applied tissue strain. The maximum local strains are all found near a stiff inclusion for axons aligned with the principal strain direction. The principal strain direction has an important influence on the results. For the fiber-reinforced oriented axons, the highest maximum axonal strains relative to the principal tissue strain are found at a 0° loading angle, which is the main axonal direction. However, the highest normalized maximum axonal strain relative to the principal tissue stress occurs at a loading angle of approximately 45° independently of the three different maximum diversion angles for the heterogeneous configurations. For the homogeneous case with fiber-reinforced oriented fibers, this occurs at about 36°. The reason the loading direction of the maximum axonal strain is shifted away from the main axonal direction, is the stiffening effect of the fibers in the main axonal direction. Nevertheless, this effect is counteracted by the decrease of the axonal strain relative to the applied tissue strain for higher loading angles. The heterogeneous fiber-reinforced cases result in higher normalized maximum axonal strains relative to the applied stress than for the homogeneous case. For a loading direction in the main axonal direction, this factor is between 1.3 and 1.4 and is caused by the

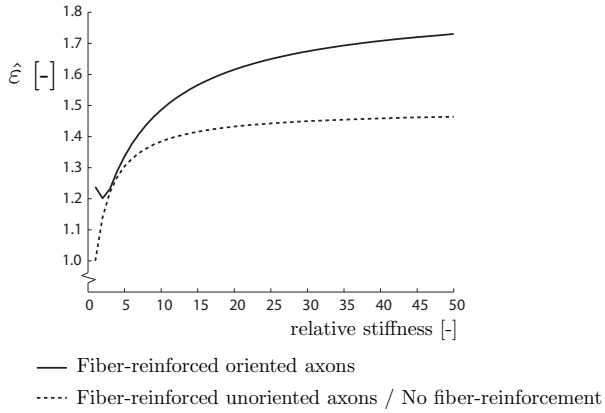

Figure 3.8: Axonal strain relative to the applied strain as a function of the stiffness of the inclusion with respect to the tissue stiffness for the simulations with a maximum diversion angle of $\varphi = 45°$ at a loading angle of $\theta = 0°$.

heterogeneous distribution of stiffnesses. For the peak values, the factor becomes 1.8 to 2.2. Here, also the fiber diversion angles have an influence on the normalized maximum axonal strain relative to the applied stress.

In this paper, it is assumed there is a relation between mechanical deformation and injury at an axonal level based on the observation by Povlishock [15] that mechanically induced DAI results in local axonal injury positioned where the axon changes its anatomical course. The results of the simulations show strain concentrations under similar circumstances, which is an indication that such a relationship might exist. Also, in experimental studies it was shown that a mechanical load imposed on axons causes physiological or functional impairments [59,60,137]. According to an experimental study conducted by LaPlaca et al. [138], axonal injury is dependent on the orientation of individual axons relative to the applied principal strain and axons are mostly sensitive to injury for stretch in the axial direction of the axon. This is in agreement with the orientation dependency of axonal injury with respect to the tissue strain that is observed in the current study.

For the development of a model that relates the mechanical aspects of TBI between the tissue level and the cellular level, several assumptions were

made, such as for the geometry and the mechanical properties at the cellular level. Despite the complexity of the real structures, a relatively simple model geometry was adopted in order to systematically compare different situations within the limits set by the limited information on the mechanical properties at the cellular level. Since no complex loading conditions are considered, it is assumed that the material behavior can be modeled completely elastic. Furthermore, the applied strain levels are chosen to be small and are well below values commonly associated with DAI. However, under the current assumption that no large non-linearities are present in the material behavior, the observed strain concentrations are almost independent of the strain level chosen. Relative quantities of predicted values are considered to be more important than absolute values making the conclusions drawn from this study partially independent of the chosen mechanical properties and loading conditions.

According to Lu and co-workers [83], the storage modulus of glial cell processes and pyramidal cell processes amounts to one-third of the modulus of their respective somata. However, this is measured by indenting the processes in a direction perpendicular to the axis of the process. For the material model used in the current study, the inclusion has a lower stiffness compared to an axon in the axonal direction, but it has a higher stiffness compared to an axon in the direction perpendicular to the axonal direction. In the latter case, this factor of one-third is reached for a logarithmic strain of about 0.5.

Since the model is plane strain, the inclusion has in fact a cylindrical shape, which could represent a blood vessel. However, the initially chosen material properties are based on the assumption that the inclusion is a soma, after which they were varied to investigate the effect of other types of inclusions (e.g., a blood vessel). A future study with three-dimensional models should elucidate the effects of different inclusion geometries with a three-dimensional nature.

In the current study, the effects of a possible undulation of the axons have not been accounted for. Although the mechanical effect of the undulation could be implemented by the non-linear constant k_2 at the tissue level, this would lead to a violation of length scales in the current model. It has been concluded by Bain et al. [87], that already at zero strain, parts of the axons are fully coupled to their surroundings, which causes them to

deform in an affine manner with respect to their surroundings. Although the axonal strain relative to the applied tissue stress is expected to become less dependent of the loading direction as a result of the undulation for small strains, it is expected to have no influence for larger strains at which DAI could occur and the axons are not undulated anymore.

3.5 Conclusion

In this study, the relation between mechanical loading of brain tissue and axonal stretching is investigated, providing a bridge between different length scales involved in TBI. Axonal strains resulting from a deformation at the tissue level can become higher than the applied tissue strain. Values of over 1.7 for the relative axonal strain are found in the simulations with a stiff inclusion. The maximum values are reached when the principal loading direction is aligned with the main axonal direction. For the loading conditions that represent a stress driven deformation, which is more representative for the mechanisms leading to TBI, axonal strains are shown to be influenced heavily by the fiber-reinforcement of the axons. The peak normalized maximum axonal strain relative to the applied stress is reached when the angle between the loading direction and the main axonal direction is 36° and about 45° for the homogeneous and heterogeneous configurations, respectively. The peak normalized maximum axonal strain relative to the applied stress is between 1.8 and 2.2 times higher for the heterogeneous cases than for the homogeneous case.

In the results of the simulations, the location of the peak strain is found close to or within the axons that deviate from the main axonal direction. Axonal injury has also been observed in a pathological study at locations where axons are forced to deviate [15]. Factors that influence the increase of the axonal strain relative to the applied tissue strain or stress are found to be: (i) the inclusion stiffness with respect to the surrounding tissue, (ii) the axonal orientation, (iii) the fiber-reinforcement (i.e, the effect of the neurofilaments, which are aligned with the long axis of the axon), and (iv) the maximum diversion angle of the axons. Factor (iii) and especially factor (iv) have an important influence mainly on the axonal strain relative to the applied stress.

The heterogeneities at the cellular level cause increased axonal strains that might lead to local injury of an axon as a result of the tissue level mechanical load and as a consequence, a strong orientation dependent sensitivity of axonal stretching to tissue level deformations is found. Therefore, FE head models should account for the effects of the mechanical heterogeneities at the cellular level and this orientation dependent sensitivity to predict more accurately DAI by means of anisotropic and microstructure-related injury criteria. Even though the current study indicates the importance of the cellular level with respect to TBI, more research is needed to properly quantify such injury criteria. Because it is not realistic to develop an FE head model with a resolution typical for the axonal length scale, a proper way to achieve this, is the integration of a detailed micromechanical model in a macroscopic head model using a multiple scale approach, in which FE models representing different discrete length scales of the same material are coupled. It is expected that this will result in more realistic deformation modes and hence also more realistic cellular level injury predictions. This will be the subject of future work. Depending on the outcome of that work, cellular level injury might be generalized to specific tissue level loads. In that case, ultimately, macroscopic head model simulations can account for the cellular level effects by merely applying these injury criteria. However, if this generalization is not possible, a multiple scale approach might still be necessary to predict brain injury caused by a mechanical load.

Chapter four

4

Anisotropic Brain Injury Criterion

Different length scales from micrometers to several decimeters play an important role in diffuse axonal injury. The kinematics at the head level result in local impairments at the cellular level. Finite element methods can be used for predicting brain injury caused by a mechanical loading of the head. Because of its oriented microstructure, the sensitivity of brain tissue to a mechanical load can be expected to be orientation-dependent. However, criteria for injury that are currently used at the tissue level in finite element head models are isotropic and therefore do not consider this orientation dependence, which might inhibit a reliable assessment of injury. In this study, an anisotropic brain injury criterion is developed that is able to describe the effects of the oriented microstructure based on micromechanical simulations. Both the effects of the main axonal direction and of local deviations from this direction are accounted for. With the anisotropic criterion for brain injury, computational head models will be able to account for aspects of diffuse axonal injury at the cellular level and can therefore more reliably predict injury.

Reproduced from: R.J.H. Cloots, J.A.W. van Dommelen and M.G.D. Geers (2011). A tissue-level anisotropic criterion for brain injury based on microstructural axonal deformation. *Journal of the Mechanical Behavior of Biomedical Materials*, (in press).

4.1 Introduction

Traumatic brain injury (TBI) can be caused by a mechanical action on the head, for instance as a result of a sports or road traffic accident. More than 1.5 million cases were reported in the United States in 2003 [139]. One of the most frequently occurring types of TBI is Diffuse Axonal Injury (DAI) [140]. For an improvement of the prevention or diagnosis of TBI, it is necessary to better understand the relation between the mechanical insult on the head and the resulting injury. Brain injury criteria are used to assess an injury level resulting from mechanical loading. The brain injury criterion most commonly used nowadays is the Head Injury Criterion (HIC) [32]. However, it has a number of drawbacks, among which the fact that it is based on the translational accelerations of the head only. Although injury occurs as a result of a mechanical load on the head, the actual injury happens at the cellular level within the brain [94,141]. Therefore, more sophisticated brain injury criteria that take this cellular level into account may be able to better predict brain injury.

More detailed mechanical effects can be included in the relation between a mechanical load and the resulting brain injury by using computational models. Three-dimensional finite element (FE) models of the head and brain have been developed to describe brain tissue strains and stresses caused by a mechanical insult (e.g., [36–38,64,97]). The outcome of these head models can be interpreted by means of tissue-level injury criteria that can be obtained from experiments in which mechanically deformed brain tissue is related to cell damage or electrophysiological impairments of the neurons (e.g., [59–62,78,138,142–144]). Some of the tissue-level criteria are based on strains, strain rates or the product of strain and strain rate, but it is difficult to obtain a threshold for injury for any of the currently used injury criteria. Besides numerical head modeling for injury prediction, also several modeling studies have focused on the relation between the tissue-level mechanical behavior and the cellular-level structures [88,126–128]. In Chapter 3, the FE method was used to investigate the cellular-level effect of brain injury. Even though research on TBI is being conducted at different length scales, current numerical head models do not include the effects of the cellular structure.

To understand how the global head load and cellular injury are connected,

it is important to make a distinction between the different length scales that play a role (see Figure 4.1). The mechanical load on the head results in a head acceleration, which causes tissue stress and strain concentrations due to the geometrical heterogeneities at the tissue level. This again leads to cellular level stress and strain concentrations, which are affected by the cellular microstructure. At the latter length scale, individual cells can be distinguished. Neurons and glial cells consist of a cell body from which processes extend [21,22]. The typical diameter of these cell bodies is about 5 μm for glial cells, whereas for neurons it is less than 10 μm or up to 20 μm for non-pyramidal neurons and other cortical and hippocampal neurons, respectively [67–72]. Most neuronal cell bodies are in the cortex, but their axons can be many centimeters long with a uniform diameter extending into the other parts of the brain, whereas dendrites taper away from the soma and rarely exceed 500 μm in length [73]. The vast majority of brain tissue consists of axons and even in the cerebral cortex, which is relatively rich in cell bodies and blood vessels in comparison with other parts of the brain, 60% to 70% of the volume consists of neuronal axons and dendrites, 5% to 10% of glial processes, 10% to 20% of cell bodies and blood vessels, and the remaining part is extracellular space [120–123].

An important aspect of DAI is that it is associated with discrete local impairments of axons at locations where these have to deviate because of the presence of an inclusion (e.g., a blood vessel or a soma) [124,125,141]. It has been shown in Chapter 3 that there might be a mechanical cause

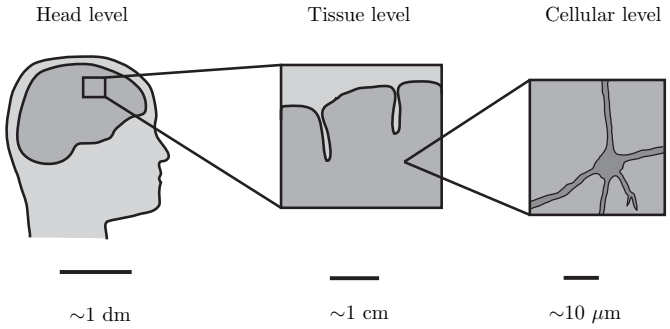

Figure 4.1: The length scales involved with TBI ranging from decimeters at the head level to micrometers at the cellular level.

for this, as concentrations of axonal stretch can occur more easily there, depending on the local material properties, axonal orientations and loading directions. From experiments with tissue deformations, the results indicate that axons are mostly sensitive to injury for stretch in the axial direction of the axon [138]. This could indicate that the micromechanics at an axonal level should be accounted for in head level FE simulations. However, the typical resolution of existing head models is much larger than the axonal length scale, which means that these micromechanical effects cannot be incorporated in the numerical head model in a conventional manner. To overcome this problem, a multi-scale approach can be adopted, in which two computational models of different length scales are coupled (e.g., [109] or Chapter 5). However, drawbacks of this approach are the complexity of modeling as well as the high computational demands, since for each integration point of the head model for which the micromechanical effects need to be accounted for, a micromechanical problem must be solved. For practical applications, FE head models should be able to predict axonal injury based on axonal orientation without the need for a nested multi-scale coupling. Therefore, the aim of this study is to develop an anisotropic injury criterion that accounts for the micromechanical effects that are important for DAI and that can be directly applied at the tissue level of a numerical head model.

4.2 Methods

In this study, a critical volume element (CVE) is modeled that represents a critical region of the brain tissue for axonal injury at the micrometer length scale. As opposed to a representative volume element, which represents a microstructure that is continuously repeated throughout the material and thereby describes the macroscopic material behavior, the CVE represents only regions that are relatively sparsely present in the microstructure and thereby the mechanical heterogeneities of the CVE do not influence the macroscopic material behavior. Two different configurations of a CVE are developed that can predict the strain concentrations at an axonal level caused by a deformation that is applied at the level of the homogenized tissue. One configuration represents a geometry with a cell body as an inclusion and the other configuration represents a geometry with a blood

vessel as an inclusion. Within those CVEs, the mechanical response of the tissue anisotropically depends on local axonal orientations. Furthermore, an anisotropic brain injury criterion is developed that can capture the concentrated axonal stretch within the CVE, which is considered to be critical for brain injury, as a function of the applied homogenized tissue strain.

4.2.1 Critical volume element

In Chapter 3, a CVE was developed that describes DAI at an axonal level. It was modeled with a plane strain assumption and was based on the pathological observation of discrete local impairments of axons near an obstruction, such as a blood vessel or soma [141]. For the model in Chapter 3, it was assumed that this typical critical geometry may be one of the causes for injury due to mechanical strain concentrations in the axons surrounding the obstruction. Furthermore, it was assumed that axonal injury is caused by axial stretching of the axon. In the current study, based on the same assumptions, the CVE is extended to a three-dimensional model of two different geometries. Both models represent a small volume of brain tissue with dimensions 50x50x50 μm^3 containing a critical configuration of axons that curve around an inclusion. The material containing the axons is modeled as a continuum and the interface with the inclusion is assumed to be perfectly tied. In one of the geometries, the inclusion is a sphere of diameter 8 μm, which represents a soma, whereas the second geometry contains a cylindrical inclusion of diameter 8 μm representing a blood vessel (see Figure 4.2). The CVEs with the spherical and the cylindrical inclusion are modeled with the FE code Abaqus 6.10 [145] and consist in total of 28216 and 27960 linear hexahedral reduced integration elements with hourglass control, respectively. Inside the CVE, the majority of the axons is orientated in the $\vec{e}_y$ direction, which is considered here as the main axonal direction. Near the inclusion, however, the axonal orientation is locally deviating from the main axonal direction. For this study, it is assumed that the axonal orientation pattern can be described by a gradient which is partially obstructed by the presence of an inclusion. Therefore, the local axonal orientation is obtained by means of a classical diffusion problem simulation, in which a concentration difference is imposed on the top and bottom faces of the model. For all other faces, as well as for the

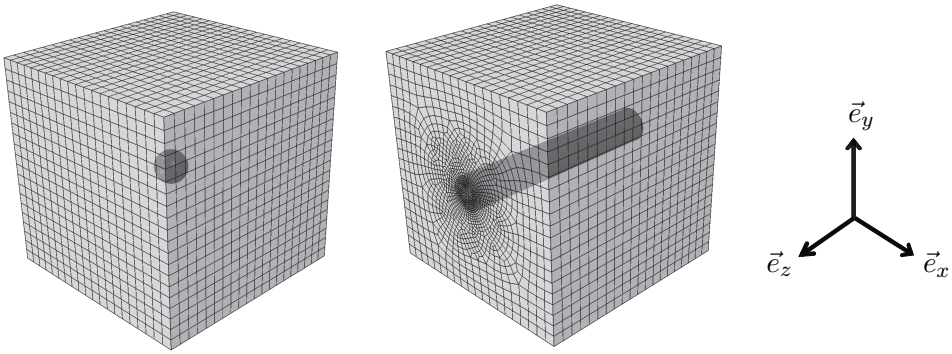

(a) (b)

Figure 4.2: The geometries and the spatial discretization of the CVEs with (a) a spherical inclusion and (b) a cylindrical inclusion.

interface with the inclusion a zero flow rate across the boundary is modeled (see Figure 4.3). With this method, for the model with the cylindrical inclusion, the main axonal orientation is perpendicular to the long axis of the inclusion. To investigate also other configurations for the CVE with the cylindrical inclusion, different orientation fields are generated where the main axonal direction varies with an angle β from 0° to 90° with respect to the orientation of the long axis of the cylindrical inclusion. This is realized by giving the local vector base $\{\vec{e}_1, \vec{e}_2, \vec{e}_3\}$, in which the axonal orientation is aligned with vector $\vec{e}_2$, at each integration point an additional rotation about vector $\vec{e}_1$, where before rotation $\vec{e}_3 = \vec{e}_z$.

Inside each axon, fibers (i.e., neurofilaments) are aligned in the direction of the axon itself and provide the axon its mechanical strength [73]. The mechanical behavior of the local material consisting of oriented axons is described by a fiber-reinforced material model, of which the strain energy potential is [145]:

$$W = \frac{G}{2}(\tilde{I}_1 - 3) + K\left(\frac{J^2-1}{4} - \frac{1}{2}\ln J\right) + \frac{k_1}{2k_2}\sum_{\alpha=1}^{N}\left(e^{k_2\langle\tilde{E}_\alpha\rangle^2} - 1\right), \quad (4.1)$$

where the third term on the right hand side is the Holzapfel-Gasser-Ogden

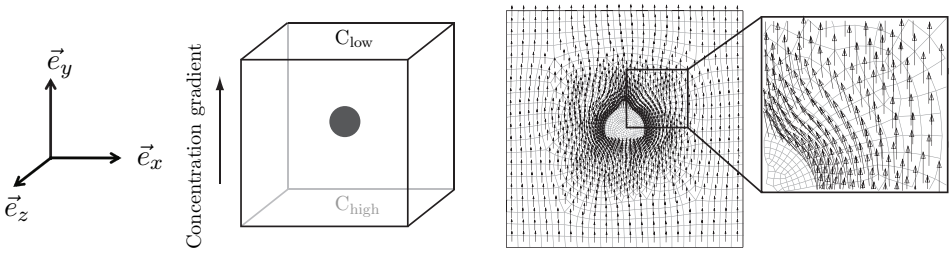

(a) (b)

Figure 4.3: (a) A diffusion problem simulation is used to obtain the axonal orientation for both CVEs. (b) Resulting vector field of the concentration gradient that is used as the axonal orientation.

form [132] with

$$\tilde{E}_\alpha = \kappa(\tilde{I}_1 - 3) + (1 - 3\kappa)(\tilde{I}_{4\alpha} - 1), \tag{4.2}$$

where G is the shear modulus, K is the bulk modulus, $J = \det(\boldsymbol{F})$ is the volume change ratio, k_1 and k_2 describe the fiber stiffness, $\tilde{I}_1$ is the first invariant of the isochoric part of the right Cauchy-Green deformation tensor $\tilde{\boldsymbol{C}} = J^{-\frac{2}{3}}\boldsymbol{C}$, $\tilde{I}_{4\alpha} = \tilde{\boldsymbol{C}} : \vec{n}_{0\alpha}\vec{n}_{0\alpha}$ where $\vec{n}_{0\alpha}$ is the fiber family direction vector in the reference configuration with unit length and N is the total number of fiber families. The material parameter κ describes the dispersion of the fiber orientations around the preferred fiber direction $\vec{n}_{0\alpha}$. The two limits of κ are 0 for fully aligned fibers (i.e., transverse isotropy) and $\frac{1}{3}$ for randomly orientated fibers (i.e., isotropy). Therefore, the value of κ is related to the degree of anisotropy. By means of the Macaulay brackets $\langle\cdot\rangle$, the fibers contribute only in tension and not in compression, as $\langle\tilde{E}\rangle$ becomes 0 if $\tilde{E}$ is negative.

The material properties of the axonal tissue are obtained from the study by Ning et al. [58], which is based on the mechanical tissue behavior of the brainstem and are $G = 12.7$ Pa, $k_1 = 121.2$ Pa and $\kappa = 0$. Furthermore, only one fiber family is assumed (i.e., $N = 1$) and the fiber contribution to the stiffness is assumed linear (i.e., $k_2 \to 0$). Then, the third term on the right hand side of Equation 4.1 becomes $W_{\text{fiber}} = \frac{k_1}{2}\langle\tilde{E}_1\rangle^2$. Because in the current study, it is assumed that mechanical anisotropy is caused by the

neurofilaments, which are of a much smaller dimension than the axons, the tissue-level parameters obtained by Ning and co-workers are used in the current study for the axonal material model. In Chapter 3, it was assumed that a cell body mechanically behaves the same as the surrounding axonal tissue, except that $\kappa = \frac{1}{3}$, referring to randomly oriented neurofilaments within the cell body. Blood vessels may have different mechanical properties, which affects the axonal strains, which is discussed in Chapter 3, but for a more in-depth investigation of the effect of the geometry the same inclusion stiffness will be used for both CVEs. The bulk modulus K is assumed to be constant over the whole volume. The parameter values are shown in Table 4.1.

Table 4.1: Material properties obtained from Chapter 3 and [58].

	G (Pa)	k_1 (Pa)	κ	K (GPa)
Axonal tissue	12.7	121.2	0	2.5
Inclusion	12.7	121.2	$\frac{1}{3}$	2.5

For the application of the mechanical loading, periodic boundary conditions are used [109]. The displacement vectors $\vec{u}$ of corner nodes c_1, c_2, c_4 and c_5, as shown in Figure 4.4, are calculated from the global deformation gradient tensor $\bar{\boldsymbol{F}}$, which equals the homogenized deformation of the CVE:

$$\vec{u}_{c_i} = (\bar{\boldsymbol{F}} - \boldsymbol{I}) \cdot \vec{x}_{c_{0i}}, \tag{4.3}$$

in which $\vec{x}_0$ is the initial position vector and $\boldsymbol{I}$ is the unit tensor. The nodal displacement vectors of the remaining parts of the boundary are tied as follows:

$$\vec{u}_{\Gamma_{5678}} - \vec{u}_{\Gamma_{1234}} = \vec{u}_{c_5} - \vec{u}_{c_1} \tag{4.4}$$

$$\vec{u}_{\Gamma_{2673}} - \vec{u}_{\Gamma_{1584}} = \vec{u}_{c_2} - \vec{u}_{c_1} \tag{4.5}$$

$$\vec{u}_{\Gamma_{4378}} - \vec{u}_{\Gamma_{1265}} = \vec{u}_{c_4} - \vec{u}_{c_1}, \tag{4.6}$$

where Γ_{jklm} denotes the faces of the model. As a result of these periodic kinematical boundary conditions, antiperiodicity of the tractions is satisfied

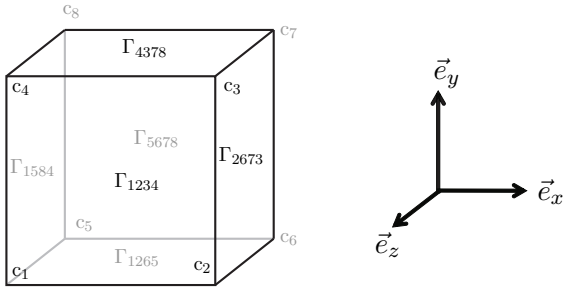

Figure 4.4: Labeling of the corners and faces of the CVE for the periodic boundary conditions.

as well [109].

Two types of loading conditions are used that both lead to isochoric deformations, because it is assumed that under impact conditions, deviatoric strains are highly dominating over volumetric strains due to the near incompressibility of brain tissue. The first loading condition is isochoric uniaxial stretching that is described by the deformation gradient tensor

$$\bar{\boldsymbol{F}} = \bar{\lambda}^{-\frac{1}{2}}\vec{m}_1\vec{m}_1 + \bar{\lambda}\vec{m}_2\vec{m}_2 + \bar{\lambda}^{-\frac{1}{2}}\vec{m}_3\vec{m}_3, \tag{4.7}$$

with $\bar{\lambda} = 1.001$, 1.01 or 1.1 the global stretch and the unit vectors $\vec{m}_i$ defining an orthogonal vector basis with $\vec{m}_2$ corresponding to the uniaxial loading direction. Then, the logarithmic strain tensor becomes

$$\bar{\boldsymbol{\varepsilon}} = \bar{\varepsilon}\left(-\frac{1}{2}\vec{m}_1\vec{m}_1 + \vec{m}_2\vec{m}_2 - \frac{1}{2}\vec{m}_3\vec{m}_3\right), \tag{4.8}$$

where $\bar{\varepsilon} = \ln(\bar{\lambda})$ is the maximum principal tissue strain. The vector basis $\{\vec{m}_1, \vec{m}_2, \vec{m}_3\}$ is defined with respect to the global Cartesian vector basis $\{\vec{e}_x, \vec{e}_y, \vec{e}_z\}$ according to

$$\vec{m}_1 = \cos\phi\cos\theta\vec{e}_x - \sin\phi\vec{e}_y + \cos\phi\sin\theta\vec{e}_z \tag{4.9}$$

$$\vec{m}_2 = \sin\phi\cos\theta\vec{e}_x + \cos\phi\vec{e}_y + \sin\phi\sin\theta\vec{e}_z \tag{4.10}$$

$$\vec{m}_3 = -\sin\theta\vec{e}_x + \cos\theta\vec{e}_z, \tag{4.11}$$

in which ϕ is the angle between $\vec{m}_2$ and $\vec{e}_y$ and θ is the rotation angle about $\vec{e}_y$ (see Figure 4.5). The angles θ and ϕ define the direction of loading with respect to the principal directions of the CVE and are varied over the entire space of orientations. Besides an isochoric uniaxial deformation, an isochoric biaxial stretching is also applied, which is described by the deformation gradient tensor

$$\bar{\boldsymbol{F}} = \bar{\lambda}\vec{m}_1\vec{m}_1 + \bar{\lambda}^{-2}\vec{m}_2\vec{m}_2 + \bar{\lambda}\vec{m}_3\vec{m}_3. \tag{4.12}$$

In addition to this CVE analysis, a homogeneous case is also considered, in which no inclusion is present. This configuration is modeled analytically as follows:

$$\varepsilon_{\mathrm{ax}}(\theta,\phi) = \frac{1}{2}\langle \ln(\boldsymbol{C}(\theta,\phi) : \vec{n}_0\vec{n}_0)\rangle, \tag{4.13}$$

where $\varepsilon_{\mathrm{ax}} = \langle \ln\lambda_{\mathrm{ax}}\rangle$ is the strain in the axial direction of the axon. This case is independent of the material behavior and depends only on the deformation and the main axonal direction.

To analyze the axonal strain with respect to the global maximum principal

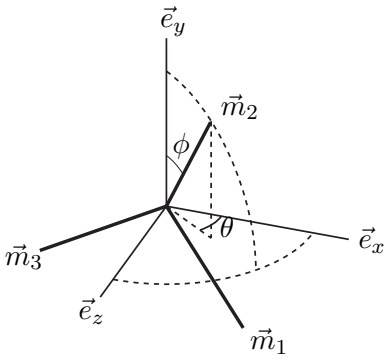

Figure 4.5: A rotated vector basis $\{\vec{m}_1,\ \vec{m}_2,\ \vec{m}_3\}$ that defines the main loading directions with respect to the global vector basis $\{\vec{e}_x,\ \vec{e}_y,\ \vec{e}_z\}$ according to the angles ϕ and θ.

tissue strain $\bar{\varepsilon}$, a relative axonal strain is defined as

$$\hat{\varepsilon}(\phi,\theta) = \frac{\varepsilon_{\mathrm{ax}}(\phi,\theta)}{\bar{\varepsilon}}, \tag{4.14}$$

where the relative axonal strain $\hat{\varepsilon}$ is a local quantity that varies throughout the CVE. For the maximum relative axonal strain, the most critical value within the CVE is used:

$$\hat{\varepsilon}_{\max}(\phi,\theta) = \max_{\mathrm{CVE}}\left\{\hat{\varepsilon}(\phi,\theta)\right\}. \tag{4.15}$$

4.2.2 Anisotropic equivalent strain measure

The most critical value of the relative axonal strain within the CVE, as stated in Equation 4.15, depends on the loading direction and the loading magnitude at the tissue level. This means that the maximum axonal strain in the CVE can be expressed as a function of the tissue strain tensor and therefore, an anisotropic equivalent strain measure is developed:

$$\begin{aligned} \bar{\varepsilon}^{\mathrm{eq}} &= \max_{\mathrm{CVE}}\left\{\varepsilon_{\mathrm{ax}}(\phi,\theta)\right\}, && (4.16)\\ &= f(\bar{\boldsymbol{\varepsilon}}), && (4.17) \end{aligned}$$

which gives the maximum axonal strain value as a function f of the tissue strain tensor $\bar{\boldsymbol{\varepsilon}}$. To achieve this, an equivalent tissue strain based on the Liu-Huang-Stout yield criterion [146], which is a combination of the Hill [147] and Drucker-Prager [148] yield criteria (originally formulated in terms of stress), is introduced:

$$\begin{aligned} \bar{\varepsilon}^{\mathrm{eq}} = \big[&F(\bar{\varepsilon}_{yy}-\bar{\varepsilon}_{zz})^2 + G(\bar{\varepsilon}_{zz}-\bar{\varepsilon}_{xx})^2 + H(\bar{\varepsilon}_{xx}-\bar{\varepsilon}_{yy})^2 \\ &+2L\bar{\varepsilon}_{yz}^2 + 2M\bar{\varepsilon}_{zx}^2 + 2N\bar{\varepsilon}_{xy}^2\big]^{\frac{1}{2}} + I\bar{\varepsilon}_{xx}^d + J\bar{\varepsilon}_{yy}^d + K\bar{\varepsilon}_{zz}^d, \end{aligned} \tag{4.18}$$

where $\bar{\varepsilon}_{ij}$ are the tissue strain components in a Cartesian vector basis $\{\vec{e}_x, \vec{e}_y, \vec{e}_z\}$ and the superscript d denotes the deviatoric part, defined as $(\cdot)^d = (\cdot) - \frac{1}{3}\mathrm{trace}(\cdot)\boldsymbol{I}$. The coefficients I, J and K referring to the linear terms are used to describe the difference in the yield strain between uniaxial tension and compression. In the current study, a uniaxial and a biaxial

deformation are used to determine the coefficients, which is comparable to tension/compression since all deformations are isochoric. In contrast to the original Liu-Huang-Stout criterion, the deviatoric part is used for the linear terms, since only isochoric cases are tested in this study and for volumetric loading, if critical, other quantities (e.g., pressure) than axonal stretching are expected to be important due to the near incompressibility of brain tissue. As a consequence, only two of the parameters I, J and K can be determined independently and therefore, they are replaced by the two (arbitrarily chosen) coefficients $A = I - K$ and $B = J - K$, which yields $I\bar{\varepsilon}^d_{xx} + J\bar{\varepsilon}^d_{yy} + K\bar{\varepsilon}^d_{zz} = A\bar{\varepsilon}^d_{xx} + B\bar{\varepsilon}^d_{yy}$. The parameters of Equation 4.18 will be determined such that the equivalent strain values are the same as the maximum axonal strains obtained from the CVE simulations. The equivalent strain can be applied to any arbitrary loading condition. To apply the deformation gradient tensor of Equation 4.7 or 4.12, the right hand side of Equation 4.18 relative to the maximum principal tissue strain $\bar{\varepsilon}$ is denoted $g(\phi, \theta)$, allowing to rewrite Equation 4.18 as

$$\bar{\varepsilon}^{\mathrm{eq}} = \bar{\varepsilon} g(\phi, \theta). \tag{4.19}$$

By using Equations 4.14 to 4.19, it follows that the orientation dependence of the equivalent strain is given by the maximum relative axonal strain, i.e., $g(\phi, \theta) = \hat{\varepsilon}_{\max}(\phi, \theta)$, from which the coefficients of Equation 4.18 can be determined, if the dependence of $\hat{\varepsilon}_{\max}$ on the direction of loading is characterized. In case of isochoric uniaxial deformation (Equation 4.7), function g can be expressed, using Equations 4.8 to 4.11, as

$$\begin{aligned} g_{\mathrm{uni}}(\phi, \theta) = \frac{3}{2} \Big[& F \left(\cos^2\phi - \sin^2\phi \sin^2\theta \right)^2 + G \left(\sin^2\phi \sin^2\theta - \sin^2\phi \cos^2\theta \right)^2 \\ & + H \left(\cos^2\phi - \sin^2\phi \cos^2\theta \right)^2 + 6L \sin^2\phi \cos^2\phi \sin^2\theta \\ & + 6M \sin^4\phi \sin^2\theta \cos^2\theta + 6N \sin^2\phi \cos^2\phi \cos^2\theta \Big]^{\frac{1}{2}} \\ & + \frac{1}{2} A (3\sin^2\phi \cos^2\theta - 1) + \frac{1}{2} B (3\cos^2\phi - 1). \end{aligned} \tag{4.20}$$

For the isochoric biaxial deformation as defined in Equation 4.12, function g can be written as

$$\begin{aligned} g_{\mathrm{bi}}(\phi,\theta) = 3\big[&F(\cos^2\phi - \sin^2\phi\sin^2\theta)^2 + G(\sin^2\phi\sin^2\theta - \sin^2\phi\cos^2\theta)^2 \\ &+ H(\cos^2\phi - \sin^2\phi\cos^2\theta)^2 + 6L\sin^2\phi\cos^2\phi\sin^2\theta \\ &+ 6M\sin^4\phi\sin^2\theta\cos^2\theta + 6N\sin^2\phi\cos^2\phi\cos^2\theta\big]^{\frac{1}{2}} \\ &- A(3\sin^2\phi\cos^2\theta - 1) - B(3\cos^2\phi - 1). \end{aligned} \tag{4.21}$$

The coefficients F, G, H, A and B can then be derived from Equations 4.20 and 4.21 for ϕ and θ equal to 0° or 90°, by solving a subset of five of the following six equations where the value of g is obtained from the CVE simulations:

$$g_{\mathrm{uni}}(0,\theta) = \frac{3}{2}(F+H)^{\frac{1}{2}} - \frac{A}{2} + B \tag{4.22}$$

$$g_{\mathrm{uni}}(90,0) = \frac{3}{2}(G+H)^{\frac{1}{2}} + A - \frac{B}{2} \tag{4.23}$$

$$g_{\mathrm{uni}}(90,90) = \frac{3}{2}(F+G)^{\frac{1}{2}} - \frac{A}{2} - \frac{B}{2} \tag{4.24}$$

$$g_{\mathrm{bi}}(0,\theta) = 3(F+H)^{\frac{1}{2}} + A - 2B \tag{4.25}$$

$$g_{\mathrm{bi}}(90,0) = 3(G+H)^{\frac{1}{2}} - 2A + B \tag{4.26}$$

$$g_{\mathrm{bi}}(90,90) = 3(F+G)^{\frac{1}{2}} + A + B. \tag{4.27}$$

The subset will be chosen such that the highest maximum relative axonal strain values are best captured by the anisotropic equivalent function. The coefficients L, M and N, which characterize the influence of the shear strains, are identified from a least squares fit of the equivalent strain values for intermediate angles of ϕ and θ between 0° or 90° to the results of the simulations for uniaxial deformations. Subsequently, the obtained coefficients are validated for biaxial deformations. The coefficients F, G, H, L, M and N have to satisfy certain constraints, since the part corresponding to the square root of Equation 4.18 should be positive semi-definite [149]. Therefore, the following conditions are required: $N \geqslant 0$, $M \geqslant 0$, $L \geqslant 0$ and $FG + FH + GH \geqslant 0$.

In the homogeneous case or in the case of the CVE that contains a spherical inclusion, both with the main axonal orientation in the $\vec{e}_y$-direction, the geometry causes the axonal strain behavior to be transversely isotropic. Due to this, the number of independent coefficients decreases according to: $F = H$, $M = H + 2G$, $L = N$ and $A = 0$.

Unlike in plasticity, for which the Liu-Huang-Stout criterion is used to describe the onset of plastic deformation, the equivalent strain measure represents the magnitude of axonal stretching. Thereby, the equivalent strain measure can be used as an anisotropic brain injury criterion. If $\varepsilon_{\mathrm{ax,c}}$ is a constant value that represents a critical axonal strain for injury, then at the onset of injury:

$$\max_{\mathrm{CVE}} \{\varepsilon_{\mathrm{ax}}(\phi, \theta)\} = \varepsilon_{\mathrm{ax,c}}, \tag{4.28}$$

from which Equation 4.19 can be rewritten as a criterion for injury:

$$\begin{aligned} \bar{\varepsilon}_{\mathrm{c}}^{\mathrm{eq}} &= \bar{\varepsilon}_{\mathrm{c}}(\phi, \theta) g(\phi, \theta), & (4.29) \\ &= \varepsilon_{\mathrm{ax,c}}, & (4.30) \end{aligned}$$

where $\bar{\varepsilon}_c$ is the critical tissue strain for axonal injury, which depends on the loading direction.

4.3 Results

In this section, the microstructural effects on the concentration of axonal strain as observed in the simulations with the CVEs are shown, as well as the ability of the proposed anisotropic equivalent strain measure to capture these effects. Unless otherwise stated, the global stretch $\bar{\lambda}$ is always 1.001 for the shown results.

In Figure 4.6, the maximum relative axonal strain is depicted as a function of the loading angle for the homogeneous case (i.e., without inclusions). The results of the analytical solution can be described perfectly by the anisotropic equivalent strain over the entire range of loading directions for both the uniaxial and the biaxial deformation modes. The axonal strain is

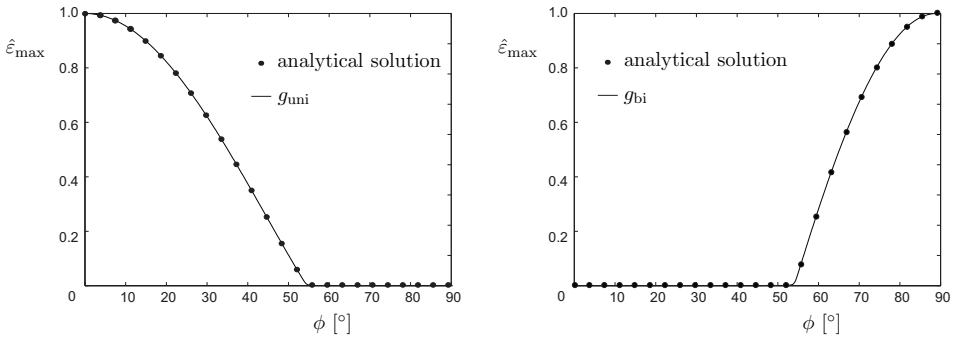

Figure 4.6: The maximum relative axonal strain versus the loading angle ϕ for (a) uniaxial and (b) biaxial deformations of homogeneous tissue with uniaxially oriented axons. In both plots, the line represents function g (Equations 4.20 and 4.21 for (a) and (b), repectively) and the dots refer to the maximum relative axonal strain obtained from the analytical solution for a homogeneous case.

equal to the applied tissue strain for the loading angle that corresponds to a tensile strain in the main axonal direction. For loading angles that cause only compressive strains in the main axonal direction, the relative strain is zero. The values of the coefficients in the anisotropic equivalent strain measure are summarized in Table 4.2, from which it can be noticed that all shear coefficients are zero for an exact fit of the homogeneous configuration.

Figure 4.7 displays the equivalent stress $\sigma^{\text{eq}} = \sqrt{\frac{3}{2}\boldsymbol{\sigma}^d : \boldsymbol{\sigma}^d}$ and the relative axonal strain $\hat{\varepsilon}$ for the CVE with a spherical inclusion and $\phi = 0°$ (i.e., the loading direction and the main axonal orientation are the same). It is clear that both field plots are alike and the highest concentrations occur equatorial to the inclusion. These results indicate that the equivalent stress distribution is influenced by the local heterogeneities (i.e., stiffness and orientation) in the same manner as the axonal strain distribution.

The relative strains that are obtained from the simulations with the CVE containing a spherical inclusion are plotted in Figure 4.8. It can be noticed that the overall dependency of the relative strain on the loading angle is

Table 4.2: The values of the coefficients of Equation 4.18 obtained for the simulations without an inclusion, with a spherical inclusion and with a cylindrical inclusion. The solution for the homogeneous case is exact.

	Inclusion		
Coefficient	None	Spherical	Cylindrical
F	1/18	0.163	0.081
G	-1/36	-0.056	-0.015
H	1/18	0.163	0.089
L	0	0.119	0.000
M	0	0.051	0.010
N	0	0.119	0.090
A	0	0.000	0.145
B	1/2	0.707	0.625

similar to the homogeneous case. However, the magnitude of the relative strains is higher and nearly reaches 1.6, which means that the maximum local axonal strain is considerably larger than the applied tissue strain. This is a consequence of the local variation in axonal orientation around

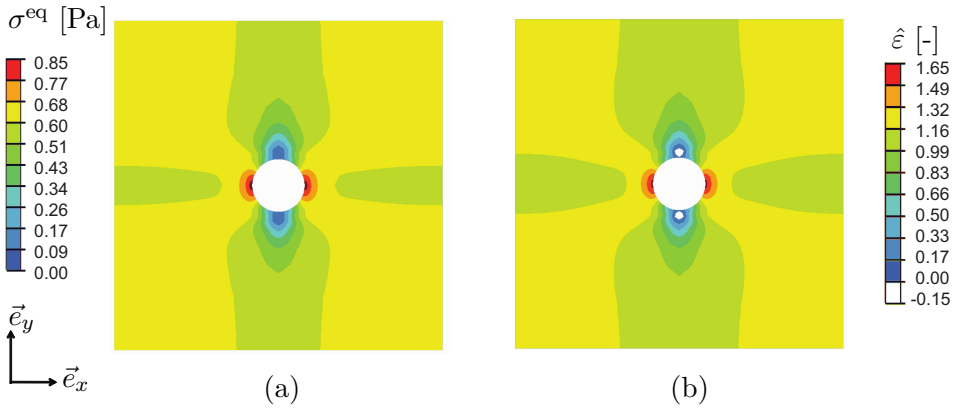

Figure 4.7: (a) Equivalent stress σ^{eq} and (b) relative axonal strain $\hat{\varepsilon}$ of a cross-section of the CVE with the spherical inclusion for a loading angle of $\phi = 0°$.

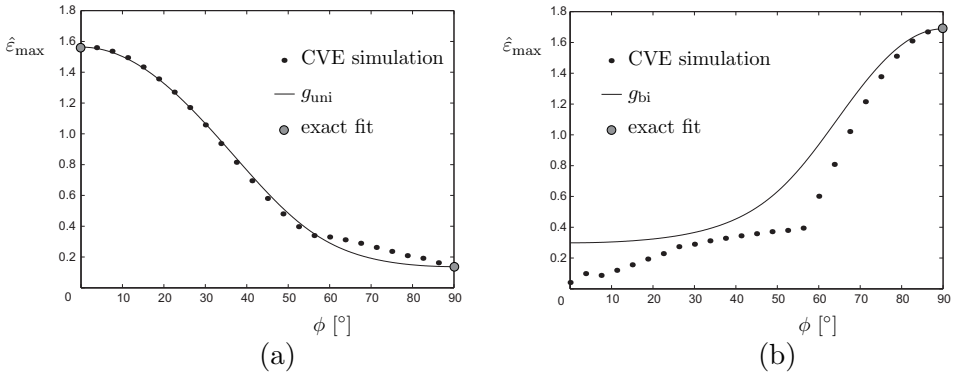

Figure 4.8: The maximum relative axonal strain versus the loading angle ϕ for (a) uniaxial and (b) biaxial deformations for the CVE with a spherical inclusion. In both plots, the line represents function g (Equations 4.20 and 4.21 for (a) and (b), repectively) and the dots refer to the maximum relative axonal strain obtained from the CVE simulations.

the inclusion as well as of the local differences in mechanical stiffness. The variation in axonal orientation also causes a part of the axons to be more aligned with the loading direction for higher loading angles resulting in higher relative strains at loading angles for which the axons are not loaded in tension in the homogeneous case. An exact agreement with the CVE results is obtained for $\phi = 0°$ and $90°$ for the uniaxial deformation (Figure 4.8a) and for $\phi = 90°$ for the biaxial deformation (Figure 4.8b) as a consequence of choosing to satisfy Equations 4.22 to 4.24, 4.26 and 4.27 exactly. There is a close agreement between the results of the CVE and the anisotropic equivalent strain for uniaxial deformation with an R^2 value of 0.9947. The values of the coefficient of the equivalent strain measure can be found in Table 4.2. As a validation step, an overall reasonable agreement is found for biaxial deformation with an R^2 value of 0.8835, although differences can be noticed around a loading angle of $\phi = 60°$ and below $\phi = 20°$.

For the CVE with a cylindrical inclusion, of which the simulation results are depicted in Figure 4.9, the relative strain is not only a function of loading angle ϕ, but also of loading angle θ, where loading occurs in the main axonal direction for $\phi = 0°$ and in the direction of the axis of the

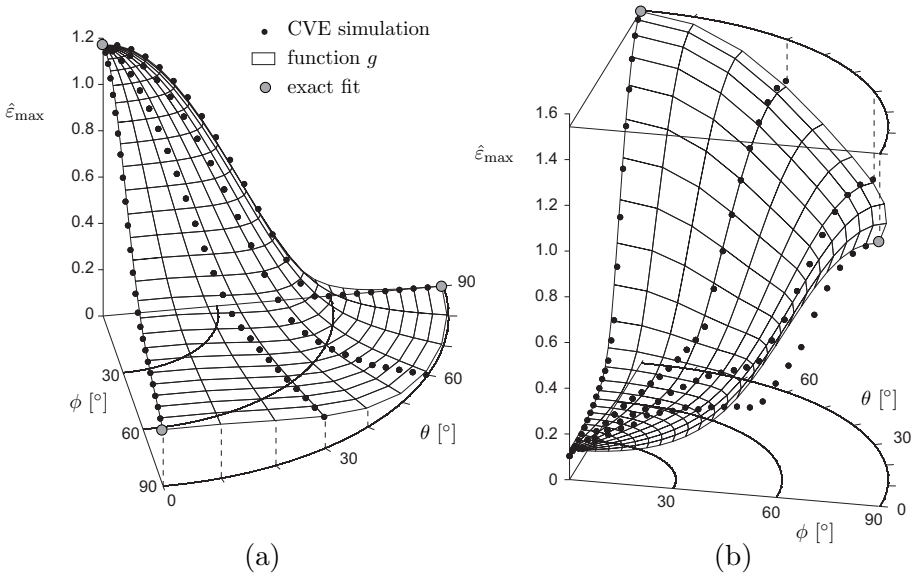

Figure 4.9: The maximum relative axonal strain versus the loading angles ϕ and θ for (a) uniaxial and (b) biaxial deformations for the CVE with a cylindrical inclusion. In both plots, the surface represents function g (Equations 4.20 and 4.21 for (a) and (b), repectively) and the dots refer to the maximum relative axonal strain obtained from the CVE simulations.

cylindrical inclusion for $\theta = \phi = 90°$. In the case of uniaxial deformation, a relative strain of about 1.2 is reached, but this value is approximately 1.6 for biaxial deformation. An exact agreement with the CVE results is obtained for $\phi = 0°$ and for $\phi = 90°$ with $\theta = 0°$ and $\theta = 90°$ for the uniaxial deformation (Figure 4.9a) and for $\phi = 90°$ with $\theta = 0°$ and $\theta = 90°$ for the biaxial deformation (Figure 4.9b). A close agreement between the results of the CVE and the anisotropic equivalent strain for uniaxial deformation is achieved with an R^2 value of 0.9965. The values of the coefficients of the equivalent strain measure are summarized in Table 4.2. Furthermore, an overall reasonable agreement for biaxial deformation is obtained with an R^2 value of 0.9658.

Figure 4.10 shows the effect of the orientation of the main axonal direction

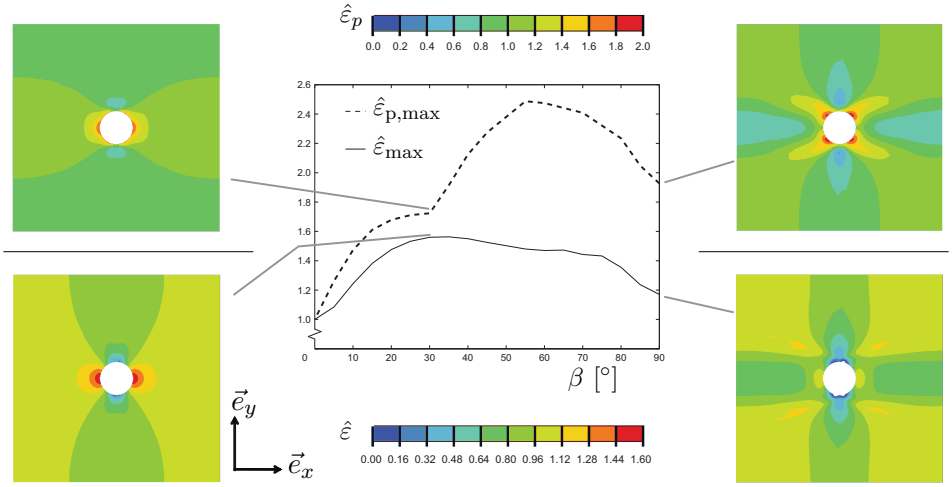

Figure 4.10: The maximum relative axonal strain $\hat{\varepsilon}_{\mathrm{max}}$ and the relative maximum principal tissue strain $\hat{\varepsilon}_{\mathrm{p,max}}$ plotted against the angle β between the main axonal orientation and the long axis of the cylindrical inclusion. The field plots show the relative axonal strain $\hat{\varepsilon}$ and the relative maximum principal tissue strain $\hat{\varepsilon}_p$ of a cross-section of the CVE with a cylindrical inclusion.

with respect to the blood vessel for a uniaxial deformation in the main axonal direction with β the angle between the main axonal direction and the direction of the blood vessel. For $\beta = 90°$, the relative maximum axonal strain is approximately 1.2 and it reaches a maximum value close to 1.6, if the main axonal direction is at 30° relative to the cylindrical axis. In the two lower field plots in Figure 4.10, it can be seen that the highest relative axonal strains are located equatorial to the inclusion cross-section, where not only the influence of the inclusion is felt, but also the axons are aligned with the loading direction. The field plot representing the relative maximum principal tissue strain, defined as the local maximum principal strain with respect to the global maximum principal strain, on the upper right hand side of Figure 4.10, shows that the highest values are at locations diagonally with respect to the inclusion, at which the axons are locally deviating most from the loading direction and therefore also at which the tissue locally has the lowest stiffness in the loading direction. This effect

gets stronger if β decreases until 55° and then diminishes again for lower angles of β, because the more the loading direction is aligned with the long axis of the cylindrical inclusion, the less the mechanical influence of the inclusion is. Consequently, with decreasing angles of β, the location of the maximum principal tissue strain moves towards the region equatorial to the inclusion in the cross-section as can be seen in the upper left hand side of Figure 4.10. These combined effects cause the relative maximum axonal strain to show a peak at $\beta = 30°$.

In the previous results, the global stretch $\bar{\lambda}$ was 1.001, which is below levels that are typically associated with DAI. To obtain the influence of higher global strain levels on the maximum relative axonal strain, the results of simulations with the CVE with a spherical inclusion with global stretch levels of 1.001, 1.01 and 1.1 are depicted in Figure 4.11. It can be observed that the overall relation between the maximum relative axonal strain from the CVE and the loading angle is similar for all three levels of global stretch. For global stretch levels of 1.001 and 1.01, the difference between resulting maximum relative axonal strains is less than 4%. For a global stretch of 1.1, the maximum relative axonal strain is 14% smaller at $\phi = 0°$ than for a global strain of 1.001. This difference decreases for higher loading angles, but for loading angles larger than 60°, the relative difference increases again, although at these loading angles the maximum relative axonal strain is small.

4.4 Discussion

In this study, an anisotropic equivalent strain measure based on axonal loading is introduced. The results show that it is capable of describing the effects of microstructural heterogeneity on axonal injury due to tissue-level mechanical loading. From simulations with critical volume elements, it was observed that locally axonal strains may be significantly larger than the overall tissue strain and that the level of axonal stretching depends strongly on the direction of loading. In Chapter 3, it was concluded that factors that influence the axonal strain relative to the applied tissue strain are: (i) the inclusion stiffness relative to the surrounding tissue, (ii) the main axonal orientation, (iii) the mechanical anisotropy and (iv) the local deviation in

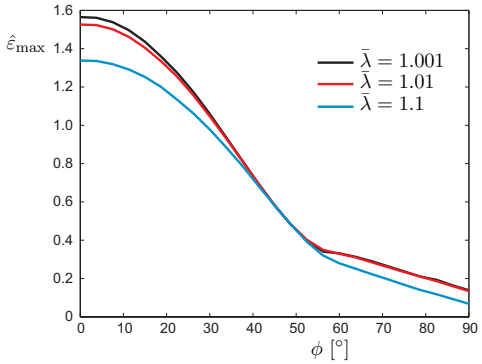

Figure 4.11: The maximum relative axonal strain $\hat{\varepsilon}_{\max}$ as a function of the loading angle ϕ with different global strain levels for the CVE with a spherical inclusion.

axonal orientations. The three-dimensional CVEs of the current study provide two important additional insights into the micromechanical effects of brain injury. Firstly, a spherical inclusion leads to higher axonal strain relative to the applied tissue strain compared to a cylindrical inclusion that is oriented perpendicular to the main axonal direction. The latter configuration is similar to the previously investigated two-dimensional cases described in Chapter 3. Secondly, higher values of the relative maximum axonal strain are observed in the three-dimensional CVE if the angle between the axis of the cylindrical inclusion and the main axonal direction is varied, and in the most critical case, they are similar to those of the spherical inclusion.

The effect of the microstructural heterogeneity in the CVE with the cylindrical inclusion depends on the loading direction in the three-dimensional space. This CVE is representative for a critical volume in the brain tissue near e.g. a single blood vessel. In reality, however, a distribution of randomly oriented blood vessels could exist. In that case, the combined effect of various CVEs with a cylindrical inclusion in all different directions with respect to the main axonal direction should be considered. Therefore, the sensitivity of the tissue to mechanical strains becomes transversely isotropic, similar to the CVE with a spherical inclusion. Since it has been shown that the highest axonal strains, which are obtained at a specific

angle between the axis of the cylindrical inclusion and the main axonal direction, are similar to those of the CVE with a spherical inclusion, it can be concluded that the latter CVE could represent a network of blood vessels as well. Nevertheless, the main focus of this research is to develop an anisotropic equivalent strain measure to predict brain injury that is generally applicable, even for the complex micromechanical effects of tissue with uniaxially oriented cylindrical inclusions.

The proposed anisotropic equivalent strain measure can be used to obtain local maximum axonal strain levels directly from a macroscopic FE head model. The equivalent strain measure was found to capture the orientation dependent sensitivity to mechanical loads for the different cases considered in this study and is expected to be generally applicable to other configurations as well. Although the axonal strains relative to the tissue strains obtained from the simulations have not been validated experimentally, the coefficients of the equivalent strain could also be obtained from deformation-controlled tissue-level injury experiments of a similar type as performed in literature (e.g., [62,78,138]). In that case, the coefficients are determined such that the equivalent strain describes actual injury rather than axonal strains. Then, if a threshold is obtained for injury, the equivalent strain can be used as an anisotropic brain injury criterion.

Although in reality the size and the shape of the inclusion can differ from the simulations in this study, in this continuum mechanics-based modeling approach, for a given orientation field, the results are independent of the length scale of the inclusion. However, the local orientation field does affect the results and this orientation field may depend on the size of the inclusion. It follows from the results that the most important reason for the dependency on the loading direction is the local axonal orientation. It is therefore expected that other sizes or shapes of the inclusion will result in similar relative maximum axonal strain values as the CVE with the spherical inclusion.

The mechanical behavior of brain tissue is known to be viscoelastic. However, no viscoelastic behavior has been included in the CVE models, since the loading path is not complex. In Chapter 5, in which the anisotropic equivalent strain as well as a viscoelastic CVE is applied to an FE head model, is is concluded that the outcome of both approaches is nearly identical. Therefore, the orientation dependence of the anisotropic equivalent

strain measure is independent of the head level loading type or rate. Nevertheless, the strain field predicted by an FE head model, to which the anisotropic equivalent strain should be applied, will depend on the viscoelastic constitutive description of brain tissue in the head model.

In pathological studies, locally injured axons are found in between intact axons [141,150]. The CVE in the current study cannot predict these individually injured axons, since the axonal tissue in the CVE is modeled as a continuum. However, since these injuries are always present within areas where the axonal orientation is deviating in its course due to an obstruction, it is assumed that the strain concentrations from the continuum axonal material are sufficient to relate axonal injury to tissue loads. Furthermore, the anisotropic equivalent strain measure can not only capture the micromechanical effects as observed in the CVEs, but also the relative axonal strain for a homogeneous case, where the mechanical behavior has no influence at the microscale.

In the current study, only axonal-level simulations are conducted. However, if the CVE or the anisotropic equivalent strain measure are used in FE head models, the full potential of these techniques will be achieved. For this purpose, the main axonal orientation should be included in the FE head model (e.g., [64,65] or Chapter 5), where the CVE or the anisotropic equivalent strain measure is applied in a local coordinate system within the head model.

In the present simulations, the effects of a possible undulation of the axons have not been accounted for. Bain and co-workers [87] concluded that already at zero strain, parts of the axons are fully coupled to their surroundings, which causes them to deform in an affine manner with respect to their surroundings. Although the maximum axonal strain relative to the applied tissue strain is expected to become less dependent of the loading direction as a result of the undulation for small strains, it is expected to have no influence for larger strains at which DAI could occur and the axons are not undulated anymore.

4.5 Conclusion

For DAI, different length scales play an important role, where the mechanical load occurs at the head level and the injury is occurring at a much smaller cellular level. Simulations with different CVEs in this study show that the heterogeneities at the cellular level result in elevated axonal strain levels that may cause axonal injury and that the magnitude of these axonal strains depends not only on the magnitude of the deformation at the tissue level, but also on the direction of tissue loading relative to the orientation of the microstructure. Current FE head models should account for these micromechanical effects for a better prediction of DAI. The anisotropic equivalent strain measure that is developed in this study is capable of describing an orientation dependence of axonal strains resulting from tissue strains. Therefore, the anisotropic equivalent strain measure can be applied to FE head models in order to relate predicted strain fields to axonal strain levels, from which a better prediction of DAI is possible. Furthermore, the parameters of the anisotropic equivalent strain measure can also be obtained from deformation-controlled experiments. From this type of experiments, the coefficients can be derived directly for injury as a consequence of tissue loading in different directions resulting in an anisotropic brain injury criterion. This study shows that the equivalent strain measure can be fitted to agree well with the results of the CVEs that were modeled as good as possible based on current knowledge. However, it is expected that the equivalent strain measure can also be fitted well on future improved simulations and/or experiments at both the cellular and the tissue level.

Chapter five

Multi-scale Mechanics of Traumatic Brain Injury

5

The length scales involved in the development of diffuse axonal injury typically range from the head level (i.e., mechanical loading) to the cellular level. The parts of the brain that are vulnerable to this type of injury are mainly the brainstem and the corpus callosum, which are regions with highly anisotropically oriented axons. Within these parts, discrete axonal injuries occur mainly where the axons have to deviate from their main course due to the presence of an inclusion. The aim of this study is to predict axonal strains as a result of a mechanical load at the macroscopic head level. For this, a multi-scale finite element approach is adopted, in which a macro-level head model and a micro-level critical volume element are coupled. The results show that the axonal strains cannot be trivially correlated to the tissue strain without taking into account the axonal orientations, which indicates that the heterogeneities at the cellular level play an important role in brain injury and reliable predictions thereof. In addition to the multi-scale approach, it is shown that a novel anisotropic equivalent strain measure can be used to assess these micro-scale effects from head level simulations only.

Reproduced from: R.J.H. Cloots, J.A.W. van Dommelen, S. Kleiven and M.G.D. Geers (2011). Multi-scale Mechanics of Traumatic Brain Injury: Predicting Axonal Strains from Head Loads. (Submitted)

5.1 Introduction

The brain is a vulnerable part of the human body in case of an accident, such as in a road traffic crash situation. In Europe, which has a total population of 330 million people, about 50,000 people die because of traumatic brain injury (TBI) each year [89]. Diffuse axonal injury (DAI) is one of the most frequently occurring types of TBI [140]. It is primarily involved with dynamic non-contact loading, although it is believed to occur in closed head impacts as well [118,119].

In order to improve the prevention and diagnosis of TBI, a better understanding of the relation between mechanical loading and TBI is necessary. Therefore, brain injury criteria are developed that can predict TBI as the result of a mechanical load. The most used brain injury criterion in the automotive industry nowadays is the head injury criterion (HIC), which is based on head level kinematics [32]. Although the mechanical loading occurs at the head level, injury of the brain is often the result of more local mechanical phenomena. Because of this, more sophisticated brain injury criteria are needed to recover the local mechanics. For this purpose, three-dimensional finite element (FE) head models are developed that simulate the response to a mechanical loading of the head to assess the risk of TBI (e.g., [36–38,97]). FE head models have a good potential to predict DAI, since they describe local deformations within the brain [102,119]. However, an indisputably well-defined correlation between mechanical loading and DAI using FE head models has not been achieved yet. A possible explanation is that in most of the currently used head models, anisotropic mechanical behavior of brain tissue is not included, even though experimental studies have concluded that neural tissue behaves clearly anisotropically in some regions of the brain (e.g., [48,51,52,58,88,151]). In line with this, recent studies have been performed that take the axonal orientation into account leading to tissue strains in the axonal direction [64,66]. Nevertheless, even if tissue strains could be predicted accurately by head models, the link to real injury is still not straightforward, as several studies concerning TBI have shown that tissue strains lead to injury at a cellular level (e.g., [53,60,62,63,79,101]), whereby the microstructural heterogeneities at the cellular level are of influence.

Brain tissue contains neurons and glial cells, which both consist of a cell

body from which processes (i.e., axons and dendrites) extend [21,22]. The diameters of the cell bodies are about 5 μm for the glial cells and often less than 10 μm for nonpyramidal cells and up to 20 μm for other cortical and hippocampal neurons [67–72]. The cell bodies are mainly residing in the cortex, but their axons, which have a uniform diameter, extend into the white matter regions and can be many centimeters long [73].

In Chapter 3, a micro-level critical volume element (CVE) was developed based on the pathological study of Povlishock [141], in which it was observed that axonal injury is only present at locations where the axons have to deviate from a straight path because of an obstruction (e.g., a blood vessel or a cell body). This viewpoint is still supported in more recent literature [124,125]. This pathological observation indicates that those axons might be subjected to locally higher strains than the tissue level strains, because of mechanical heterogeneities at the axonal level, which is discussed in Chapter 3. Furthermore, it shows that a region with axons near an inclusion can be considered as a critical region for axonal injury. Moreover, in the pathological observations of brain-injured humans, Povlishock found axonal damage mainly within white matter regions, such as the brainstem and the corpus callosum.

This influence of the microstructure of the tissue might induce an orientation dependence of the sensitivity of brain tissue to a mechanical load in regions where the tissue has a unidirectionally oriented structure. This highlights the importance of taking into account microstructural aspects of the tissue in tissue-level brain injury criteria.

Within this context, the aim of this study is to investigate the local axonal strains near an inclusion in relation to the tissue level strains of the brainstem and the corpus callosum during mechanical loading of the head. To achieve a coupling between an FE head model that does not contain details at a cellular level and local axonal strains, a multi-scale framework with a macroscopic head model and a microscopic critical volume element (CVE) is used. Both levels are solved with the FE method. The CVE is constructed on the basis of microscopic pathological findings for DAI. An approximate single scale approach to include cellular level effects in the same FE head model (without using a CVE) is pursued through an anisotropic equivalent strain measure that can estimate axonal strains directly from head model tissue strains, which is described in Chapter 4. To

investigate to capability of the anisotropic equivalent strain measure to account for microstructural effects (as modeled in a CVE), the outcome of both approaches will be compared.

5.2 Methods

In this section, first, the multi-scale method will be explained, whereas the anisotropic equivalent strain measure will be explained further on. For the multi-scale approach, at the macro level an FE head model is used and at the micro level a CVE is developed (see Figure 5.1). To achieve this, the influence of the microstructural configuration as well as the anisotropic sensitivity of the tissue to mechanical loads should be accounted for. The FE head model is originally developed by Kleiven [37] and for the current study, it is extended with anisotropic tissue behavior. The CVE developed in this study represents a microstructural configuration that is critical for axonal injury. In Figure 5.2, it is shown schematically how the head model and the CVE are coupled in the multi-scale framework. Macroscopic loading conditions are based on the reconstruction of a real sports accident [37,152] and are imposed on the head model. After the simulations of the

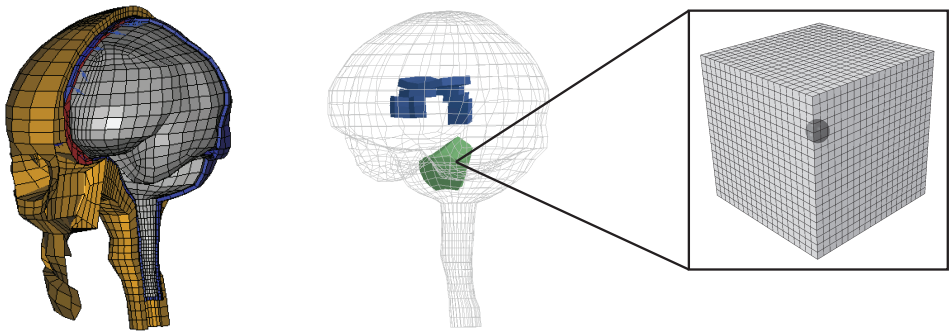

Figure 5.1: Models at the macroscopic and the microscopic level: (a) head model, (b) head model showing the brainstem and the corpus callosum and (c) critical volume element.

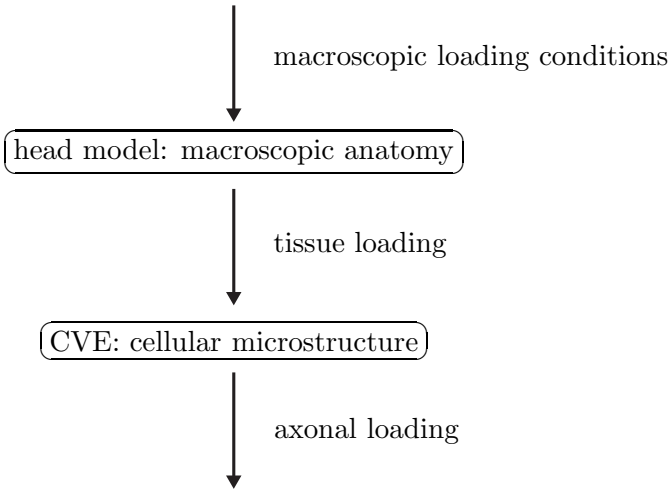

Figure 5.2: Schematic representation of the computational multi-scale implementation.

head model are completed, the obtained internal brain tissue loading response from the head model is used as a loading condition for the CVE, where for each integration point in the regions of interest of the head model a separate CVE simulation is conducted. The outcome of the CVE simulations is the axonal loading, where the orientation of the axons are taken into account. For completeness, a situation is also simulated in which no inclusion is present in the microstructure by directly taking the logarithmic tissue strain obtained in the head model in the macroscopic local main axonal direction (i.e., without a CVE simulation).

Since the discrete focal impairments of the axons are often found in the brainstem and the corpus callosum, focus is put on these parts of the head model. In order to perform an in-depth study of the axonal strains in the CVE in relation to the tissue strains in the brainstem and the corpus callosum of the head model, one specific injurious loading case of the head model is considered, where for each element of the brainstem and the corpus callosum a CVE simulation is performed.

5.2.1 Head model

The head model used in this study is based on the model developed by Kleiven [37] in the FE code LS-DYNA 971 (LTSC, Livermore, CA), which consists of 11,158 eight-node hexahedral elements, 10,165 four-node shell and membrane elements, and 22 two-node truss elements. The simulations are performed in the dynamic regime with an explicit integration scheme. For this study, the material behavior of the brain tissue is described by a viscoelastic fiber-reinforced anisotropic material model. This model is implemented as a user material of which the hyperelastic strain energy potential is:

$$W = \frac{G}{2}(\tilde{I}_1 - 3) + K\left(\frac{J^2-1}{4} - \frac{1}{2}\ln J\right) + \frac{k_1}{2k_2}\left(e^{k_2\langle\tilde{E}\rangle^2} - 1\right), \qquad (5.1)$$

where the third term on the right hand side is based on the Holzapfel-Gasser-Ogden form [132], with only one fiber family here, with

$$\tilde{E} = \kappa(\tilde{I}_1 - 3) + (1 - 3\kappa)(\tilde{I}_4 - 1), \qquad (5.2)$$

where G is the shear modulus, K is the bulk modulus, $\tilde{I}_1$ is the first invariant of the isochoric right Cauchy-Green deformation tensor $\tilde{\boldsymbol{C}} = J^{-\frac{2}{3}}\boldsymbol{C}$ with $\boldsymbol{C}$ the right Cauchy-Green deformation tensor and $J = \det(\boldsymbol{F})$ is the volume change ratio. Furthermore, $\tilde{I}_4 = \tilde{\boldsymbol{C}} : \vec{n}_0\vec{n}_0$ is the isochoric fourth invariant where $\vec{n}_0$ is the fiber direction vector in the reference configuration with unit length; k_1 is the scalar fiber stiffness, and κ is the dispersion of the fiber orientations around the preferred fiber direction $\vec{n}_0$. The two limits of κ are 0 for fully aligned fibers (i.e., transverse isotropy) and $\frac{1}{3}$ for randomly oriented fibers (i.e., isotropy). Therefore, the value of κ is related to the degree of anisotropy. By means of the Macaulay brackets $\langle\cdot\rangle$, the fibers contribute only in tension and not in compression, as $\langle\tilde{E}\rangle$ becomes 0 if $\tilde{E}$ is negative. The fiber contribution to the stiffness is assumed linear (i.e., $k_2 \to 0$) [58]. Viscoelasticity is added by using:

$$\boldsymbol{S}(t) = \int_0^t \left[M_\infty + \sum_i M_i \exp\left(-\frac{t-\tau}{\tau_i}\right)\right] \frac{\partial \boldsymbol{S}^e}{\partial \tau} d\tau, \qquad (5.3)$$

where $M_\infty + \sum_i M_i = 1$, τ is a time variable that runs from from the initial time up to the current time t, $\boldsymbol{S}(t)$ is the current deviatoric second Piola-Kirchhoff stress tensor, $\boldsymbol{S}^e$ is the deviatoric elastic second Piola-Kirchhoff stress tensor as derived from the non-volumetric part of Equation 5.1 (i.e., the first and third term on the right side), M_∞ is the long term parameter recovering the role of the material parameters G and k_1 in the limit, M_i are the relaxation parameters of the viscoelastic modes and τ_i are the time constants. The volumetric behavior is assumed to be independent of time.

The material properties of the brain tissue are based on a combination of the experimental study of Ning et al. [58] on the brainstem of a 4-week old pig and the material properties of the brain tissue in the original head model [37]. The material properties used in the current study are given in Table 5.1. Since the original head model has been validated with isotropic mechanical behavior only, the mechanical response of the original and the extended model are expected to be similar in case the extended model would contain only isotropically oriented fibers (i.e., $\kappa = \frac{1}{3}$) in the brain tissue. Furthermore, the ratio of the parameter values for G and k_1 is assumed to be the same as the ratio in the study by Ning et al., although the absolute parameter values are not taken from this study. The fiber orientation is modeled fully uniaxially in the corpus callosum (lateral orientation), the brainstem (inferior-posterior orientation) and the spinal cord (inferior-

Table 5.1: Material properties of the brain tissue in the head model.

G (Pa)	1214	
k_1 (Pa)	11590	
M_1 for $\tau_1 = 10^{-6}$ s	0.7685	
M_2 for $\tau_2 = 10^{-5}$ s	0.1856	
M_3 for $\tau_3 = 10^{-4}$ s	0.0148	
M_4 for $\tau_4 = 10^{-3}$ s	0.0190	
M_5 for $\tau_5 = 10^{-2}$ s	0.0026	
M_6 for $\tau_6 = 10^{-1}$ s	0.0070	
M_∞	0.0025	
	Isotropic parts	Anisotropic parts
κ	$\frac{1}{3}$	0

posterior orientation), which will result in anisotropic mechanical behavior. For the remaining part of the brain tissue, the fiber orientation is modeled fully isotropic. In the original isotropic head model, the brainstem has a higher stiffness than the remaining brain tissue, which is here automatically accounted for by the increased stiffness from the fiber contribution in the inferior-posterior orientation. The bulk modulus of brain tissue is 2.1 GPa [133], but to prevent volumetric locking of the elements, a lower value of 50 MPa is used, which is still much higher than the shear modulus.

The loading conditions of the head model are based on a reconstruction case of an accident in the American National Football League with case numbers 57H2 [37,152]. This case is involved with loss of consciousness, which is often related to brainstem injury [153]. In Figure 5.3, the acceleration of the head model is shown.

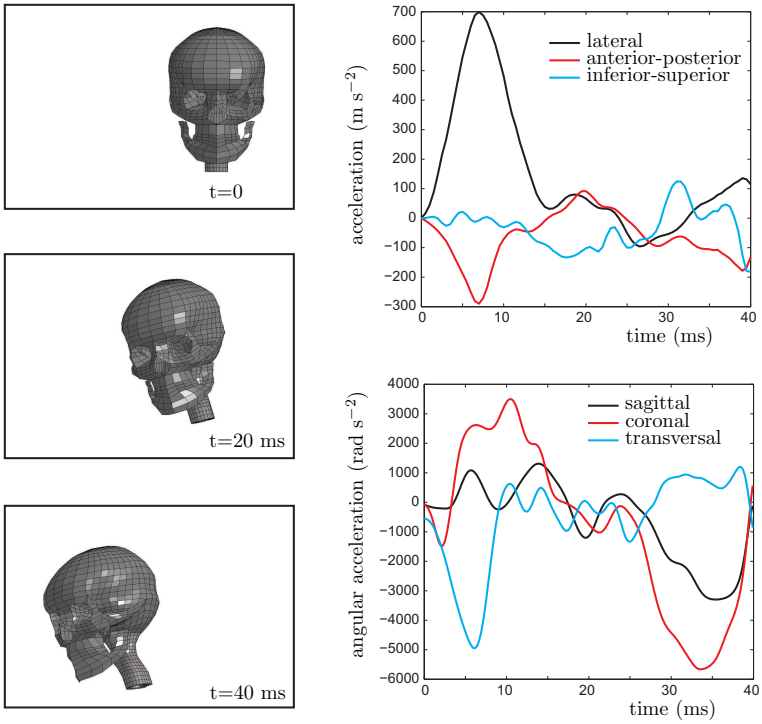

Figure 5.3: Head model loading condition based on the reconstruction of a struck sports player (case number 57H2 [152]).

5.2.2 Critical volume element

The CVE is developed using the FE code Abaqus 6.10-2 [145]. As opposed to the head model, the CVE is analyzed with a quasi-static computation with an implicit integration scheme. It contains 27,960 eight-node reduced integration hexahedral elements. The three-dimensional geometry of the CVE is based on pathological observations for axonal injury. It contains a spherical inclusion with a cross-sectional diameter of 8 μm and its surrounding material is assumed to consist of axons only. The inclusion and the surrounding tissue are assumed to be fully compatible at the interface. The tissue, consisting of axons, is modeled with a continuum approach. In line with the head model used at the macroscopic level, an anisotropic Holzapfel-Gasser-Ogden model [132] is used with the same properties as the head model. Note that volume associated to these critical locations is statistically small, so that the average tissue properties at the microstructural level correspond with those at the macroscopic level. Furthermore, the neurofilaments causing the anisotropic behavior are characterized by a much smaller length scale than the macro-level head model as well as the micro-level CVE. The same material model can therefore be used in the head model and the CVE without violating the separation of length scales. In order to obtain the axonal strains, each material point of the CVE has a specific orientation representing the local axonal orientation, which is depicted in Figure 5.4. The CVE simulations are conducted

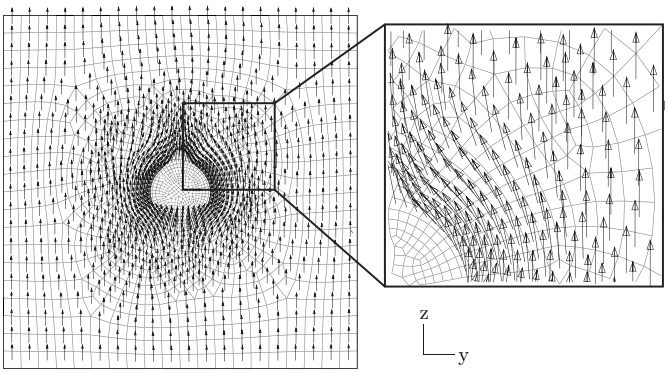

Figure 5.4: Cross-section of the CVE with the spatial discretization and the axonal orientation in each element of the part that consists of axons.

for material points (i.e., integration points in the FE discretization) of the brainstem and the corpus callosum in the head model and therefore, the main axonal direction in the CVE is aligned with the local axonal direction of the brainstem and the corpus callosum in the head model.

The behavior of the inclusion is also described with the Holzapfel-Gasser-Ogden model, but with isotropically oriented fibers (i.e., $\kappa = \frac{1}{3}$). To investigate the influence of the inclusion stiffness, three different values of the elastic parameters of the inclusion relative to those of the brain tissue are used: A) equal to those of the isotropic brain tissue, B) three times stiffer, and C) ten times stiffer. The bulk modulus is constant over the entire CVE and is equal to that of the head model. The material properties are shown in Table 5.2.

The loading conditions of the CVE are obtained from the deformation gradient tensor in the corresponding material point in the brain tissue as predicted with the head model and imposed by means of periodic boundary conditions [109]. The displacement vector $\vec{u}$ of a corner node c_i, as shown in Figure 5.5, is calculated from the global deformation gradient tensor $\bar{\boldsymbol{F}}$, which is obtained from the Green-Lagrange strain tensor in the head model, through:

$$\vec{u}_{\mathrm{c}_i} = (\bar{\boldsymbol{F}} - \boldsymbol{I}) \cdot \vec{x}_{0\mathrm{c}_i}, \tag{5.4}$$

in which $\vec{x}_0$ is the initial position vector and $\boldsymbol{I}$ is the unit tensor. Equation 5.4 is prescribed at the corner nodes c_1, c_2, c_4, and c_5. The nodal displacement vectors of the remaining parts of the boundary are tied as

Table 5.2: Material properties of the CVE.

	Axonal tissue	Inclusion		
		A (1x)	B (3x)	C (10x)
G (Pa)	1214	1214	3642	12140
k_1 (Pa)	11590	11590	34770	115900
κ	0	$\frac{1}{3}$	$\frac{1}{3}$	$\frac{1}{3}$
M_1 to M_6 and M_∞	see Table 5.1			

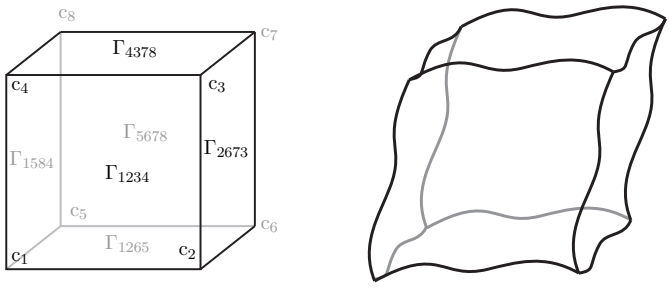

(a) (b)

Figure 5.5: CVE with (a) labeling of the corners and faces in the undeformed state and (b) deformed model with periodic boundary conditions.

follows:

$$\vec{u}_{\Gamma_{5678}} - \vec{u}_{\Gamma_{1234}} = \vec{u}_{c_5} - \vec{u}_{c_1}, \tag{5.5}$$
$$\vec{u}_{\Gamma_{2673}} - \vec{u}_{\Gamma_{1584}} = \vec{u}_{c_2} - \vec{u}_{c_1}, \tag{5.6}$$
$$\vec{u}_{\Gamma_{4378}} - \vec{u}_{\Gamma_{1265}} = \vec{u}_{c_4} - \vec{u}_{c_1}, \tag{5.7}$$

where Γ_{jklm} denotes the faces of the model (see Figure 5.5). As a result of these kinematical boundary conditions, antiperiodicity of the tractions is satisfied [109].

5.2.3 Anisotropic equivalent strain measure

In Chapter 4, an anisotropic equivalent strain measure $\bar{\varepsilon}^{\mathrm{eq}}$ has been developed that represents the maximum axonal strain as a result of the tissue strain components $\bar{\varepsilon}_{ij}$:

$$\begin{aligned}\bar{\varepsilon}^{\mathrm{eq}} = \big[&F(\bar{\varepsilon}_{yy} - \bar{\varepsilon}_{zz})^2 + G(\bar{\varepsilon}_{zz} - \bar{\varepsilon}_{xx})^2 + H(\bar{\varepsilon}_{xx} - \bar{\varepsilon}_{yy})^2 \\ &+2L\bar{\varepsilon}_{yz}^2 + 2M\bar{\varepsilon}_{zx}^2 + 2N\bar{\varepsilon}_{xy}^2\big]^{\frac{1}{2}} + I\bar{\varepsilon}_{xx}^d + J\bar{\varepsilon}_{yy}^d + K\bar{\varepsilon}_{zz}^d,\end{aligned} \tag{5.8}$$

This equivalent strain measure accounts for the orientation dependence governing the contribution of tissue deformations to axonal stretching. The coefficients of this equivalent strain were obtained from a CVE on which

isochoric uniaxial and biaxial deformations in all loading directions were applied. The values are given in Table 5.3 and they are obtained with a CVE with a spherical inclusion, in which the main axonal direction is in the y-direction. To simplify the analysis and eliminate the coupled solution at

Table 5.3: The values of the coefficients of the equivalent strain measure in Equation 5.8 as obtained from CVE calculations described in Chapter 4.

Coefficient	F	G	H	L	M	N	I	J	K
Value	0.163	-0.056	0.163	0.119	0.051	0.119	0.000	0.707	0.000

two scales, the equivalent strain measure can be used to replace the CVE as depicted in Figure 5.6. In the current study, the predictions based on this equivalent strain measure will be compared with the maximum axonal strain values obtained from the CVE simulations.

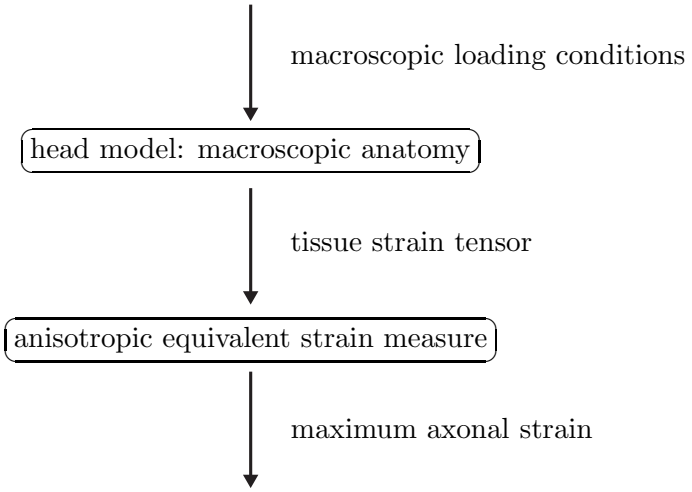

Figure 5.6: Schematic representation of the implementation of the anisotropic equivalent strain measure.

5.3 Results

In Figure 5.7, a strain field is shown for the head model, from which it is clear that elevated (macroscopic) strain levels up to 0.28 occur, especially around the brainstem. For this particular situation, in which loss of consciousness was observed, this indicates that the brainstem is a vulnerable part for injury in case an injurious mechanical load occurs.

The maximum axonal strains obtained from a CVE simulation as a function of the tissue strain in a specific material point in the brainstem and the corpus callosum are plotted in Figure 5.8. No clear relation between the axonal strain and the maximum principal tissue strain is observed, both for the simulations with and without an inclusion. Following the trajectory in time, it can be noticed that two peak values of the maximum principal logarithmic tissue strain are reached in the brainstem as well as the corpus callosum. For these two peak values, however, the ratio between the tissue strain and the maximum axonal strain is different. The presence of an inclusion leads to increased local maximum axonal strains in the tensile regime. Furthermore, the relation between the axonal strain and the tissue strain is also dependent on the angle φ (between the maximum principal

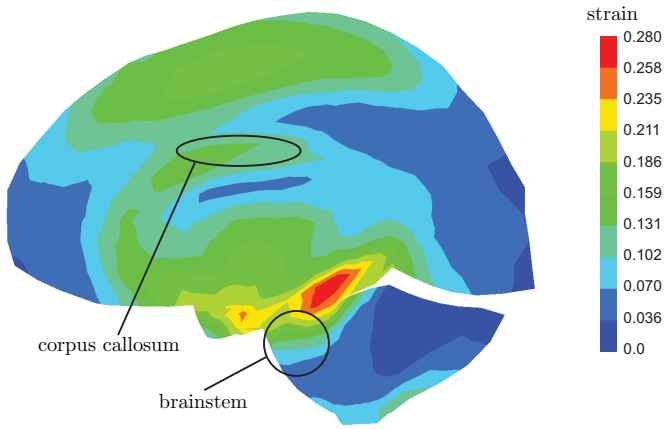

Figure 5.7: Maximum principal logarithmic strain of a sagittal cross section of the head model at 37 ms.

loading direction of the tissue and the main axonal direction), which is most pronounced in the trajectory without an inclusion. For this case, when the angle φ approaches 90°, a compressive axonal strain is found, whereas the maximum principal tissue strain is positive.

The influence of the stiffness of the blood vessel on the maximum local axonal strain is displayed in Figure 5.9. The inclusions A, B, and C have material properties that are nearly equal to the brain tissue, three

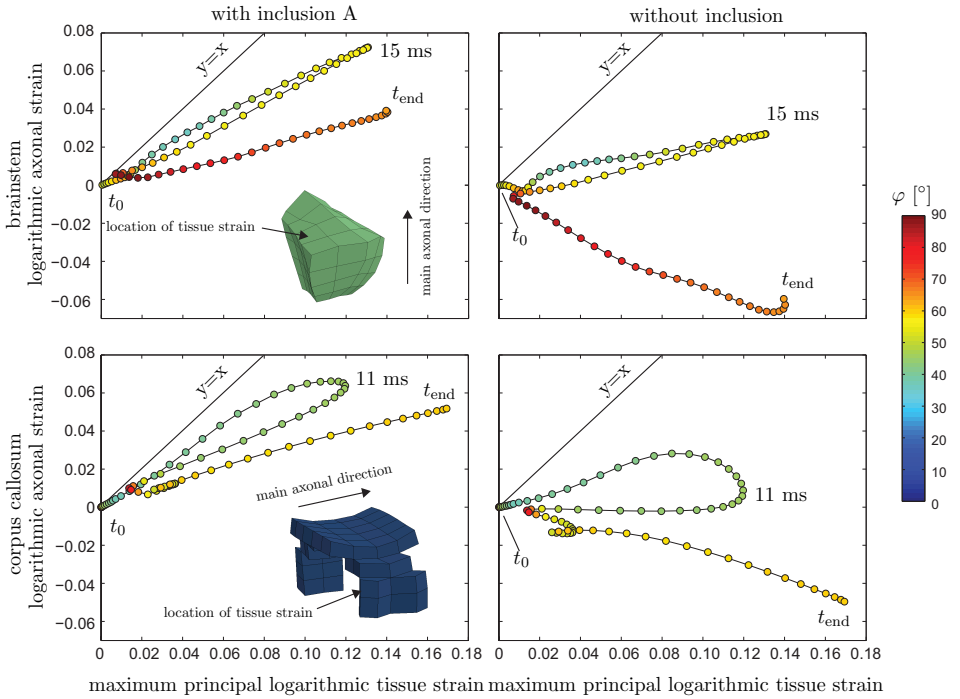

Figure 5.8: Time trajectory of the maximum axonal strain in the CVE versus the maximum principal tissue strain from t_0 to t_{end} during the mechanical loading for one point in the brainstem and one point in the corpus callosum in the head model. The inset shows the brainstem and the corpus callosum with an arrow indicating the material point of which the tissue loading is obtained. The colors refer to the angle φ between the maximum principal loading direction of the tissue and the main axonal direction.

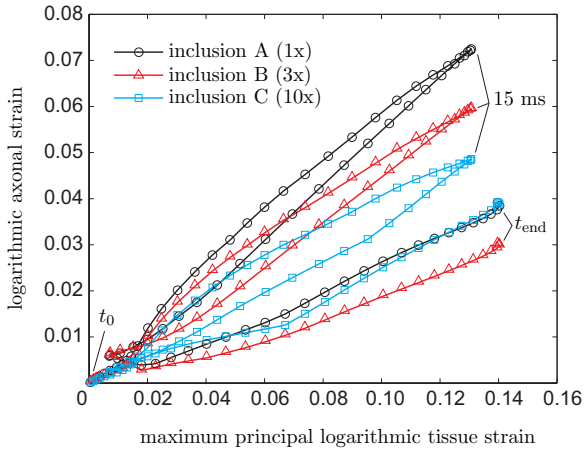

Figure 5.9: Trajectories of the maximum axonal strain in the CVE versus the maximum principal tissue strain from t_0 to t_{end} during the mechanical loading for the same location in the brainstem in the head model with three different degrees of stiffness of the inclusion.

times higher, or ten times higher, respectively. The only difference is that for all inclusions $\kappa = \frac{1}{3}$ as opposed to $\kappa = 0$ for the anisotropic brain tissue. Although the overall shape of the trajectory remains similar for all three cases, some important differences are present. At 15 ms, the axonal strain values are lower for an increased stiffness of the inclusion, whereby an increase with a factor 10 of the inclusion stiffness leads to a decrease of the maximum axonal strain by $\frac{1}{3}$. At time t_{end}, however, the effect of the stiffness is different, where the axonal strains for inclusion A and C are similar and those for inclusion B are lower. Because the surrounding brain tissue is anisotropic and the inclusion is isotropic, the stiffness of the inclusion relative to the brain tissue depends also on the loading direction, which causes the dissimilarities between 15 ms and t_{end}.

Figure 5.10 shows the axonal strain field of the CVE with inclusion A obtained from the material point in the brainstem (used for Figure 5.8) during the injurious load case at 15 ms. Adjacent to the inclusion, strain concentrations are present at the location where the local axonal orientation is most aligned with the tissue loading direction. One can also notice that

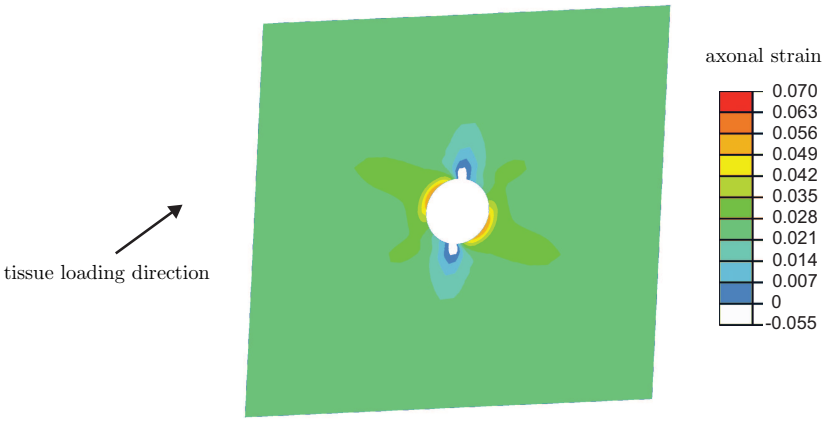

Figure 5.10: Cross section of the axonal strain field of the CVE at $t = 15$ ms in the brainstem. For clarity, the strain field of the inclusion is not depicted.

the axonal strain values more distant from the inclusion are in agreement with the strain values of the case without an inclusion (see Figure 5.8).

When the axonal strain is plotted against the maximum principal tissue strain for all elements of the brainstem in the head model at each time step (see Figure 5.11), it is observed that overall the maximum principal tissue strain is an overprediction for the maximum axonal strain in the CVE. The amount of this overprediction is partially related to the angle φ, where higher angles generally result in a larger overprediction. The results of the simulations with an inclusion show a good correlation between axonal and tissue strains for the range of angles φ from 0° to about 40°. However, still many local values deviate from these general observations. This indicates that the maximum principal strain observed in the tissue of the head model is not able to predict strains occurring at the axonal level due to the influence of axonal orientation. Furthermore, the inclusion causes the axonal strains to be larger than without an inclusion for the same tissue strains. Moreover, whereas compressive axonal strains are occurring for the situation without an inclusion, they are only in the tensile regime for the situation with an inclusion. This is caused by the local deviation of axonal orientation near the inclusion due to which at least some of the

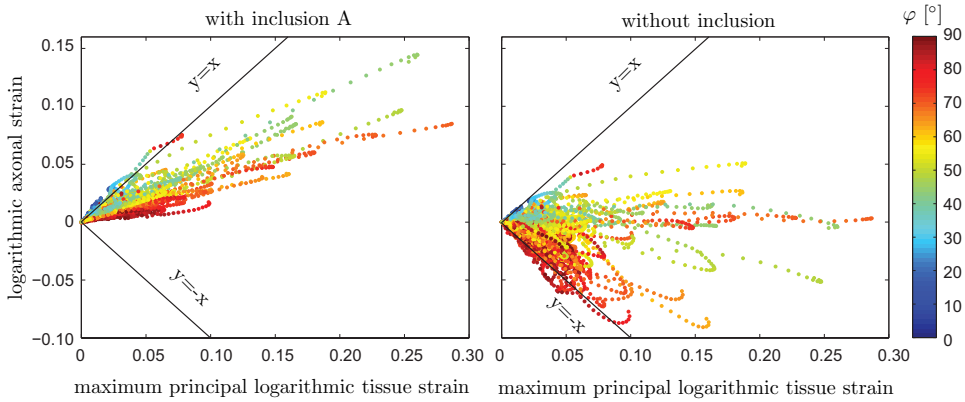

Figure 5.11: Maximum axonal strain in the CVE versus the maximum principal tissue strain at each time step during the mechanical loading for all elements of the brainstem in the head model.

axons are always fully or partially aligned with the tissue loading direction, which is not the case without an inclusion.

In a first step towards including the effects of axonal orientation, the (macroscopic) tissue strains in the main axonal direction are considered, for which it should be noted that this is the same as the axonal strain for a region without an inclusion. Figure 5.12 depicts the axonal strain of the CVE with an inclusion versus the tissue strain of the head model in the main axonal direction for all elements of the brainstem. For a situation without an inclusion, the same values would be plotted on both axes and therefore the line $y = x$ can be interpreted as the axonal strain value for a situation without an inclusion. It can be noticed that the inclusion causes the axonal strains to increase, in particular when the angle between the loading direction and the main axonal direction is large and the tissue strain is positive. Nevertheless, several instances with a smaller angle still lead to high axonal strains indicating that the tissue strain in the main axonal direction is not able to predict the local axonal strain accurately in case of an inclusion. Only for lower values of φ, the axonal strain shows a close agreement with the tissue strain in the main axonal direction. Furthermore, it is observed that also negative tissue strains in the main axonal direction lead to axonal stretching. The general observation is that the tissue strain in the main

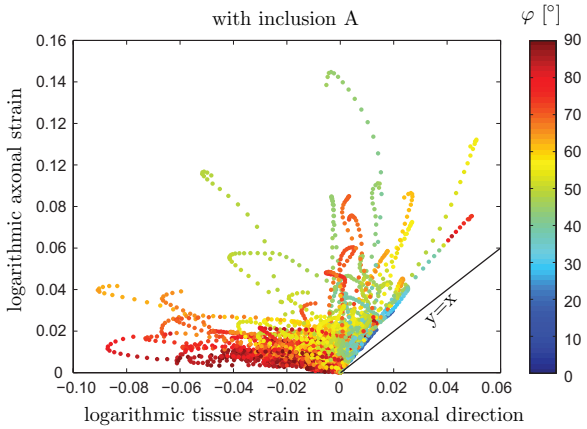

Figure 5.12: Maximum axonal strain in the CVE with an inclusion versus the tissue strain in the main axonal direction at each time step during the mechanical loading for all elements of the brainstem in the head model.

axonal direction is an underprediction of the maximum axonal strain in the presence of an inclusion and the amount of underprediction depends partially on the angle φ.

In Figure 5.13, tissue and axonal strains obtained in the brainstem and the corpus callosum are plotted as a function of time. The maximum axonal strains obtained from the CVE simulations are between the maximum principal tissue strain and the tissue strain in the main axonal direction during the entire simulation time. In the brainstem, the time-averaged relative differences of the maximum principal tissue strain, the tissue strain in the main axonal direction and the anisotropic equivalent strain with respect to the maximum axonal strain in the CVE are 2.05±0.19, 0.39±0.11 and 1.05±0.064 (mean±standard deviation), respectively. In the corpus callosum, the relative differences are 2.23±0.63, 0.33±0.17 and 1.05±0.059, respectively. The anisotropic equivalent strain agrees therefore the most with the maximum axonal strain in the CVE in terms of both the relative mean differences and the smallest standard deviations. For this loading case, the profile of the maximum axonal strain in the CVE is similar to that of the maximum principal tissue strain for the brainstem. However,

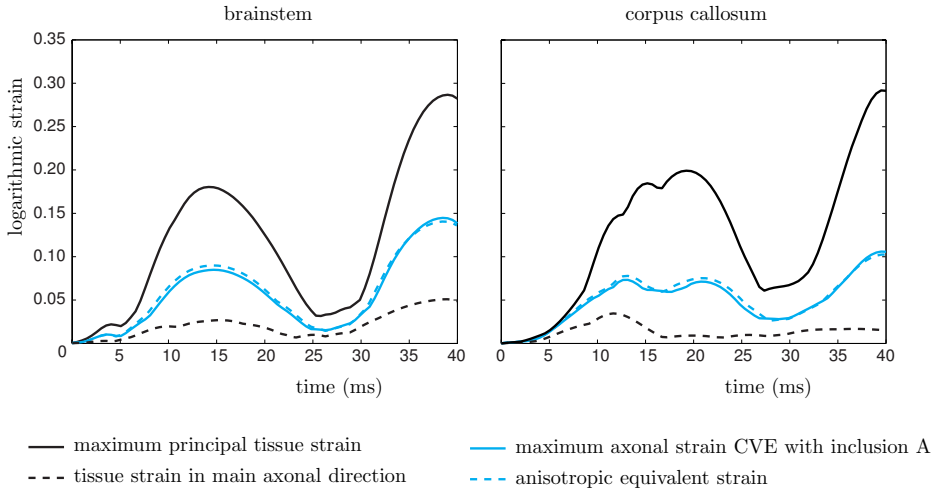

Figure 5.13: Maximum values of the tissue and the axonal strains versus time in the brainstem and the corpus callosum.

the profiles of the remaining tissue strains, in particular the tissue strain in the main axonal direction in the corpus callosum, deviate from the maximum axonal strain in the CVE (i.e., the standard deviations of the relative differences are large with respect to their mean values). This indicates that axonal strains cannot be generally obtained from the maximum principal tissue strain or the tissue strain in the main axonal direction. Furthermore, it can be noticed that the anisotropic equivalent strain, which is obtained directly from the tissue in the macroscopic head model, agrees well with the maximum axonal strain obtained from the CVE simulations.

For a more in-depth comparison between the CVE simulations and the anisotropic equivalent strain measure, the maximum axonal strain of the CVE simulations is plotted versus the anisotropic equivalent strain in Figure 5.14 for all material points of the brainstem. It can be observed that all dots are close to the solid black line that represents an exact agreement between the axonal strain and the equivalent strain. For large angles of φ, the outcome of the CVE is generally higher than the equivalent strain, whereas for small angles it is generally the opposite. The relative differences are 20% or less for equivalent strains higher than 0.06 and less than

7% for equivalent strains above 0.10. The overall R^2 value is 0.98. It is clear that the anisotropic equivalent strain is a better predictor for axonal strains as obtained from the CVE than the maximum principal tissue strain (see Figure 5.11, left hand side) and the tissue strain in the main axonal direction (see Figure 5.12).

The strain fields of the brainstem are shown in Figure 5.15 at 37 ms, when the highest strain values have been reached. The anisotropic equivalent strain is not only lower than the maximum principal tissue strain, but also the strain concentrations are in different points for either the anisotropic equivalent strain or the maximum principal tissue strain. Furthermore, the material point for which the highest equivalent strain in the brainstem is computed is the same as that obtained by means of the CVE simulations.

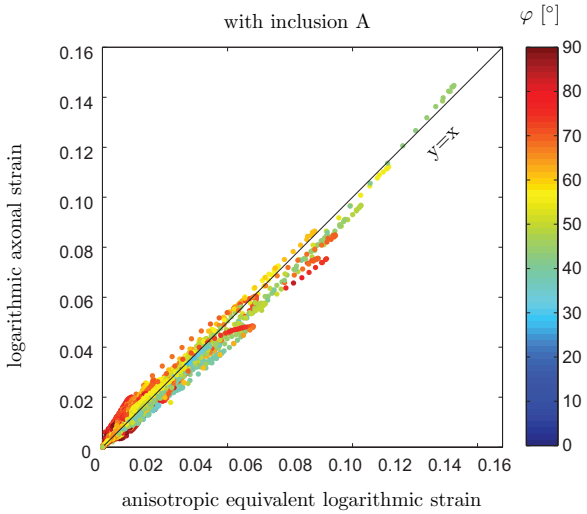

Figure 5.14: Maximum axonal strain in the CVE with an inclusion versus the anisotropic equivalent strain of the tissue at each time step during the mechanical loading for all elements of the brainstem in the head model.

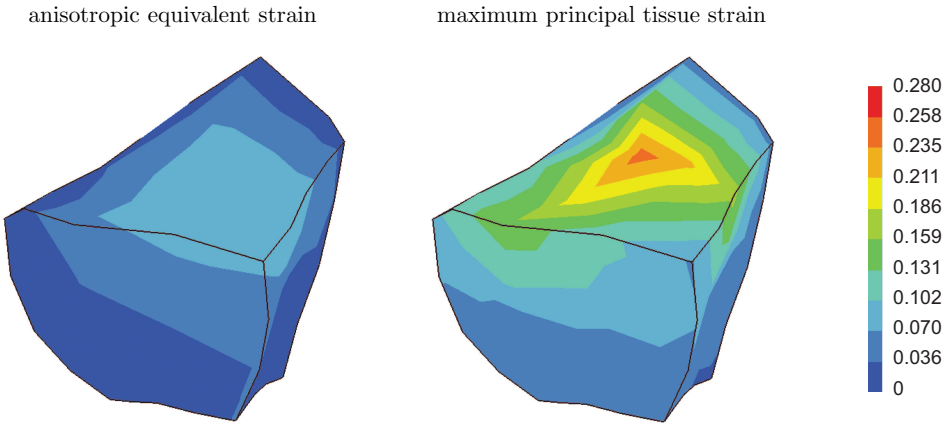

Figure 5.15: Field plots of the strain values in the brainstem at 37 ms for the injurious loading case 57h2.

5.4 Discussion

In this study, a multi-scale approach was used with a macroscopic FE head model to simulate the tissue response to mechanical loading and a micro-mechanical FE model of a CVE to obtain the local axonal strains due to the heterogeneities at the cellular level, which are assumed to be the cause of the discrete local axonal impairments in case of DAI. The strain values of the CVE and the FE head model have no trivial correlation. The maximum principal tissue strain in the FE head model is shown to be an overprediction for the maximum axonal strain in the CVE. In a study using the same FE head model, but with isotropic viscoelastic material behavior, performed by Kleiven [37], it was shown that loading conditions associated with concussion result in predictions of relatively high strain levels that are on the same level as suggested for DAI [59], even though the mechanical behavior for brain tissue in the model corresponds with the effective shear modulus of approximately 10 kPa at 80 Hz found for brain tissue in vivo by [154] using magnetic resonance elastography. The lack of correlation between between the tissue strain and the diagnosis of concussion in the study by Kleiven [37] might be explained by the overprediction of tissue strains for the interpretation of the maximum axonal strain, which

is shown in the current study. Furthermore, the tissue strain in the main axonal direction in the head model is shown to be an underprediction for the maximum axonal strain in the CVE. More importantly, the amount of over- and underprediction depends on the microstructure and the loading direction, which indicates that criteria for DAI should be developed taking into account the effects of the cellular level. In addition to the multi-scale method, an anisotropic equivalent strain measure (see Chapter 4) was implemented in the FE head model to estimate axonal strains through a single scale analysis. The equivalent strain was shown to be in close agreement with the outcome of the CVE simulations, whereas it requires only tissue strains predicted with a macroscopic head model and does not involve a multi-scale analysis. Therefore, since the CVE in this study is modeled with viscoelastic, anisotropic tissue behavior and the equivalent strain measure was originally developed for a hyperelastic, anisotropic tissue behavior, it can be concluded that viscoelasticity has no significant influence on the micro-level strains, unlike the tissue-level strains.

The FE head model has a geometry that distinguishes several parts of the brain (e.g., cerebral cortex, corpus callosum, brainstem). Although it does not include a detailed geometry (e.g., the folding structure of the cerebral cortex), the influence of these details are assumed to be local and therefore do not affect the tissue deformations of the brainstem and the corpus callosum. Although in reality, the brainstem would be more cylindrically shaped than in the model, the total volume is close to MRI volumetric measurements of the brainstem from healthy volunteers [37].

The loading conditions of the FE head model are based on the reconstruction of a specific injurious sports accident using HIII dummies [37]. Because of this, only the motion of the head could be applied directly to the head. Therefore, the possibly important influence of spinal cord bending could not be included in the analysis, which might affect the strain levels in the brainstem. Nevertheless, since this study is concerned with the maximum local axonal strains with respect to the tissue strains, the conclusions drawn are expected to remain valid for slightly different global mechanical loads.

The material properties of the head model were originally isotropic [37], but for this study the behavior was extended with anisotropy, because several studies have shown that areas of the brain with aligned axons reflect an anisotropic material behavior (e.g., [48,51,52,58,88,151]). In the origi-

nal isotropic head model, the brainstem was modeled with stiffer material properties than the remaining brain tissue. In the current study, it is assumed that the stiff nature of the brainstem is justified only in the main axonal direction due to the anisotropic behavior. Therefore, the current anisotropic head model contains the same material properties for the entire brain tissue, except for the fiber orientation distribution (i.e., either uniaxially aligned or randomly oriented).

In Chapter 3, it was shown that anisotropy at the tissue level causes the strains to become smaller in the main axonal direction, but larger in other directions for the same stress levels. For a homogeneous axonal alignment (e.g., without the presence of an inclusion) this would also lead to reduced axonal strains, even for the higher strain levels in other directions than the main axonal direction, since then the loading direction is not aligned with the axons anymore. However, when the axons have to deviate for an inclusion, partial alignment exists for a wider range of loading directions compared to the one without an inclusion. Hence, these axons have a higher strain locally caused by anisotropic material behavior. Nevertheless, the focus of this study is on the differences between the tissue-level strains and the axonal strains.

The CVE has a geometry with a simplified inclusion, which has a spherical shape that represents a cell body. In Chapter 4, also a cylindrical inclusion was used that represents a blood vessel. It was found that the most critical configuration of the cylindrical inclusion (i.e., main axonal direction about 30° with respect to the long axis of the cylinder) resulted in the same strain levels as with the spherical inclusion. Because blood vessels inside the brain are oriented rather randomly, it is assumed that this most critical configuration likely exists. The similar influence of the spherical and the most critical cylindrical configuration on the axonal strains, originates from the fact that the local axonal orientation with respect to the loading direction has a greater influence on the axonal strain than the actual shape of the inclusion. Therefore, it is assumed that the CVE with a spherical inclusion does not only adequately represent the case of a cell body, but also the case of a network of blood vessels. The stiffness of the inclusion relative to the surrounding axons has an influence on the axonal strain levels relative to the tissue strain level, but the overall relation between tissue and axonal strains remains similar.

Currently, the CVE is coupled only to the brainstem and the corpus callosum of the head model. Because also other parts of the brain can be involved with DAI, it may be necessary to couple these parts as well. In general, axons in other parts of the brain are less aligned, which will probably result in a different relation between the axonal strains and the tissue strains than for the brainstem and the corpus callosum. Also, different regions of the brain could have different tolerance criteria at the cellular level, which has been shown in a study by Elkin and Morrison [155]. This indicates there are more microstructural aspects that might play a role in cellular-level injury and that have not been included in the CVE used in the current study. Furthermore, the brainstem and the corpus callosum have a relatively simple geometry, whereas other parts of the brain might need more detailed geometries of the FE head model to obtain realistic tissue deformations. A more extended implementation of anisotropy could therefore be realized in the FE head model created by automatic segmentation and meshing based on medical images with a mesh size of 1 mm^3, which was developed recently [40]. The simulations of this more detailed model showed a similar correlation with the localized brain motion experiments of Hardy et al. [156], as observed for the model used in the present study.

5.5 Conclusion

This study shows that axonal strains deviate from the maximum principal tissue strains as well as from tissue strains in the main axonal direction that are predicted in an FE head model, where the tissue strains are an overprediction or an underprediction of the maximum axonal strains, respectively. The main observation, however, is that tissue strains do not consistently scale with the maximum axonal strain, since the amount of over- and underprediction depend on the loading direction relative to the main axonal direction. This is caused by the local heterogeneities at the cellular level, which are local axonal orientation, difference in stiffness between the axons and the inclusion, and the anisotropic material behavior of the axons. The latter factor also influences the tissue strain in the FE head model. Since DAI is a type of injury in which the mechanical load occurs at the head level and the actual injury occurs at the cellular level, a multi-scale method with an FE head model and a CVE is a promising approach to obtain cel-

lular based injury criteria. Furthermore, a single scale alternative to the multi-scale approach is the anisotropic equivalent strain measure, which can be used to obtain axonal strains directly from tissue-level strains. In combination with a critical value for injury, this measure can be used as an injury criterion.

Chapter six

Discussion, conclusions and recommendations

6

6.1 Discussion and conclusions

The brain is probably the most important part of a human body. With it, we can control our body in terms of movement, thinking and many other functions, both intentionally and unintentionally. At least, if one is healthy. More than any other part of the body, it determines the human being as a whole. Therefore, it is protected well against injury caused by external chemical and mechanical influences by a range of natural mechanisms. However, because brain tissue is a very delicate tissue, it is still vulnerable to injury caused by mechanical loading of the head despite the protection of for example the skull. Accidents that involve a severe loading of the head may lead to injury of the brain.

The brain has been a subject of research for thousands of years [157] and the biomechanics of TBI has been studied for many decades [27,104]. In spite of that, the understanding of the mechanisms related to TBI is still far from complete. One reason for this is that many processes are involved with TBI simultaneously and continue long after the original mechanical insult, leading to full or partial loss of functioning, which can be permanent or temporary. Another reason concerning the difficulty in trying to understand the true aspects of TBI is the complex anatomy of the brain, including the substructures, the network of nerves and the many cells, which makes it

hard to characterize the mechanical behavior. Both reasons, though, have one aspect in common: they occur at several length scales at the same time. Therefore, TBI is truly a multi-scale phenomenon. In this study, the objective was to obtain a relation between the processes at these length scales. This has been achieved by developing computational models that bridge the mechanics of the brain's substructure and the tissue as well as the tissue and the axons.

In Chapter 2, the development of a meso-level plane strain FE model is described that is able to relate head loads to local tissue stresses by describing the influences of the substructures of the cerebrum. The results of the simulations show elevated levels of tissue stress near the bottom of the sulci during the head loading. The agreement with local injuries that were observed by Strich [117] indicates that these injuries are possibly triggered by the locally increased deformations. The anatomical details of the cerebrum are now also being included in the next generation of head models (e.g., [40]).

Chapters 3 to 5 are concerned with axonal injuries and how these are caused by higher level mechanical loads. First, several mechanical phenomena are investigated in Chapter 3 by developing a plane strain FE model that is a critical volume element (CVE), which relates tissue-level mechanics to axonal strains in a critical region for axonal injury. This model is based on the locations of axonal injury that were observed by Povlishock [15], corresponding to axons that deviate from their anatomical course due to the presence of an inclusion (e.g., a soma). In this thesis, it is assumed that these local axonal injuries are a consequence of axonal strain concentrations. Therefore, if local axonal stretching leads to injury, the maximum axonal strains in these critical regions are potentially a better predictor for injury than the maximum principal tissue strain, which is often used as an injury predictor. The mechanical phenomena that are investigated in Chapter 3 are the effects of the amount of curvature of the axons around the inclusion, the stiffness of the inclusion relative to the axons and the axonal and tissue-level as well as axonal-level effects caused by anisotropy. The main reason to vary these parameters is because the exact values of these parameters are not well-known. The results of the simulations show increased axonal strains at the same location, which indicates that axonal injury might be caused by locally larger deformations of the axons.

These strain concentrations occur due to the preferred orientation of axons through their oriented stretch directions and the resulting mechanical anisotropy. Furthermore, the presence of an inclusion with a different stiffness leads to a concentration of strain. As a consequence of these effects, the sensitivity of brain tissue to a mechanical load will anisotropically depend on the main axonal direction. The next step is the development of two different fully three-dimensional CVEs (i.e., with a spherical and a cylindrical inclusion) and an anisotropic equivalent strain measure that is documented in Chapter 4. It is shown that for predefined uniaxial and biaxial deformations in varying principal directions, the equivalent strain measure is able to produce a similar strain as obtained for the maximum axonal strains in the CVE simulations. The three-dimensional CVE and the anisotropic equivalent strain measure are two different tools to obtain local maximum axonal strains from simulations with an FE head model. Thereby, both approaches can be considered as an anisotropic criterion for injury, accounting for the orientation-dependent sensitivity of the tissue and are to be compared to an appropriate critical level of axonal strain. The CVE and the FE head model are coupled by means of a multi-scale approach, whereas the application of the equivalent strain measure to the head model is a single scale approach. Both approaches lead to a similar prediction of maximum axonal strains in a head model simulation based on an injurious load case, which means that the anisotropic equivalent strain measure is a proper alternative for the multi-scale simulations with the CVE, even for deformations that are not predefined as in Chapter 4. In Figure 6.1, the approach and the results of this thesis are summarized.

The modeling approach in this thesis, in particular the meso-level and the micro-level models, has been done such that the conclusions are generally valid. This is achieved by investigating the influence of varying the values of parameters that are not indisputably well-defined and by using relative measures. Nevertheless, the models are developed to represent the real physical problem in mind and are therefore expected to account for the most important aspects of injury at their respective length scale. The material behavior of brain tissue is an important assumption for the models, especially with the large variation in brain tissue properties in literature. The meso-level model and the FE head model in Chapter 3 use the isotropic non-linear viscoelastic material model developed by Hrapko et al. [48,49,57], which is obtained based on an extensive range of experiments.

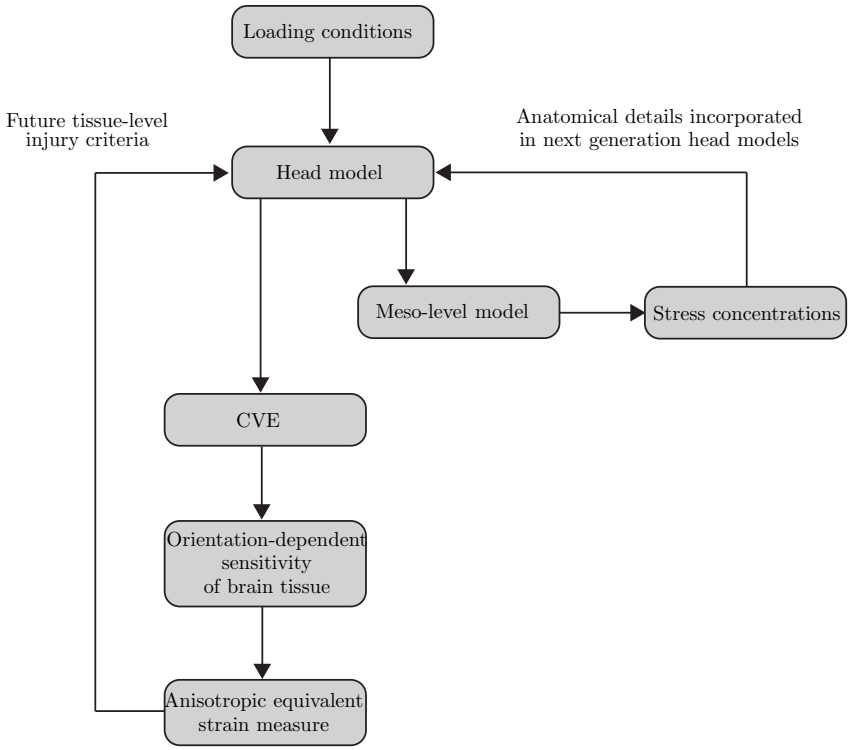

Figure 6.1: Schematic summary of the approach and the results of this study.

For the micro-level model, i.e., the CVE, anisotropic material behavior caused by neurofilaments was assumed to be important and therefore the Holzapfel-Gasser-Ogden fiber-reinforced anisotropic material model [132] is used. The material values are obtained from the study by Ning et al. [58], which contained only two successful test results. However, similar relative differences in shear moduli in different directions were obtained in other studies [51,52,57]. Since the density for critical regions for injury in the tissue, as described by the CVE, is assumed to be small, the local heterogeneities will not affect the overall tissue behavior. Therefore, the constitutive behavior of the axonal tissue in the CVE and the behavior of the tissue in the head model should be the same. Because the head model used for the multi-scale analysis was originally validated for injury in a

single scale analysis with isotropic viscoelastic brain tissue [37], the overall viscoelastic behavior used in the validated head model is maintained for the multi-scale analysis and anisotropy is added in the same ratio of stiffness in different direction as that reported in Ning et al. [58]. The same material behavior is adopted in the CVE in the multi-scale framework.

The geometries of the models describing the anatomy of the head and brain at different length scales are another important assumption in this thesis. At the macro level, two different FE head models are used. The head model used in Chapter 2 was developed by Claessens et al. [95] and later its geometry was refined by Brands et al. [41,158]. In Chapter 5, a different head model with an even more refined geometry is used that was developed by Kleiven [37,98]. However, compared to the anatomy of the brain these head models contain relatively coarse geometries. This might lead to the prediction of strains that are not true tissue strains, but the overall mechanical response is expected to be accurate enough for this study. Moreover, the loadings applied to the meso-level model and the CVE are not only based on the head model simulations, but also on stylized or predefined loading profiles. Therefore, the conclusions from these studies are relatively independent of the head models chosen. The geometries of the meso-level model are based on the anatomy of the cerebral cortex. Although they are relatively stylized, they are much more detailed than the head models used. It is assumed that the main features leading to local injuries at the bottom of the sulci are accounted for and that more refined geometries would not lead to different conclusions. Furthermore, from a mechanical viewpoint, a more refined geometry does not lead to improved conclusions if the heterogeneities of mechanical properties are not refined as well. This is also one of the main reasons why the CVEs contain different geometries with idealized inclusions. The second reason for the simple geometries of the CVEs is the assumption that the main cause of increased axonal strains is concerned with the orientation distribution of the axons relative to the principal loading direction and the anisotropic mechanical behavior. More realistic geometries will not lead to an overall different axonal orientation distribution and therefore not to different maximum axonal strains.

Despite the study on the different length scales of injury biomechanics of the brain in this thesis, predicting injury is still complicated. In order to translate the findings of this thesis into true injury mechanisms, more research

is necessary. The models can be a starting point for other researchers, carefully reconsidering the modeling assumptions if new information becomes available. The most important outcome of this thesis for other researcher to use is expected to be the anisotropic equivalent strain measure, because it is a practical tool to account for the microstructural effects in a single scale head model simulation and in combination with a critical level of axonal strain forms a criterion for injury. Furthermore, tissue-level experiments could be used to characterize the parameters of this generally formulated anisotropic criterion for injury, in which case the underlying microstructural effects do not need to be known.

6.2 Recommendations

The aim of this study was to relate the different length scales concerning TBI, which has been achieved. For using or improving the findings of this study, some recommendation are given:

- Depending on the region of interest with respect to local brain injury, the meso-level heterogeneities should be accounted for, e.g., by including these details in the geometry of the FE head model [40].
- If the region of interest for injury is sufficiently far away from the cerebral cortex, FE head models with less geometrical detail will probably suffice for using the CVE or the anisotropic equivalent strain measure. Importantly, the orientation of the axons and the anisotropy should be accounted for in the FE head model.
- Diffusion tensor imaging (DTI), which is used to visualize the orientation and degree of alignment of axons, is a promising technique to implement axonal orientation in FE head models. To account for the mechanical consequences of this orientation, the outcome of diffusion tensor measurements, including the main orientation and the amount of dispersion, should be related to mechanical anisotropy.
- The predictive capabilities of new anisotropic head models using the CVE or the anisotropic equivalent strain measure as an injury criterion should be validated. This can be done by using documentation

based on accident reconstructions containing detailed information on the loading conditions and the clinical observations.

- When more information becomes available about the micromechanical aspects of axonal injury, improved CVEs can be made for a more accurate understanding of local axonal injury. Some of the aspects that can be investigated are the interface condition between the axons and the inclusion. Also, a more realistic microstructure can be adopted, including the local heterogeneities of the mechanical properties. The current CVE is modeled with locally fully aligned axons or with a fully isotropic orientation of axons (see Chapter 3). However, if the degree of axonal alignment has an intermediate value, more modeling assumptions need to be made for a proper implementation in the CVE.

- For a better understanding of the relation between the mechanical load and the physiological events of axonal injury, an even lower length scale that accounts for damage of the network of neurofilaments probably has to be modeled.

- Further characterization of the anisotropic equivalent strain measure can be done by at least two different approaches: 1) fitting the coefficients to a further improved CVE, or 2) fitting the coefficients to the stretch levels that are critical for injury in different stretch directions obtained from tissue-level experiments, thereby allowing it to be used directly as an anisotropic criterion for injury.

Appendix A

Finite element implementation

In Section A.1, the constitutive model for brain tissue that is used in Chapter 2 is explained. This model is based on the incompressible constitutive model developed by Hrapko et al. [49] for porcine white matter. For the model in Chapter 2, compressibility is added. The numerical implementation of the constitutive model is explained in Section A.2.

A.1 Constitutive model of brain tissue

The constitutive model consists of an elastic part, denoted by subscript e, and of a (deviatoric) viscoelastic part, denoted by subscript ve, with N viscoelastic modes. The total Cauchy stress tensor $\boldsymbol{\sigma}$ is written as

$$\boldsymbol{\sigma} = \boldsymbol{\sigma}_e^h + \boldsymbol{\sigma}_e^d + \sum_{i=1}^{N} \boldsymbol{\sigma}_{ve_i}^d, \tag{A.1}$$

in which superscripts h and d denote the hydrostatic and the deviatoric part, respectively. The hydrostatic part of Equation A.1 is defined as

$$\boldsymbol{\sigma}_e^h = K(J-1)\boldsymbol{I}, \tag{A.2}$$

where K is the bulk modulus and $J = \sqrt{I_3} = \det(\boldsymbol{F})$ is the change in volume and I_3 is the third invariant of the Finger tensor $\boldsymbol{B}$.

The deviatoric part of Equation A.1 is represented schematically in Figure A.1. It shows the deviatoric elastic stress mode ($\boldsymbol{\sigma}_e^d$) and the viscoelastic stress modes ($\boldsymbol{\sigma}_{ve_i}^d$) with $i = 1$ to N. The deviatoric elastic mode describes a non-linear response to the deformation $\boldsymbol{F}$, which is given by

$$\boldsymbol{\sigma}_e^d = \frac{G_\infty}{\sqrt{I_3}} \left[(1-A)\exp\left(-C\sqrt{b\tilde{I}_1 + (1-b)\tilde{I}_2 - 3} \right) + A \right] \left[b\tilde{\boldsymbol{B}}^d - (1-b)(\tilde{\boldsymbol{B}}^{-1})^d \right], \tag{A.3}$$

where G_∞ is the elastic shear modulus, I_3 is the third invariant of the Finger tensor $\boldsymbol{B}$, $\tilde{\boldsymbol{B}} = J^{-\frac{2}{3}}\boldsymbol{B}$ is the isochoric part of the Finger tensor $\boldsymbol{B}$, and $\tilde{I}_1$ and $\tilde{I}_2$ are the first and second invariant of the isochoric Finger tensor $\tilde{\boldsymbol{B}}$, respectively. A, C, and b are elastic fitting parameters.

The third term on the right hand side of Equation A.1 consists of the summation of the viscoelastic modes. The mechanical energy that initially is stored as elastic energy in a viscoelastic material dissipates in time. This means that for the current state, the mechanical energy is partly stored as elastic energy and partly dissipated as heat. Therefore, the deformation gradient tensor $\boldsymbol{F}_i$ is partitioned into an elastic deformation gradient tensor $\boldsymbol{F}_{e_i}$ and a viscous deformation gradient tensor $\boldsymbol{F}_{v_i}$ [106,107]. The partitioning of the viscoelastic deformations is depicted in Figure A.2. For simplicity, the subscript i indicating the viscoelastic mode i is omitted throughout the remaining part of this section. A multiplicative decomposition of the

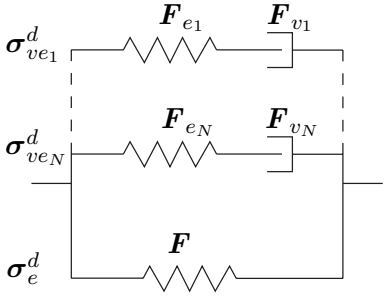

Figure A.1: Schematic representation of the deviatoric part of the constitutive model for brain tissue with elastic deformation $\boldsymbol{F}_e$ and $\boldsymbol{F}$ and viscous deformation $\boldsymbol{F}_v$.

deformation gradient tensor $\boldsymbol{F}$ is assumed:

$$\boldsymbol{F} = \boldsymbol{F}_e \cdot \boldsymbol{F}_v. \tag{A.4}$$

The decomposition involves a fictitious intermediate state, which could exist after application of merely the viscous deformation gradient tensor $\boldsymbol{F}_v$ (Figure A.2). This is the stress-free state, which after application of the elastic deformation tensor $\boldsymbol{F}_e$ transforms into the final state.

By using Equation A.4 with the velocity gradient tensor $\boldsymbol{L} = \dot{\boldsymbol{F}} \cdot \boldsymbol{F}^{-1}$, it follows that

$$\boldsymbol{L} = \boldsymbol{L}_e + \boldsymbol{L}_v, \tag{A.5}$$

with

$$\boldsymbol{L}_e = \dot{\boldsymbol{F}}_e \cdot \boldsymbol{F}_e^{-1} \tag{A.6}$$

$$\boldsymbol{L}_v = \boldsymbol{F}_e \cdot \dot{\boldsymbol{F}}_v \cdot \boldsymbol{F}_v^{-1} \cdot \boldsymbol{F}_e^{-1}. \tag{A.7}$$

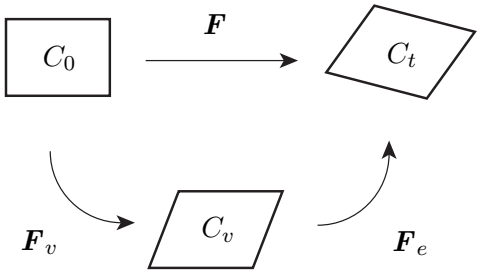

Figure A.2: Partitioning of the deformation gradient tensor $\boldsymbol{F}$ into an elastic deformation gradient tensor $\boldsymbol{F}_e$ and a viscous deformation gradient tensor $\boldsymbol{F}_v$ in order to obtain a fictitious stress-free state C_v between the initial configuration C_0 and the current configuration C_t.

The velocity gradient tensor $\boldsymbol{L}$ can also be decomposed as

$$\begin{aligned} \boldsymbol{L} &= \boldsymbol{D} + \boldsymbol{\Omega}, && \text{(A.8)} \\ \boldsymbol{L}_e &= \boldsymbol{D}_e + \boldsymbol{\Omega}_e, && \text{(A.9)} \\ \boldsymbol{L}_v &= \boldsymbol{D}_v + \boldsymbol{\Omega}_v, && \text{(A.10)} \end{aligned}$$

in which $\boldsymbol{D} = \frac{1}{2}(\boldsymbol{L} + \boldsymbol{L}^T)$ is the symmetric rate of deformation tensor and $\boldsymbol{\Omega} = \frac{1}{2}(\boldsymbol{L} - \boldsymbol{L}^T)$ the skew-symmetric spin tensor. However, this does not provide a unique intermediate state, as rigid-body rotation can be assigned to both $\boldsymbol{F}_e$ and $\boldsymbol{F}_v$. To obtain a unique intermediate state, the viscous deformations are chosen to be spin-free. This assumption means that $\boldsymbol{\Omega}_v = \boldsymbol{0}$.

Furthermore, the viscous right Cauchy-Green deformation tensor is defined as

$$\boldsymbol{C}_v = \boldsymbol{F}_v^T \cdot \boldsymbol{F}_v. \tag{A.11}$$

In order to update the tensor $\boldsymbol{C}_v$ in the time integration scheme, which is described in Section A.2, use is made of its time derivative:

$$\dot{\boldsymbol{C}}_v = \boldsymbol{F}_v^T \cdot \dot{\boldsymbol{F}}_v + \dot{\boldsymbol{F}}_v^T \cdot \boldsymbol{F}_v. \tag{A.12}$$

By using Equations A.5 to A.7, Equation A.12 can be rewritten into

$$\dot{\boldsymbol{C}}_v = \boldsymbol{F}^T \cdot \boldsymbol{B}_e^{-1} \cdot [(\boldsymbol{L} - \boldsymbol{L}_e) \cdot \boldsymbol{B}_e + \boldsymbol{B}_e \cdot (\boldsymbol{L}^T - \boldsymbol{L}_e^T)] \cdot \boldsymbol{B}_e^{-1} \cdot \boldsymbol{F}. \tag{A.13}$$

Using the assumption of a spin-free viscous deformation, the time derivative of the viscous right Cauchy-Green deformation tensor for a unique intermediate state yields

$$\dot{\boldsymbol{C}}_v = 2 \cdot \boldsymbol{F}^T \cdot \boldsymbol{B}_e^{-1} \cdot \boldsymbol{D}_v \cdot \boldsymbol{F}. \tag{A.14}$$

The elastic Finger tensor is calculated by

$$\boldsymbol{B}_e = \boldsymbol{F} \cdot \boldsymbol{C}_v^{-1} \cdot \boldsymbol{F}^T. \tag{A.15}$$

The third term on the right hand side of Equation A.1 describes the vis-

coelastic contribution to the stress as follows:

$$\boldsymbol{\sigma}_{ve}^{d} = \frac{G}{\sqrt{I_3}} \left[a\tilde{\boldsymbol{B}}_{e}^{d} - (1-a)(\tilde{\boldsymbol{B}}_{e}^{-1})^{d} \right], \tag{A.16}$$

with G the shear modulus, I_3 the third invariant of the Finger tensor $\boldsymbol{B}$, $\tilde{\boldsymbol{B}}_e$ the isochoric part of the elastic Finger tensor $\boldsymbol{B}_e$, and a a viscoelastic fitting parameter. The viscous deformation $\boldsymbol{F}_v$ is assumed to be volume-invariant, so that $\det(\boldsymbol{F}_v) = 1$ and $J_e = \det(\boldsymbol{F}_e) = J$. This justifies the use of the third invariant of $\boldsymbol{B}$ instead of $\boldsymbol{B}_e$ in Equation A.16.

The viscous rate of deformation tensor, is calculated from the flow rule, assuming incompressibility, as

$$\boldsymbol{D}_v = \frac{\boldsymbol{\sigma}_{ve}^{d}}{2\eta(\tau)}, \tag{A.17}$$

where the dynamic viscosity η is a function of the scalar equivalent stress measure $\tau = \sqrt{\frac{1}{2}\boldsymbol{\sigma}^d : \boldsymbol{\sigma}^d}$. It is described by the Ellis model, which states

$$\eta(\tau) = \eta_\infty + \frac{\eta_0 - \eta_\infty}{1 + \left(\frac{\tau}{\tau_0}\right)^{(n-1)}}, \tag{A.18}$$

with subscripts 0 and ∞ denoting the initial and infinite values, respectively. The initial value for viscosity is defined as $\eta_0 = G\lambda$, whereas the infinite viscosity is defined as $\eta_\infty = k\eta_0$.

A.2 Numerical implementation

For the numerical implementation of the stress computation of Equation A.1, several steps have to be taken for each time t. The elastic stresses $\boldsymbol{\sigma}_e^h(t)$ (Step 2) and $\boldsymbol{\sigma}_e^d(t)$ (Step 3) can be computed directly. For the time integration of the viscoelastic stress computation (Step 4), the Heun's method, also known as the improved Euler's method, is used [41]. This involves an explicit time integration scheme for Equation A.14. First, a prediction (indicated by $\bar{}$) of the derivative of the viscous right Cauchy-Green deformation tensor $\bar{\boldsymbol{C}}_{v_i}(t)$ is computed in Step 4b by using the original Euler

forward method. This is used to calculate $\bar{\dot{\boldsymbol{C}}}_{v_i}(t)$ and $\bar{\boldsymbol{\sigma}}^d_{ve_i}(t)$. After that, $\boldsymbol{C}_{v_i}(t)$ is more accurately determined in Step 4d by applying the trapezoidal rule, after which $\dot{\boldsymbol{C}}_{v_i}(t)$ and $\boldsymbol{\sigma}^d_{ve_i}(t)$ are calculated. For each time step, the values of tensors $\boldsymbol{C}_{v_i}(t)$, $\dot{\boldsymbol{C}}_{v_i}(t)$, and $\boldsymbol{\sigma}^d_{ve_i}(t)$ are stored for the next time increment. For the initial values, no deformation is assumed, which yields $\boldsymbol{F}(0) = \boldsymbol{I}$, $\boldsymbol{C}_{v_i}(0) = \boldsymbol{I}$, $\dot{\boldsymbol{C}}_{v_i}(0) = \boldsymbol{0}$, and $\boldsymbol{\sigma}^d_{ve_i} = \boldsymbol{0}$. The steps for the numerical implementation are as follows:

1. Compute the deformation $\boldsymbol{F}$(t) from the nodal displacements.
2. Compute $\boldsymbol{\sigma}^h_e(t) = K(J(t) - 1)\boldsymbol{I}$.
3. Compute $\boldsymbol{\sigma}^d_e(t) =$
   $\frac{G_\infty}{\sqrt{\tilde{I}_3(t)}} \left[(1 - A)\exp\left(-C\sqrt{b\tilde{I}_1 + (1 - b)\tilde{I}_2 - 3}\right) + A\right]$
   $\left[b\tilde{\boldsymbol{B}}^d(t) - (1 - b)(\tilde{\boldsymbol{B}}^{-1})^d(t)\right]$.
4. (a) Retrieve $\boldsymbol{C}_{v_i}(t - dt)$ and $\dot{\boldsymbol{C}}_{v_i}(t - dt)$ from the previous time increment for each mode $i = 1$ to N.

   (b) For mode $i = 1$ to N, predict $\boldsymbol{C}_{v_i}(t)$, $\boldsymbol{B}_{e_i}(t)$, and $\boldsymbol{\sigma}^d_{ve_i}(t)$:

   $$\bar{\boldsymbol{C}}_{v_i}(t) = \boldsymbol{C}_{v_i}(t - dt) + \dot{\boldsymbol{C}}_{v_i}(t - dt)dt,$$

   $$\bar{\boldsymbol{B}}_{e_i}(t) = \boldsymbol{F}(t) \cdot \bar{\boldsymbol{C}}^{-1}_{v_i}(t) \cdot \boldsymbol{F}^T(t),$$

   $$\bar{\boldsymbol{\sigma}}^d_{ve_i}(t) = \frac{G_i}{\sqrt{\tilde{I}_3(t)}} \left[a\bar{\tilde{\boldsymbol{B}}}^d_{e_i}(t) - (1 - a)(\bar{\tilde{\boldsymbol{B}}}^{-1}_{e_i})^d(t)\right].$$

   (c) Predict $\boldsymbol{\sigma}^d(t)$ and $\tau(t)$:

   $$\bar{\boldsymbol{\sigma}}^d(t) = \boldsymbol{\sigma}^d_e(t) + \textstyle\sum_{i=1}^N \bar{\boldsymbol{\sigma}}^d_{ve_i}(t),$$

   $$\bar{\tau}(t) = \sqrt{\bar{\boldsymbol{\sigma}}^d(t) : \bar{\boldsymbol{\sigma}}^d(t)}.$$

   (d) For mode $i = 1$ to N, predict $\eta_i(t)$, $\boldsymbol{D}_{v_i}(t)$, and $\dot{\boldsymbol{C}}_{v_i}(t)$:

$$\bar{\eta}_i(t) = \eta_{\infty_i} + \frac{\eta_{0_i} - \eta_{\infty_i}}{1 + \left(\frac{\bar{\tau}(t)}{\tau_0}\right)^{(n_i - 1)}},$$

$$\bar{\boldsymbol{D}}_{v_i}(t) = \frac{\bar{\boldsymbol{\sigma}}^d_{ve_i}(t)}{2\bar{\eta}_i(t)},$$

$$\bar{\dot{\boldsymbol{C}}}_{v_i}(t) = 2 \cdot \boldsymbol{F}^T(t) \cdot \bar{\boldsymbol{B}}^{-1}_{e_i}(t) \cdot \bar{\boldsymbol{D}}_{v_i}(t) \cdot \boldsymbol{F}(t),$$

determine $\boldsymbol{C}_{v_i}(t)$, $\boldsymbol{B}_{e_i}(t)$ and $\boldsymbol{\sigma}^d_{ve_i}(t)$:

$$\boldsymbol{C}_{v_i}(t) = \boldsymbol{C}_{v_i}(t - dt) + \tfrac{1}{2}(\dot{\boldsymbol{C}}_{v_i}(t - dt) + \bar{\dot{\boldsymbol{C}}}_{v_i}(t))dt,$$

$$\boldsymbol{B}_{e_i}(t) = \boldsymbol{F}(t) \cdot \boldsymbol{C}^{-1}_{v_i}(t) \cdot \boldsymbol{F}^T(t),$$

$$\boldsymbol{\sigma}^d_{ve_i}(t) = \frac{G_i}{\sqrt{I_3(t)}} \left[a\tilde{\boldsymbol{B}}^d_{e_i}(t) - (1 - a)(\tilde{\boldsymbol{B}}^{-1}_{e_i})^d(t) \right],$$

and store $\boldsymbol{C}_{v_i}(t)$ for the next time increment.

(e) Determine $\boldsymbol{\sigma}^d(t)$ and $\tau(t)$:

$$\boldsymbol{\sigma}^d(t) = \boldsymbol{\sigma}^d_e(t) + \textstyle\sum_{i=1}^N \boldsymbol{\sigma}^d_{ve_i}(t),$$

$$\tau(t) = \sqrt{\boldsymbol{\sigma}^d(t) : \boldsymbol{\sigma}^d(t)}.$$

(f) For mode $i = 1$ to N, determine $\eta_i(t)$, $\boldsymbol{D}_{v_i}(t)$ and $\dot{\boldsymbol{C}}_{v_i}(t)$:

$$\eta_i(t) = \eta_{\infty_i} + \frac{\eta_{0_i} - \eta_{\infty_i}}{1 + \left(\frac{\tau(t)}{\tau_0}\right)^{(n_i - 1)}},$$

$$\boldsymbol{D}_{v_i}(t) = \frac{\boldsymbol{\sigma}^d_{ve_i}(t)}{2\eta_i(t)},$$

$$\dot{\boldsymbol{C}}_{v_i}(t) = 2 \cdot \boldsymbol{F}^T(t) \cdot \boldsymbol{B}^{-1}_{e_i}(t) \cdot \boldsymbol{D}_{v_i}(t) \cdot \boldsymbol{F}(t),$$

and store $\dot{\boldsymbol{C}}_{v_i}(t)$ for the next time increment.

5. Compute $\boldsymbol{\sigma}(t) = \boldsymbol{\sigma}^h_e(t) + \boldsymbol{\sigma}^d(t)$.

Bibliography

[1] C. Brooks, B. Gabella, R. Hoffman, D. Sosin, and G. Whiteneck. Traumatic brain injury: designing and implementing a population-based follow-up system. *Arch Phys Med Rehabil*, 78:S26–S30, 1997.

[2] R. Waxweiler, D. Thurman, J. Sniezek, D. Sosin, and J. O'Neil. Monitoring the impact of traumatic brain injury: a review and update. *J Neurotrauma*, 12:509–516, 1995.

[3] ETSC. *Exposure data for travel risk assessment*. European Transport Safety Council, Brussels, Belgium, 1999.

[4] B. Jennett. Epidemiology of head injury. *J Neurol Neurosurg Psychiatry*, 60:362–369, 1996.

[5] J.E. Bailes. Head injuries in sports. In B.D. Jordan, P. Tsairis, and R.F. Warren, editors, *Sports Neurology*, pages 215–233. Lippincott-Raven, Philadelphia, PA, 2nd edition, 1998.

[6] M.W. Collins, S.H. Grindel, M.R. Lovell, D.E. Dede, D.J. Moser, and B.R. Phalin. Relationship between concussion and neuropsychological performance in college football players. *JAMA*, 282:964–970, 1999.

[7] J.T. Matser, A.G.H. Kessels, B.D. Jordan, M.D. Lezak, and J. Troost. Chronic traumatic brain injury in professional soccer players. *Neurology*, 51:791–796, 1998.

[8] E.J.T. Matser, A.G.H. Kessels, M.D. Lezak, B.D. Jordan, and J. Troost. Neuropsychological impairment in amateur soccer players. *JAMA*, 282:971–973, 1999.

[9] J.T. Matser, A.G.H. Kessels, M.D. Lezak, and J. Troost. A dose-response relation of headers and concussions with congnitive impairment in professional soccer players. *J Clin Exp Neuropsychol*, 23:770–774, 2001.

[10] J.W. Powell and K.D. Barber-Foss. Traumatic brain injury in high schools athletes. *JAMA*, 282:958–963, 1999.

[11] S.N. Macciocchi, D.B. Reid, and J.T. Barth. Disability following head injury. *Curr Opin Neurol*, 6:773–777, 1993.

[12] T.W. McAllister. Neuropsychiatric sequelae of head injuries. *Psychiatr Clin North Am*, 15:395–413, 1992.

[13] J. Adams, D. Doyle, I. Ford, T. Gennarelli, D. Graham, and D. McClellan. Diffuse axonal injury in head injury: definition, diagnosis, and grading. *Histopathology*, 15:49–59, 1989.

[14] D. Graham, J. Adams, and T. Gennarelli. Mechanisms of non-penetrating head injury. *Prog Clin Biol Res*, 234:159–168, 1988.

[15] J.T. Povlishock. Traumatically induced axonal injury: pathogenesis and pathobiological implications. *Brain Pathol*, 2:1–12, 1992.

[16] J. Adams, D. Doyle, and D. Graham. Diffuse axonal injury in head injuries caused by a fall. *Lancet*, 2:1420–1422, 1984.

[17] T. Gennarelli. Mechanisms of brain injury. *J Emerg Med*, 11:5–11, 1993.

[18] M. Grady, M. McLaughlin, C. Christman, A. Valadka, C. Fligner, and J. Povlishock. The use of antibodies targeted against the neurofilament subunits for the detection of diffuse axonal injury in humans. *J Neuropathol Exp Neurol*, 52:143–152, 1993.

[19] B. Morrison III, K. Saatman, D. Meaney, and T. McIntosh. In vitro central nervous system models of mechanically induced trauma: a review. *J Neurotrauma*, 15:911–928, 1998.

[20] L. Thibault, T. Gennarelli, S. Margulies, J. Marcus, and R. Eppinger. The strain dependent pathophysiological consequences of inertial loading on central nervous system tissue. In *Proceedings of the IRCOBI conference*, 1990.

[21] E.N. Marieb. *Human anatomy and physiology.* Benjamin/Cummings Science Publishing, Menlo Park, CA, USA, 4th edition, 1998.

[22] J. Nolte. *The human brain: an introduction to its functional anatomy.* Mosby, Inc., St. Louis, MO, USA, 5th edition, 2002.

[23] The American Society of Clinical Oncology. http://www.asco.org, 2008.

[24] M. Hrapko. *Mechanical behavior of brain tissue for injury prediction: characterization and modeling.* PhD thesis, Eindhoven University of Technology, 2008.

[25] A.C. Guyton and J.E. Hall. *Textbook of medical physiology.* W.B. Saunders Co., Philadelphia, PA, USA, 10th edition, 2000.

[26] N.R. Saunders, M.D. Habgood, and K.M. Dziegielewska. Barrier mechanisms in the brain, I. adult brain. *Clin Exp Pharmacol Physiol*, 26:11–19, 1999.

[27] W. Goldsmith. The state of head injury biomechanics: past, present, and future: part 1. *Crit Rev Biomed Eng*, 29:441–600, 2001.

[28] A.E. Davis. Mechanisms of traumatic brain injury: biomechanical, structural and cellular considerations. *Crit Care Nurs Q*, 23(3):1–13, 2000.

[29] J.M. Meythaler, J.D. Peduzzi, E. Eleftheriou, and T.A. Novack. Current concepts: diffuse axonal injury-associated traumatic brain injury. *Arch Phys Med Rehabil*, 82:1461–1471, 2001.

[30] E. Gutierrez, K. Haglid Y. Huang, F. Bao, H. Hansson, A. Hamberger, and D. Viano. A new model for diffuse brain injury by rotational acceleration: I model, gross appearance, and astrocytosis. *J Neurotrauma*, 18(3):247–257, 2001.

[31] C.S. Cotter, P.K. Smolarkiewicz, and I.N. Szczyrba. A viscoelastic fluid model for brain injuries. *Int J Numer Meth Fluids*, 40:303–311, 2002.

[32] NHTSA. *Occupant crash protection - head injury criterion, S6.2 of FMVSS 571.208*. NHTSA, Washington, DC, 1972.

[33] S.S. Margulies, L.E. Thibault, and T.A. Gennarelli. Physical model simulations of brain injury in the primate. *J Biomech*, 17:162–170, 1998.

[34] J. Ivarsson, D.C. Viano, P. Lövsund, and B. Aldman. Strain relief from the cerebral ventricles during head impact: experimental studies on natural protection of the brain. *J Biomech*, 33:181–189, 2000.

[35] J. Ivarsson, D.C. Viano, and P. Lövsund. Influence of the lateral ventricles and irregular skull base on brain kinematics due to sagittal plane head rotation. *J Biomech Eng*, 124:442–431, 2002.

[36] L. Zhang, K.H. Yang, and A.I. King. A proposed injury threshold for mild traumatic brain injury. *J Biomech Eng*, 126:226–236, 2004.

[37] S. Kleiven. Predictors for traumatic brain injuries evaluated through accident reconstruction. *Stapp Car Crash J*, 51:81–114, 2007.

[38] D. Marjoux, D. Baumgartner, C. Deck, and R. Willinger. Head injury prediction of the HIC, HIP, SIMon and ULP criteria. *Accident Anal Prev*, 40:1135–1148, 2008.

[39] M. Hrapko, J.A.W. van Dommelen, G.W.M. Peters, and J.S.H.M. Wismans. On the consequences of non linear constitutive modelling of brain tissue for injury prediction with numerical head models. *Int J Crashworthiness*, 14:245–257, 2009.

[40] J. Ho, H. von Holst, and S. Kleiven. An automatic method to generate a patient specific finite element head model. *Int J Crashworthines*, 14:555–563, 2009.

[41] D.W.A. Brands, P.H.M. Bovendeerd, and J.S.H.M. Wismans. On the potential importance of non-linear viscoelastic material modelling for

numerical prediction of brain tissue response: test and application. *Stapp Car Crash J*, 46, 2002.

[42] R. Willinger, H. Kang, and B. Diaw. Three-dimensional human head finite-element model validation against two experimental impacts. *Ann Biomed Eng*, 27:403–410, 1999.

[43] J.S. Raul, D. Baumgartner, R. Willinger, and B. Ludes. Finite element modelling of human head injuries caused by a fall. *Int J Leg Med*, 2005.

[44] C. Zhou, T.B. Khalil, and A.I. King. A new model comparing impact responses of homogeneous and inhomogeneous human brain. In *Stapp Car Crash Conference Proceedings*, volume 39. The Stapp Association, 1995.

[45] A.S. Al-Bsharat, W.N. Hardy, K.H. Yang, T.B. Khalil, S. Tashman, and A.I. King. Brain/skull relative displacement magnitude due to blunt head impact: new experimental data and model. In *Stapp Car Crash Conference Proceedings*, volume 43. The Stapp Association, 1999.

[46] B. Fischl and A.M. Dale. Measuring the thickness of the human cerebral cortex from magnetic resonance images. *Proc Natl Acad Sci*, 97:11050–11055, 2000.

[47] D.R.S. Bradshaw, J. Ivarsson, C.L. Morfey, and D.C. Viano. Simulation of acute subdural hematoma and diffuse axonal injury in coronal head impact. *J Biomech*, 34:85–94, 2001.

[48] M. Hrapko, J.A.W. van Dommelen, G.W.M. Peters, and J.S.H.M. Wismans. The influence of test conditions on characterization of the mechanical properties of brain tissue. *J Biomech Eng*, 130:031003, 2008.

[49] M. Hrapko, J.A.W. van Dommelen, G.W.M. Peters, and J.S.H.M. Wismans. The mechanical behaviour of brain tissue: large strain response and constitutive modelling. *Biorheology*, 43(5):623–636, 2006.

[50] F. Shen, T.E. Tay, J.Z. Li, S. Nigen, P.V.S. Lee, and H.K. Chan. Modified bilston nonlinear viscoelastic model for finite element head injury studies. *J Biomech Eng*, 125:797–801, 2006.

[51] M.T. Prange and S.S. Margulies. Regional, directional, and age-dependent properties of the brain undergoing large deformation. *J Biomech Eng*, 124:244–252, 2002.

[52] K.B. Arbogast and S.S. Margulies. Material characterization of the brainstem from oscillatory shear tests. *J Biomech*, 31:801–807, 1998.

[53] B.S. Elkin, E.U. Azeloglu, K.D. Costa, and B. Morrison III. Mechanical heterogeneity of the rat hippocampus measured by atomic force microscope indentation. *J Neurotrauma*, 24:812–822, 2007.

[54] B.S. Elkin, A. Ilankova, and B. Morrison III. Age-dependent regional mechanical properties of the rat hippocampus and cortex. *J Biomech Eng*, 132:011010, 2010.

[55] B.S. Elkin, A. Ilankova, and B. Morrison III. Dynamic, regional mechanical properties of the porcine brain: Indentation in the coronal plane. *J Biomech Eng*, 133:071009, 2011.

[56] B.S. Elkin, A.I. Ilankova, and B. Morrison III. A detailed viscoelastic characterization of the p17 and adult rat brain. *J Neurotrauma*, 28:(in press), 2011.

[57] M. Hrapko, H. Gervaise, J.A.W. van Dommelen, G.W.M. Peters, and J.S.H.M. Wismans. Identifying the mechanical behaviour of brain tissue in both shear and compression. In *Proceedings of the IRCOBI conference*, 2007.

[58] X. Ning, Q. Zhu, Y. Lanir, and S.S. Margulies. A transversely isotropic viscoelastic constitutive equation for brainstem undergoing finite deformation. *J Biomech Eng*, 128:925–933, 2006.

[59] A.C. Bain and D.F. Meaney. Tissue-level thresholds for axonal damage in an experimental model of central nervous system white matter injury. *J Biomech Eng*, 122:615–622, 2000.

[60] A.C. Bain, R. Raghupathi, and D.F. Meaney. Dynamic stretch correlates to both morphological abnormalities and electrophysiological impairment in a model of traumatical axonal injury. *J Neurotrauma*, 18:499–511, 2001.

[61] B. Morrison III, H.L. Cater, C.C. Wang, F.C. Thomas, C.T. Hung, G.A. Ateshian, and L.E. Sundstrom. A tissue level tolerance criterion fo living brain developed with an in vitro model of traumatic mechanical loading. *Stapp Car Crash J*, 47, 2003.

[62] B. Morrison III, H.L. Cater, C.D. Benham, and L.E. Sundstrom. An in vitro model of traumatic brain injury utilising two-dimensional stretch of organotypic hippocampal slice cultures. *J Neurosci Meth*, 150:192–201, 2006.

[63] H.L. Cater, L.E. Sundstrom, and B. Morrison III. Temporal development of hippocampal cell death is dependent on tissue strain but not strain rate. *J Biomech*, 39:2810–2818, 2006.

[64] S. Chatelin, C. Deck, F. Renard, S. Kremer, C. Heinrich, J.-P. Armspach, and R. Willinger. Computation of axonal elongation in head trauma finite element simulation. *J Mech Behav Biomed*, (in press), 2011.

[65] N. C. Colgan, M. D. Gilchrist, and K. M. Curran. Applying DTI white matter orientations to finite element head models to examine diffuse TBI under high rotational accelerations. *Prog Biophys Mol Biol*, 103:304–309, 2010.

[66] R.M. Wright and K.T. Ramesh. An axonal strain injury criterion for traumatic brain injury. *Biomech Model Mechanobiol*, (in press), 2011.

[67] G. Rajkowska and P. S. Goldman-Rakic. Cytoarchitectonic definition of prefrontal areas in the normal human cortex: I. remapping of areas 9 and 46 using quantitative criteria. *Cereb Cortex*, 5:307–322, 1995.

[68] G. Rajkowska, L.D. Selemon, and P.S. Goldman-Rakic. Neuronal and glial somal size in the prefrontal cortex. *Arch Gen Psychiatry*, 55:215–224, 1998.

[69] J.N. Pierri, C.L.E. Volk, S. Auh, A. Sampson, and D.A. Lewis. Decreased somal size of deep layer 3 pyramidal neurons in the prefrontal cortex of subjects with schizophrenia. *Arch Gen Psychiatry*, 58:466–473, 2001.

[70] D. Cotter, D. Mackay, G. Chana, C. Beasley, S. Landau, and I. P. Everall. Reduced neuronal size and glial cell density in area 9 of the dorsolateral prefrontal cortex in subjects with major depressive disorder. *Cereb Cortex*, 12:386–394, 2002.

[71] J.R. Highley, M.A. Walker, B. McDonald, T.J. Crow, and M.M. Esiri. Size of hippocampal pyramidal neurons in schizophrenia. *Brit J Psychiat*, 183:414–417, 2003.

[72] J.J. Hutsler. The specialized structure of human language cortex: Pyramidal cell size asymmetries within auditory and language-associated regions of the temporal lobes. *Brain Lang*, 86:226–242, 2003.

[73] B. Alberts, D. Bray, J. Lewis, M. Raff, K. Roberts, and J.D. Watson. *Molecular biology of the cell*. Garland Publishing, New York, NY, 3th edition, 1994.

[74] P.D. Coleman, J. Romano, L. Lapham, and W. Simon. Cell counts in cerebral cortex of an autistic patient. *J Autism Dev Disord*, 15:245–255, 1985.

[75] L.D. Selemon, G. Rajkowska, and P.S. Goldman-Rakic. Elevated neuronal density in prefrontal area 46 in brains from schizophrenic patients: Application of a three-dimensional, stereologic counting method. *J Comp Neurol*, 392:402–412, 1998.

[76] C.C. Sherwood, C.D. Stimpson, M.A. Raghanti, D.E. Wildman, M. Uddin, L.I. Grossman, M. Goodman, J.C. Redmond, C.J. Bonar, J.M. Erwin, and P.R. Hof. Evolution of increased glia-neuron ratios in the human frontal cortex. *Proc Natl Acad Sci*, 103:13606–13611, 2006.

[77] K. A. Barbee. Mechanical cell injury. *Ann NY Acad Sci*, 1066:67–84, 2005.

[78] D.M. Geddes-Klein, K.B. Schiffman, and D.F. Meaney. Mechanisms and consequences of neuronal stretch injury in vitro differ with the model of trauma. *J Neurotrauma*, 23:193–204, 2006.

[79] C.L. Floyd, F.A. Gorin, and B.G. Lyeth. Mechanical strain injury increases intracellular sodium and reverses na^{+}/ca^{2+} exchange in cortical astrocytes. *Glia*, 51:35–46, 2005.

[80] D.H. Smith, J.A. Wolf, T.A. Lusardi, V.M.-Y. Lee, and D.F. Meaney. High tolerance and delayed elastic response of cultured axons to dynamic stretch injury. *J Neurosci*, 19:4263–4269, 1999.

[81] T.A. Lusardi, J.A. Wolf, M.E. Putt, D.H. Smith, and D.F. Meaney. Effect of acute calcium influx after mechanical stretch injury in vitro on the viability of hippocampal neurons. *J Neurotrauma*, 21:61–72, 2004.

[82] A. Singh, Y. Lu, C. Chen, S. Kallakuri, and J.M. Cavanaugh. A new model of traumatic axonal injury to determine the effects of strain and displacement rates. *Stapp Car Crash J*, 50, 2006.

[83] Y. Lu, K. Franze, G. Seifert, C. Steinhäuser, F. Kirchhoff, H. Wolburg, J. Guck, P. Jammey, E.-Q. Wei, J. Käs, and A. Reisenbach. Viscoelastic properties of individual glial cells and neurons in the CNS. *Proc Natl Acad Sci*, 103:17759–17764, 2006.

[84] A. Heredia, C.C. Bui, U. Suter, P. Young, and T.E. Schäffer. AFM combines functional and morphological analysis of peripheral myelinated and demyelinated nerve fibers. *Neuroimage*, 37:1218–1226, 2007.

[85] T.J. Dennerll, P. Lamoureux, R.E. Buxbaum, and S.R. Heidemann. The cytomechanics of axonal elongation and retraction. *J Cell Biol*, 109:3073–3083, 1989.

[86] R. Bernal, P.A. Pullarkat, and F. Melo. Mechanical properties of axons. *Phys Rev Lett*, 99:018301, 2007.

[87] A.C. Bain, D.I. Schreiber, and D.F. Meaney. Modeling of microstructural kinematics during simple elongation of central nervous system tissue. *J Biomech Eng*, 125:798–804, 2003.

[88] K.B. Arbogast and S.S. Margulies. A fiber-reinforced composite model of the viscoelastic behavior of the brainstem in shear. *J Biomech*, 32:865–870, 1999.

[89] F. Tagliaferri, C. Compagnone, M. Korsic, F. Servadei, and J. Kraus. A systematic review of brain injury epidemiology in Europe. *Acta Neurochir*, 148:255–268, 2006.

[90] J.A. Acosta, J.C. Yang, R.J. Winchell, R.K. Simons, D.A Fortlage, P. Hollingsworth-Fridlund, and D.B Hoyt. Lethal injuries and time to death in a level I trauma center. *J Am Coll Surg*, 186:528–533, 1998.

[91] A.I. King. Fundamentals of impact biomechanics: part I - biomechanics of the head, neck, and thorax. *Ann Rev Biomed Eng*, 2:55–81, 2000.

[92] J. Versace. A review of the severity index. In *Stapp Car Crash Conference Proceedings*, volume 15. The Stapp Association, 1971.

[93] H. Henn. Crash tests and the head injury criterion. *Teaching mathematics and its applications*, 17:162–170, 1998.

[94] A.K. Ommaya, L. Thibault, and F.A. Bandak. Mechanisms of impact head injury. *Int J Impact Engng*, 15(4):535–560, 1994.

[95] M.H.A. Claessens, A.A.H.J. Sauren, and J.S.H.M. Wismans. Modelling of the human head under impact conditions. In *Stapp Car Crash Conference Proceedings*, volume 41. The Stapp Association, 1997.

[96] F.P. DiMasi, R.H. Eppinger, and F.A. Bandak. Computational analysis of head impact response under car crash loadings. In *Stapp Car Crash Conference Proceedings*, volume 39. The Stapp Association, 1995.

[97] E.G. Takhounts, R.H. Eppinger, J.Q. Campbell, R.E. Tannous, E.D Power, and L.S. Shook. On the development of the SIMon finite element head model. *Stapp Car Crash J*, 47, 2003.

[98] S. Kleiven. Evaluation of head injury criteria using a finite element model validated against experiments on localized brain motion, intracerebral acceleration, and intracranial pressure. *Int J Crashworthiness*, 11:65–79, 2006.

[99] J. Ho and S. Kleiven. Dynamic response of the brain with vasculature: a three-dimensional computational study. *J Biomech*, 40:3006–3012, 2007.

[100] W. Welker, J. Johnson, and A. Noe. Comparitive mammalian brain collections. Technical report, University of Wisconsin, Michigan State and National Museum of Health and Medicine, www.brainmuseum.org, 2007.

[101] D.C. Engel, J.E. Slemmer, A.S. Vlug, A.I.R. Maas, and J.T. Weber. Combined effects of mechanical and ischemic injury to cortical cells: secondary ischemia increases damage and decreases effects of neuroprotective agents. *Neuropharmacology*, 49:985–995, 2005.

[102] R.T. Miller, S.S. Margulies, M. Leoni, M. Nonaka, X. Chen, D.H. Smith, and D.F. Meaney. Finite element modeling approaches for predicting injury in an experimental model of severe diffuse axonal injury. In *Stapp Car Crash Conference Proceedings*, volume 42. The Stapp Association, 1998.

[103] T. Nishimoto and S. Murakami. Direct impact simulations of diffuse axonal injury by axial head model. *JSAE Review*, 21:117–123, 2000.

[104] W. Goldsmith and K.L. Monson. The state of head injury biomechanics: past, present, and future part 2: physical experimentation. *Crit Rev Biomed Eng*, 33:105–207, 2005.

[105] J.K. Mai, J. Assheuer, and G. Paxinos. *Atlas of the human brain*. Academic Press, London, GB, 1st edition, 1997.

[106] A.I. Leonov. Nonequilibrium thermodynamics and rheology of viscoelastic polymer media. *Rheol Acta*, 15:85–98, 1976.

[107] G.W.M. Peters and F.P.T. Baaijens. Modelling of non-isothermal viscoelastic flows. *J Non-Newtonian Fluid Mech*, 68:205–224, 1997.

[108] J.K. Wood. Dynamic response of human cranial bone. *J Biomech*, 4:1–12, 1971.

[109] V.G. Kouznetsova, W.A.M. Brekelmans, and F.P.T. Baaijens. An approach to micro-macro modeling of heterogenous materials. *Comp Mech*, 27:37–48, 2001.

[110] A. Garo, M. Hrapko, J.A.W. van Dommelen, and G.W.M. Peters. Towards a reliable characterisation of the mechanical behaviour of brain tissue: The effects of post-mortem time and sample preparation. *Biorheology*, 44:51–58, 2007.

[111] N.M. Lind, A. Moustgaard, J. Jelsing, G. Vajta, P. Cumming, and A.K. Hansen. The use of pigs in neuroscience: modeling brain disorders. *Neurosci Biohav R*, 31:728–751, 2007.

[112] H. Mao, L. Zhang, K.H. Yang, and A.I King. Application of a finite element model of the brain to study traumatic brain injury mechanisms in the rat. *Stapp Car Crash J*, 50, 2006.

[113] P. Aimedieu and R. Grebe. Tensile strength of cranial pia mater: preliminary results. *J Neurosurg*, 100:111–114, 2004.

[114] X. Jin, J.B. Lee, L.Y. Leung, L. Zhang, K.H. Yang, and A.I. King. Biomechanical response to the bovine pia-arachnoid complex to tensile loading at varying strain-rates. *Stapp Car Crash J*, 50, 2006.

[115] C. Lauret, M. Hrapko, J.A.W. van Dommelen, G.W.M. Peters, and J.S.H.M. Wismans. Optical characterization of acceleration-induced strain fields in inhomogeneous brain slices. *Med Eng Phys*, 31:392–399, 2009.

[116] J. Ho and S. Kleiven. Can sulci protect the brain from traumatic injury? *J Biomech*, 42:2074–2080, 2009.

[117] S. J. Strich. Diffuse degeneration of the cerebral white matter in severe dementia following head injury. *J Neurol Neurosurg Psychiat*, 19:163–185, 1956.

[118] S.M. Gentleman, G.W. Roberts, T A. Gennarelli, W.L. Maxwell, J.H. Adams, S. Kerr, and D.I. Graham. Axonal injury: a universal

consequence of fatal closed head injury. *Acta Neuropathol*, 89:537–543, 1995.

[119] D.H. Smith, D.F. Meaney, and W.H. Shull. Diffuse axonal injury in head trauma. *J Head Trauma Rehabil*, 18:307–316, 2003.

[120] J. D. Fenstermacher, C. Li, and V.A. Levin. Extracellular space of the cerebral cortex of normothermic and hypothermic cats. *Exp Neurol*, 27:101–114, 1970.

[121] V. Braitenberg and A. Schüz. *Cortex: Statistics and geometry of neuronal connectivity*. Springer, Berlin, Germany, 2nd edition, 1998.

[122] R. Ventura and K. Harris. Three-dimensional relationships between hippocampal synapses and astrocytes. *J Neurosci*, 19:6897–6906, 1999.

[123] D.B. Chklovskii, T. Schikorski, and C.F. Stevens. Wiring optimization in cortical circuits. *Neuron*, 34:341–347, 2002.

[124] J. Sahuquillo, M.A. Poca, and S. Amorós. Current aspects of pathophysiology and cell dysfunction after severe head injury. *Curr Pharm Des*, 7:1475–1503, 2001.

[125] M. Gaetz. The neurophysiology of brain injury. *Clin Neurophysiol*, 115:4–18, 2004.

[126] M. Khoshgoftar, S. Najarian, F. Farmanzad, B. Vahidi, and F.T. Ghomshe. A biomechanical composite model to determine effective elastic moduli of the CNS gray matter. *American J of Applied Sciences*, 4:918–924, 2007.

[127] N. Abolfathi, A. Naik, M. S. Chafi, G. Karami, and M. Ziejewski. A micromechanical procedure for modelling the anisotropic mechanical properties of brain white matter. *Comput Method Biomec*, 12:249–262, 2009.

[128] G. Karami, N. Grundman, N. Abolfathi, A. Naik, and M. Ziejewski. A micromechanical hyperelastic modeling of brain white matter under large deformation. *J Mech Behav Biomed*, 2:243–254, 2009.

[129] L. Snook, L. Paulson, D. Roy, L. Philips, and C. Beaulieu. Diffusion tensor imaging of neurodevelopment in children and young adults. *Neuroimage*, 26:1164–1173, 2005.

[130] M.T. Prange, D.F. Meaney, and S.S. Margulies. Defining brain mechanical properties: Effects of region, direction, and species. *Stapp Car Crash J*, 44, 2000.

[131] Simulia, Providence, R.I. *Abaqus 6.8 manual*.

[132] T.C. Gasser, R.W. Ogden, and G.A. Holzapfel. Hyperelastic modelling of arterial layers with distributed collagen fibre orientations. *J R Soc Interface*, 3:15–35, 2006.

[133] J.H. McElhany, V.L. Roberts, and J.F. Hilyard. *Handbook of human tolerance*. Japan Automobile Research Institute Inc., Tokyo, Japan, 2nd edition, 1976.

[134] D.E. Goldman and T.F. Hueter. Tabular data of the velocity and absorption of high-frequency sound in mammalian tissue. *J Acoustical Soc Am*, 28:35–37, 1956.

[135] A. Etoh, S. Mitaku, J. Yamamoto, and K. Okano. Ultrasonic absorption anomaly of brain tissue. *Jpn J Appl Phys*, 33:2874–2879, 1994.

[136] S. Lin, S. Shieh, and M.J. Grimm. Ultrasonic measurements of brain tissue properties. In *Symp Proc Center for Disease Control*, pages 27–31. Wayne State University, 1997.

[137] J.A. Galbraith, L.E. Thibault, and D.R. Matteson. Mechanical and electrical responses of the squid giant axon to simple elongation. *J Biomech Eng*, 115:13–22, 1993.

[138] M.C. LaPlaca, D.K. Cullen, J.J. McLoughlin, and R.S. Cargill II. High rate shear strain of three-dimensional neural cell cultures: a new in vitro traumatic brain injury model. *J Biomech*, 38:1093–1105, 2005.

[139] W. Rutland-Brown, J.A. Langlois, K.E. Thomas, and Y.L. Xi. Incidence of traumatic brain injury in the united states, 2003. *J Head Trauma Rehabil*, 21:544–548, 2006.

[140] T.A. Gennarelli, G.M. Spielman, T.W. Langfitt, P.L. Gildenberg, T. Harrington, J. A. Jane, L. F. Marshall, J. D. Miller, and L. H. Pitts. Influence of the type of intracranial lesion on outcome from severe head injury. *J Neurosurg*, 56:26–32, 1982.

[141] J. T. Povlishock. Pathobiology of traumatically induced axonal injury in animals and man. *Ann Emerg Med*, 22:980–986, 1993.

[142] H.L. Cater, D. Gitterman, S.M. Davis, C.D. Benham, B. Morrison III, and L.E. Sundstrom. Stretch-induced injury in organotypic hippocampal slice cultures reproduces in vivo post-traumatic neurodegeneration: role of glutamate receptors and voltage-dependent calcium channels. *J Neurochem*, 101:434–447, 2007.

[143] M.C. LaPlaca and G.R. Prado. Neural mechanobiology and neural vulnerability to traumatic loading. *J Biomech*, 43:71–78, 2010.

[144] Z. Yu and B. Morrison III. Experimental mild traumatic brain injury induces functional alteration of the developing hippocampus. *J Neurophysiol*, 103:499–510, 2010.

[145] Simulia, Providence, RI. *Abaqus 6.10 manual*, 2010.

[146] C. Liu, Y. Huang, and M.G. Stout. On the asymmetric yield surface of plastically orthotropic materials: a phenomenological study. *Acta mater*, 45:2397–2406, 1997.

[147] R. Hill. A theory of the yielding and plastic flow of anisotropic metals. *Proc Roy Soc London Ser A*, 193:281–297, 1948.

[148] D.C. Drucker and W. Prager. Soil mechanics and plastic analysis or limit design. *Q Appl Math*, 10:157–165, 1952.

[149] R. Hill. Theoretical plasticity of textured aggregates. *Math Proc Camb Phil Soc*, 85:179–191, 1979.

[150] W.L. Maxwell, C. Watt, D.I. Graham, and T.A. Gennarelli. Ultrastructural evidence of axonal shearing as a result of lateral acceleration of the head in non-human primates. *Acta Neuropathol*, 86:136–144, 1993.

[151] S. Nicolle, M. Lounis, R. Willinger, and J.F. Palierne. Shear linear behavior of brain tissue over a large frequency range. *Biorheology*, 42:209–223, 2005.

[152] D.C. Viano, I.R. Casson, E.J. Pellman, L. Zhang, A.I. King, and K.H. Yang. Concussion in professional football: brain responses by finite element analysis: part 9. *Neurosurgery*, 57:891–916, 2005.

[153] N.A. Shaw. The neurophysiology of concussion. *Prog Neurobiol*, 67:281–344, 2002.

[154] P.J. McCracken, A. Manduca, J. Felmlee, and R.L. Ehman. Mechanical transient-based magnetic resonance elastography. *Magn Reson Med*, 53:628–639, 2005.

[155] B.S. Elkin and B. Morrison III. Region-specific tolerance criteria for the living brain. *Stapp Car Crash J*, 51:127–138, 2007.

[156] W.N. Hardy, C.D. Foster, M.J. Mason, K.H. Yang, A.I. King, and S. Tashman. Investigation of head injury mechanisms using neutral density technology and high-speed biplanar x-ray. *Stapp Car Crash J*, 45:337–368, 2001.

[157] A.E. Walker, E.R. Laws, and G.B. Udvarhelyi. *The genesis of neuroscience*. American Association of Neurological Surgeons, Park Ridge, IL, 1998.

[158] D.W.A. Brands, G.W.M. Peters, and P.H.M. Bovendeerd. Design and numerical implementation of a 3-d non-linear viscoelastic constitutive model for brain tissue during impact. *J Biomech*, 37:127–134, 2004.

Samenvatting

De hersenen vormen een belangrijk onderdeel van ons lichaam. Zelfs bij voor de hand liggende taken, zoals het lezen van deze tekst, spelen ze een voorname rol. De hersenen houden rekening met de positie van je handen en het boek ten opzichte van het lichaam. Daarnaast wordt de informatie die via de ogen de hersenen binnenkomt, verwerkt en naar andere delen van de hersenen doorgestuurd. Daar worden de woorden die je leest gekoppeld aan taal en associaties waarbij een groot deel van je hersenen wordt aangesproken. En als je deze tekst uit hebt, herinner je er wellicht nog iets van; in de korte tijd dat het lezen van deze tekst kost, zijn je hersenen veranderd.

Het mag duidelijk zijn dat hersenletsel grote gevolgen kan hebben op het functioneren van een persoon. Hersenletsel wordt in veel gevallen veroorzaakt door een zware belasting op het hoofd, zoals een klap of een plotselinge snelle beweging. Dit wordt traumatisch hersenletsel genoemd. Om de oorzaak van traumatisch hersenletsel beter in beeld te brengen, wordt in dit onderzoek gekeken naar het verband tussen de zware belasting op het hoofd en schade aan de hersenen. Met de nieuwe inzichten uit dit onderzoek kunnen betere middelen worden ontwikkeld die moeten leiden tot een juiste diagnostiek voor betere behandeling. Ook kan hersenletsel preventief (deels) tegen worden gegaan door de ontwikkeling van bijvoorbeeld veiligere auto's of het gebruik van verbeterde helmen.

Voornamelijk het type hersenletsel dat ontstaat door een plotselinge snelle beweging van het hoofd (en niet door een klap) verloopt volgens een complex proces. Een van de moeilijkheden hierbij is het feit dat hersenletsel op verschillende schaalniveaus plaatsvindt: bij een plotselinge snelle beweging

van het hoofd (macroniveau), zoals bij een ongeval, vindt de uiteindelijke schade op een lager niveau plaats, namelijk de zenuwcellen (microniveau). Echter, de relatie tussen deze niveaus was tot nog toe niet grondig onderzocht. Bij de meeste studies naar traumatisch hersenletsel wordt alleen gekeken naar de plotselinge bewegingen van het hoofd en niet naar spanningen en rekken in de hersenen zelf. Een meer verfijnde methode is om de spanningen en rekken van hersenweefsel als gevolg van een versnelling van het hoofd met computermodellen te berekenen. Letsel kan dan worden voorspeld door de berekende rekken of spanningen te koppelen aan letselcriteria. Deze criteria geven aan bij welke rekken of spanningen er schade aan het hersenweefsel ontstaat.

De meeste van bovengenoemde computermodellen bevatten geen gedetailleerde beschrijving van de anatomie van de hersenen. Omdat het niet duidelijk is of deze vereenvoudiging in de bestaande modellen van invloed is op de voorspellingen van hersenletsel, is het eerste deel van dit onderzoek gericht op de juistheid hiervan. Hiervoor zijn vier computermodellen ontwikkeld met elk een andere vorm. Drie van deze modellen geven de gedetailleerde anatomie van een klein deel van de oppervlakte van hersenen met gevouwen structuren weer. Het vierde model heeft een massieve structuur (dus zonder gevouwen structuur) die samen met de drie andere modellen wordt gebruikt om de invloed van vouwen aan de oppervlakte van de hersenen te analyseren. Met behulp van deze computermodellen is aangetoond dat er lokaal hoge spanningen optreden aan de oppervlakte van de hersenen die in andere modellen niet aanwezig zijn vanwege de vereenvoudigde weergave. Bovendien komen de locaties van deze berekende spanningsconcentraties overeen met de locaties waar volgens pathologische onderzoeken ook daadwerkelijk hersenletsel wordt gevonden. Dit betekent dat de reeds bestaande letselcriteria van hersenletsel, zoals hierboven genoemd, wellicht niet direct toegepast kunnen worden op hoofdmodellen die geen anatomische details van de hersenen bevatten.

Het tweede deel van dit onderzoek gaat over de mechanische relatie tussen het weefsel- en celniveau van hersenletsel. Doordat de hersencellen allerlei microstructuren vormen, wordt aangenomen dat de krachten op het weefsel niet een-op-een worden doorgegeven aan de cellen, maar dat deze krachten onregelmatig verdeeld worden. Dit heeft mogelijk invloed op de kans op schade aan de hersenen. Om deze invloed te bestuderen zijn er voor dit

onderzoek computermodellen ontwikkeld. Deze zijn gebaseerd op pathologisch onderzoek, waarbij beschadigingen van hersencellen ter grootte van enkele duizendsten van millimeters zijn ontdekt. De computermodellen geven verhoogde rekken aan op dezelfde plekken als deze beschadigingen in de werkelijkheid voorkomen. Dat geeft aan dat de mechanische invloed op microniveau mogelijk van belang is voor de kans op hersenletsel. Bovendien laten berekeningen met de computermodellen zien dat de gevoeligheid van hersenweefsel voor letsel afhankelijk is van de richting van de belasting op weefselniveau. Vervolgens is er in dit onderzoek een formule ontwikkeld waarmee deze richtingsafhankelijke gevoeligheid van hersenweefsel voor letsel kan worden bepaald. Tenslotte zijn er in dit onderzoek berekeningen uitgevoerd waarbij een computermodel van het hoofd is gebruikt waarbij de effecten op microniveau zijn geïmplementeerd. Dit is op twee verschillende manieren gebeurd: enerzijds door het micromodel rechtstreeks te koppelen aan het hoofdmodel en anderzijds door de eerdergenoemde formule te gebruiken in het hoofdmodel. Met het hoofdmodel is een ongeval gesimuleerd, waarbij de resultaten voor beide methoden vrijwel gelijk zijn. Dit betekent dat de praktisch toepasbaar ontwikkelde formule even goed werkt als de gecompliceerde methode, waarbij het micromodel direct aan het hoofdmodel is gekoppeld.

De verschillende modellen die in dit onderzoek zijn ontwikkeld, tonen aan dat de meeste van de huidige computermodellen van het hoofd details missen die een juiste voorspelling van hersenletsel in de weg kan staan. Het is dus van belang om de effecten veroorzaakt door deze details mee te nemen in toekomstige studies. Hierbij kan de ontwikkelde methode uit dit onderzoek van pas komen, of eventueel worden verbeterd door verder onderzoek.

Acknowledgements

Doing a PhD is of course not an easy job. At least, that is my opinion. Finishing a PhD really feels as quite an achievement. However, I certainly did not do it all by myself. Therefore, I would like to thank a few people.

I am very grateful to my promotor Marc Geers and copromoter Hans van Dommelen. They have supported me during the entire process of my PhD research and I appreciate it a lot how helpful they have been. Always when I thought I was almost able to, figuratively speaking, jump over the bar, Marc nudged it up a little higher by saying the right words, so in the end I learned to jump twice as high as I thought I was able to. Furthermore, the many discussions I had with Hans have been quite important for the development of this thesis.

Also, I would like to thank the committee members prof.dr. Gerhard Holzapfel, prof.dr.ir. Gerrit Peters, prof.dr.ir. Jos Vander Sloten, dr. Svein Kleiven and dr. Barclay Morrison for their interest in my research; the dean of our department prof.dr. Philip de Goey for being the chairman during my defense.

I would like to thank Svein Kleiven also for giving me the opportunity to conduct research at Neuronics, KTH in Stockholm for a period of three months as well as for the collaboration afterwards. The people at Neuronics (and in Stockholm in general) were friendly, which was quite motivating. Special thanks go to Xiaogai Li and Tobias Nyberg for our discussions regarding brain injury, but especially for all the other discussions we had.

Thanks to my students Lisa Tang, Wai Chua and Giuseppe Melpignano for their contribution to my research and thus indirectly for their interest in

my research. Concerning the work performed by Lisa, I would furthermore like to thank Gerrit Peters, Gustav Strijkers and Anna Vilanova for their help and discussions.

Thanks to Alice, Patrick, Leo and Arno, for their help regarding the practical issues.

I have to say that because of the friendly people in MaTe, my time at the university was very pleasant. I want to mention a few more people by name. First, my office mates during these years: Matej, Pieter, Lambert, Arash, Cem, Juan Carlos, Erica, Bart, Peter, Gwen, Lars, Britta, René, Gulia, Roman, Agnese, Hamid, Murthy, Bhairav and Selim. Some other people that made the office walls seem to disappear in a nice way and with whom I had nice discussions: Mohammad, Tuncay, Ana, Piz, Véronique, (other) Lambert, Susanne, Leong Hien, Jan, Frederico, İzzet, İsa, Pooya, Casper and Willem-Jan. Most of the people I have not even mentioned yet, but feel free to write your name here, if you think you have been forgotten...

En natuurlijk bedankt Johanneke en veel liefs aan Jasmijn en Melle.

Rudy, October 2011

Curriculum Vitae

Rudy Cloots was born on January 14, 1982 in Sittard, the Netherlands. In 2000, he finished his secondary education at the Trevianum in Sittard. From September 2000 until February 2007 he studied Biomedical Engineering at the Eindhoven University of Technology. During this study, he became mainly interested in the biomechanical field and he received his Master's degree in 2007 on the subject of the mechanical influence of the heterogeneities of the cerebral cortex on traumatic brain injury. After that, he started a Ph.D. research on the subject of the multi-scale mechanics of traumatic bran injury in the Materials Technology group of the Eindhoven University of Technology. Part of his research was conducted at the School of Technology and Health of the Royal Institute of Technology in Stockholm, Sweden. Since 2011 he is employed at Code Product Solutions in Geleen, the Netherlands.

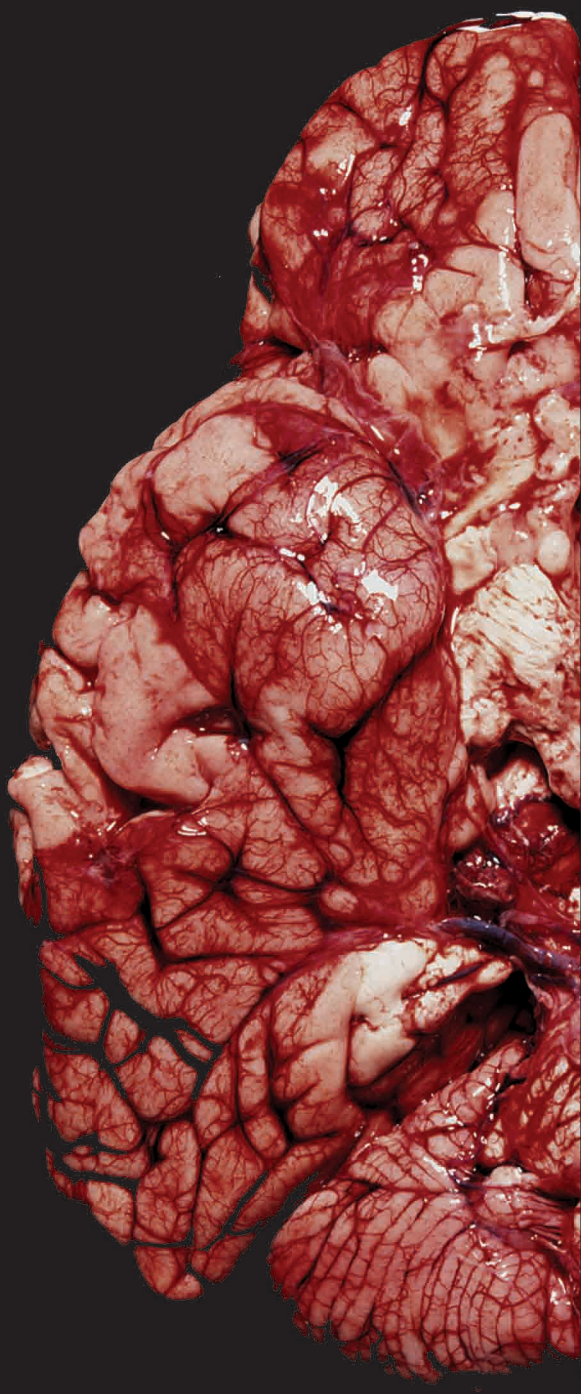

Photograph © Fragile 2009 - courtesy Raphaël Dallaporta